Topological phases and phase transitions in magnets and ice

Keesman, R.

Citation

Keesman, R. (2017, June 7). *Topological phases and phase transitions in magnets and ice*. *Casimir PhD Series*. Retrieved from https://hdl.handle.net/1887/49403

Version: Not Applicable (or Unknown)

License: [Licence agreement concerning inclusion of doctoral thesis in the Institutional Repository of the University of Leiden]

Downloaded from: https://hdl.handle.net/1887/49403

Note: To cite this publication please use the final published version (if applicable).

Cover Page

Universiteit Leiden

Leiden University Repository

The handle http://hdl.handle.net/1887/49403 holds various files of this Leiden University dissertation.

Author: Keesman, R.
Title: Topological phases and phase transitions in magnets and ice
Issue Date: 2017-06-07

Topological Phases and Phase Transitions in Magnets and Ice

Proefschrift

ter verkrijging van
de graad van Doctor aan de Universiteit Leiden,
op gezag van Rector Magnificus prof.mr. C.J.J.M. Stolker,
volgens besluit van het College voor Promoties
te verdedigen op woensdag 7 juni 2017
klokke 11.15 uur

door

Rick Keesman

geboren te Hengelo
in 1988

Promotores:	Prof. dr. G. T. Barkema	(Universiteit Utrecht en Universiteit Leiden)
	Prof. dr. R. A. Duijne	(Universiteit Utrecht en Technische Universiteit Eindhoven)
Promotiecommissie:	dr. L. Fritz	(Universiteit Utrecht)
	Prof. dr. M. V. Mostovoy	(Universiteit Groningen)
	Prof. dr. J. Aarts	
	Prof. dr. E. R. Eliel	

FSC
www.fsc.org
MIX
Paper from
responsible sources

Casimir PhD series, Leiden 2017-14
ISBN 978-90-8593-297-0
Printed by: Gildeprint - Enschede
An electronic version of this thesis can be found at
https://openaccess.leidenuniv.nl

This work is part of the D-ITP consortium,
a program of the Netherlands Organisation for Scientific Research (NWO)
that is funded by the Dutch Ministry of Education, Culture and Science (OCW).

The cover shows an artistic rendering of a spin structure in the skyrmion phase of a ferromagnet (top) transforming into a typical arrow configuration in the six-vertex model (bottom).

Contents

Publications vii

Introduction ix

1 Néel skyrmions in confined geometries 1
  1 Introduction . . . 1
  2 Model and simulations . . . 6
  3 Magnetic phases and phase diagram . . . 9
  4 Degeneracies and fluctuations . . . 13
  5 Conclusions, discussion, and outlook . . . 21

2 Skyrmions in square-lattice antiferromagnets 23
  1 Introduction . . . 23
  2 Model . . . 25
  3 Phases . . . 26
  4 Phase diagram from simulations . . . 28
  5 Analytical phase diagram . . . 28
  6 Interaction energies . . . 31
  7 Skyrmions . . . 32
  8 Discussion and conclusion . . . 35

3 Finite-size scaling at infinite-order phase transitions 37
  1 Introduction . . . 37
  2 The F model and observables . . . 39
  3 Simulations . . . 41
  4 Analysis . . . 45
    4.I Peak position $\beta_{\max}$ . . . 45
    4.II Peak height $h_{\max}$ . . . 47
    4.III Peak width w . . . 49
  5 Comparison of observables . . . 49
    5.I Logarithmic derivative of P_0 . . . 50
    5.II Ordinary derivative of P_0 . . . 50

5.III Polarizability 51
6 Conclusion 51

4 The F model with domain walls 53
1 Introduction 53
2 Theory 56
2.I The F model and domain walls 56
2.II The domain-wall partition function 60
2.III The staggered polarization 61
3 Simulations 64
4 Results 66
4.I Energy and specific heat 66
4.II The logarithmic derivative of P_0 70
4.III Arctic curves 74
4.IV Oscillations in vertex densities 74
5 Summary and outlook 82
A Relating opposite configurations 84

Outlook 87

References 89

Samenvatting 105

Acknowledgements 113

Curriculum vitae 115

List of Figures

0.1 Finite-size scaling for the Ising model xix
0.2 Diagram of racetrack memory xxii
0.3 Square and I_h ice xxiii
0.4 The six allowed vertices xxiv

1.1 Ferromagnetic phase diagram 5
1.2 Various ferromagnetic configurations 8
1.3 Various wire-like configurations for increasing field strength . . 11
1.4 Ground state degeneracy (with quantum corrections) 15
1.5 Energy at the degeneracy points as function of temperature . . 18
1.6 Probability ratios at degeneracy points as function of temperature 19
1.7 Discrete jumps in the winding number and magnetization . . . 20

2.1 Various anti-ferromagnetic ground state configurations 27
2.2 Anti-ferromagnetic phase diagram 30
2.3 Energy contributions of various parameters for anti-ferromagnets 32
2.4 Skyrmion probability in a finite anti-ferromagnet 34

3.1 The six allowed vertices 40
3.2 The three observables as function of temperature 44
3.3 Data collapse for the three observables 46
3.4 Critical temperature as function of system size 47
3.5 Maximal height as function of system size 48
3.6 Peak width as function of system size 49

4.1 The six allowed vertices 57
4.2 Full six-vertex model phase diagram 58
4.3 Average energy and specific heat as functions of temperature . 68
4.4 Energy as a function of system size 69
4.5 $d \ln P_0/d\beta$ as a function of temperature 72
4.6 Characteristics of $d \ln P_0/d\beta$ as a function of system size 73
4.7 Local c-vertex densities at various temperatures 75
4.8 Vertex densities along the diagonal at the critical point 77

4.9 Average c-vertex density difference for various system sizes . . 78
4.10 Local c-vertex density differences at various temperatures . . . 80
4.11 Truncated local c-vertex density differences 81

5.1 Magneetveldenlijnen voor verscheidene configuraties. 108
5.2 Een spin configuratie met één skymrion. 109
5.3 De zes toegestane vertices 111

Publications

This Thesis is based on the following works:

[1] R. Keesman, A. O. Leonov, P. van Dieten, S. Buhrandt, G. T. Barkema, L. Fritz, and R. A. Duine, *Degeneracies and fluctuations of Néel skyrmions in confined geometries*, Phys. Rev. B **92**, 134405 (2015), arXiv:1506.00271 [cond-mat.mes-hall].

[2] R. Keesman, M. Raaijmakers, A. E. Baerends, G. T. Barkema, and R. A. Duine, *Skyrmions in square-lattice antiferromagnets*, Phys. Rev. B **94**, 054402 (2016), arXiv:1603.03688 [cond-mat.mes-hall].

[3] R. Keesman, J. Lamers, R. A. Duine, and G. T. Barkema, *Finite-size scaling at infinite-order phase transitions*, J. Stat. Mech., 093201 (2016), arXiv:1605.08876 [cond-mat.stat-mech].

[4] R. Keesman and J. Lamers, *Numerical study of the F model with domain-wall boundaries*, Phys. Rev. E **95**, 052117 (2017), arXiv:1702.05474 [cond-mat.stat-mech].

Other publications:

[5] R. Keesman, G. T. Barkema, and D. Panja, *Dynamical eigenmodes of star and tadpole polymers*, J. Stat. Mech., P02021 (2013), arXiv:1210.0774 [cond-mat.mat.soft].

[6] R. Keesman, G. T. Barkema, and D. Panja, *Dynamical eigenmodes of a polymerized membrane*, J. Stat. Mech., P04009 (2013), arXiv:1212.1024 [cond-mat.mat.soft].

Introduction

This work is a culmination of my efforts as a PhD student at Instituut-Lorentz for Theoretical Physics at Leiden University. Each of the following four chapters in this Thesis is based on published work (or accepted for publication) and can be read separately. These works, however, also share some similarities. In particular, both the method of investigation, mainly Monte Carlo simulations, and the overarching topic of topological phases and phase transitions are a recurring focus in each of these chapters.

The next sections were written for readers who want to familiarize themselves more with these topics. The first three sections treat general concepts in my computational physics research, whereas the last two sections are good starting points for understanding the models used in each of the following four chapters in this Thesis.

Topological phases and phase transitions

First, we clarify what is meant by topological phases and phase transitions. Phases and topological phases are defined, after which phase transitions are discussed.

The phase of matter is a term that can only be used macroscopically. Whatever fluctuations are going on at the microscopic level averages out at the macroscopic level which allows for the description of the system in terms of macroscopic bulk properties in the thermodynamic (infinite size) limit. These properties are homogeneous over (a part of) the system at a macroscopic level. Examples are the volume of a gas, the temperature of a liquid, or the magnetization of some solid. When such properties can be defined, the system is in a certain phase.

Very recently (Oct 2016) David Thouless, Duncan Haldane, and Michael Kosterlitz were awarded the Nobel Prize in Physics *"for theoretical discoveries of topological phase transitions and topological phases of matter"* [7]. Among other results they discovered that, in some cases a topological integer, like the winding number in a plane or the number of holes in an object, can be assigned to a physical system. When this number is non-zero the system is in a topologically non-trivial phase or, in short, a topological phase.

Macroscopic properties of the system can vary due to changes of the system while being in a certain phase. An example is the temperature dependence of the specific heat of liquid water at constant pressure. When the system is on the verge of going from one phase into another, however, usually at least one macroscopic property changes drastically. To distinguish between a change within a phase or between phases one has to define the order parameter. The order parameter is defined as being zero in one phase and non-zero in the other[8] making the order parameter non-analytic by definition. In ferromagnetic systems the total magnetization can serve as the order parameter as it is zero above the Curie temperature and nonzero below it. The phase transition is then unambiguously defined as the point at which the order parameter changes from zero to non-zero.

There is a plethora of phase transitions that can all be grouped into certain types of phase transitions, as well as specific classes. The different types of phase transitions are nowadays defined by the behaviour of the temperature of the system with respect to the energy that is poured into it.

An example of a first-order phase transition is the boiling of a cup of water. As more energy is injected into the system via heating the temperature increases until it reaches the boiling point. All the heat that is injected into the system from that point onwards is being used to evaporate the liquid water into its gaseous form instead of increasing the temperature. Only when all of the water is gaseous will the injection of energy into the system result in an increase of temperature. The energy as a function of temperature makes a discrete jump. The first derivative of the energy with respect to temperature diverges, which makes this phase transition of the first order.

Many magnetic phase transitions are of the second order. If you take an ordinary ferromagnet at high temperatures in a small magnetic field, it will stay disordered due to all the thermal fluctuations. When the temperature is gradually lowered the system will, at some point, almost instantly collapse into an ordered ferromagnetic state aligned along the external magnetic field. These states behave quite differently, and the energy as a function of temperature has a kink at the phase transition, at which the derivative is not well-defined, resulting in a divergence in the second derivative of the energy with respect to temperature. In a similar way all higher-order phase transitions can be defined.

The systems in the first two chapters have a second-order phase transition.

Close enough to the critical point, susceptibilities of observables show power-law decay, and it is the set of exponents from the power-laws that define in which class of phase transitions the system belongs to. It is interesting to note that different microscopically defined systems can have the same critical behaviour and are thus in the same universality class [9].

These systematic definitions of the order of a phase transition can be continued to third and higher order but the most curious type is that of infinite order. In this case the energy as a function of temperature is non-analytic, as it is described by two different analytic functions on both sides of the phase transition, but yet is completely smooth. In other words, the energy nor its derivatives have a discontinuity. Chapter 3 and 4 of this Thesis treat a system that has a Berezinskiĭ–Kosterlitz–Thouless transition [10, 11, 12], which is an infinite-order type phase transition.

The types of phase transitions can also be distinguished by whether or not the state of matter changes from and to a topologically non-trivial phase. Phase transitions into and from a topologically non-trivial phase are called topological phase transitions whereas transitions between two topologically trivial phases are usually just called phase transitions. Certain phase transitions, however, are between two topologically trivial phases but involve the binding or proliferation of topological excitations called (anti)-vortices. These types of phase transitions are usually also called topological phase transitions and the most notable example is the phase transition in the two-dimensional classical XY-model, a lattice model in which vectors on a ring are energetically favoured to align with neighbouring vectors, which is also of the KBT type. The XY-model is also closely related to the model used in Chapter 3 and 4.

It is interesting to note that for the XY-model there is a different type of long-range order known as quasi-long range order. Usually one can define a completely disordered phase, that is positionally and orientationally isotropic, and a crystalline phase that possesses long-range order in which local information allows you to extrapolate the exact local configuration at any distance. In two dimensions, however, it has been shown, first by Berenzinskiĭ, that there can also be quasi long-range order leading to a topological phase transition. In this case there is still bond-orientational order but no longer any positional order. In other words, from local information, one can still determine the positions of (quasi)particles relative to each other but nothing can be said about their absolute positions.

Simulation methods

Simulations are a valuable tool, not only to compare to analytical results, but more so to address research questions currently out of reach of analytical methods. Throughout this work all simulations have been done using some form of the Monte Carlo method [13]. It is very successful in approximating the exact probability distribution of a system with lots of degrees of freedom and a relatively smooth energy landscape.

Another very important concept is parallel tempering [14]. This is another algorithm-independent method to explore phase space at various temperatures in parallel to reduce the difficulties that arise when the landscape is not so smooth. It exchanges configurations at different temperatures as to overcome energy barriers one might encounter.

Monte Carlo simulation

Monte Carlo simulations are probabilistic simulations that use random inputs to mainly study systems that are otherwise too difficult to solve analytically. A big class of problems considers a phase space $\mathscr{P}$ where each point $C \in \mathscr{P}$ has a certain weight $w_C > 0$. If the weights are known then the probability p_C of state C occurring is given by its relative value $p_C = w_C/Z$, where $Z := \sum_C w_C$ is the partition function. Monte Carlo simulations can be used to explore the phase space and procure draws from the probability distribution such that the expectation values of observables can be estimated.

In thermal equilibrium, for a classical system at temperature T connected to a thermal bath, the probability of microstate C to occur is given by the Boltzmann weight

$$p_C = \frac{1}{Z} \exp(-\beta E_C) \ , \tag{0.1}$$

where $\beta := 1/(k_B T)$ is the inverse temperature, k_B Boltzmann's constant, and E_C the total energy of C [15]. In turn this means that the occurrence probability ratio $r_{CD} := p_C/p_D = \exp(-\beta E_{CD})$ only depends on the temperature and energy difference $E_{CD} := E_C - E_D$ between the states.

A Markov process [16] describes a transition with probability $P_{C\to D}$ between states C and D that only depends on these states. The history of the states the system was in before this process is irrelevant. A typical Monte Carlo simulation uses such a process in which C and D are relatively closeby, e.i., E_{CD} is not too large, such that r_{CD} does not deviate too much from unity. This type of sampling is called importance sampling [17] in which most computation time is spent in sets of microstates that have the largest contributions to the partition function.

To ensure correct sampling of the equilibrium distribution there are two very important conditions that must apply to the simulation. The first is global balance which states that the rate from and to state C must be equal

$$\sum_D p_C P_{C\to D} = \sum_D p_D P_{C\to D} \ . \tag{0.2}$$

If they are equal then the system is in equilibrium. A much stricter condition is that of detailed balance

$$p_C P_{C\to D} = p_D P_{D\to C} \ , \tag{0.3}$$

which is easier to prove for algorithms and implement. Systems with detailed balance also satisfy global balance by definition. There are, however, some interesting algorithms that break detailed balance [18]. The second condition is that of ergodicity which states that every configuration $C \in \mathcal{P}$ must have some probability of occurring if the Markov process is continued long enough such that all of $\mathcal{P}$ is probed eventually.

From Eqs. (0.1,0.3) we conclude that if the transition probabilities satisfy

$$\frac{P_{D\to C}}{P_{C\to D}} = \exp(-\beta E_{CD}) \ , \tag{0.4}$$

then the draws from $\mathcal{P}$ are weighted properly. To maximize the acceptance of proposed transitions the best choice for the transition probability is given by

$$P_{C\to D} = \begin{cases} \exp(\beta E_{CD}) & , \ E_{CD} < 0 \\ 1 & , \ \text{else} \ . \end{cases} \tag{0.5}$$

Algorithms that satisfy this are known as Metropolis algorithms [19].

These types of Monte Carlo simulations allow you to probe the parts of a large phase space that are most relevant at a certain temperature. Additionally, if the starting point of the simulations are out of equilibrium the systems will thermalize automatically after enough time has passed. If the whole of phase space is of interest, however, simulations need to be run over a temperature range and large improvements of data quality can be obtained by making use of parallel tempering.

Parallel tempering

If various Monte Carlo simulations are run at different temperatures each simulation probes different regions of phase space. Even at a single temperature there might be disjoined regions of alike configurations and if a Monte Carlo simulation only updates to very similar configurations it is likely to stay in one of these regions for a long time. The Ising model is an example of such a system with a degenerate ground state where spins are all either up or down. If you only flip single spins at a time then at low temperatures it will be very unlikely for the system to reverse its netto magnetization and ergodicity is broken in practice. At higher temperatures the energy barriers between different regions become of less importance and transitions between these regions become easier. Parallel tempering, also known as replica exchange Markov chain Monte Carlo (MCMC) sampling, uses this to its advantage by allowing simulations at different temperatures to swap configurations. At high temperatures the configurations are more likely to change rapidly and by swapping back to low temperatures they might end up in another disjoined region than where they came from. Parallel tempering is also mostly independent of the update algorithm used. As long as an update algorithm can be used at any temperature parallel tempering can be wrapped around it. It is most successful for systems with lots of energy barriers and disjoined regions, like glassy systems.

To explain the general form of parallel tempering we need to distinguish between a microstate and the tuning parameters that characterize a system. In general we can define the microstate to contain all the information of the degrees of freedom. For a spin glass the randomness and temperature would be part tuning parameters and the spins part of the microstate. Microstate C has an energy E_C or $E_{C'}$ depending on which parameters it is evaluated for. The inverse temperatures of the systems are β and $\beta_{C'}$ respectively. Similarly as for a normal Monte Carlo move described above it follows from detailed balance that

$$\frac{P_{CD'\to C'D}}{P_{C'D\to CD'}} = \frac{p_{C'}p_D}{p_C p_{D'}} = \exp(-\beta' E_{C'D'} + \beta E_{CD}) \ . \tag{0.6}$$

If only the temperatures differ between the systems and the energies are parameter independent, i.e., $E_{CD} = E_{C'D'}$, this simplifies to

$$\frac{P_{CD'\to C'D}}{P_{C'D\to CD'}} = \exp(\Delta\beta E_{CD}) \ , \tag{0.7}$$

with $\Delta\beta = \beta - \beta'$. Using Metropolis the swapping probability is then maximized when

$$P_{CD' \to C'D} = \begin{cases} \exp(-\beta' E_{C'D'} + \beta E_{CD}) = \exp(\Delta\beta E_{CD}) & , \ \Delta\beta E_{CD} < 0 \\ 1 & , \ \text{else} \ . \end{cases} \tag{0.8}$$

In other words; we always accept a swap if it moves the energetically favourable microstate to the colder system, and otherwise swap with some probability smaller than one.

Given a set of temperatures the above provides all the means to implement parallel tempering. Choosing an optimal set of temperatures is, however, another problem that has to be faced before the simulations can be run. The set of temperatures is typically bound by the temperature range of interest, most likely a large range around a phase transition starting from the unordered state to well below the critical temperature. Typically around the phase transition the specific heat, and thus the relative energy fluctuations, are rather large and so temperature differences must decrease to have the same overlap of energy distributions for the different temperatures. The higher the specific heat the more simulations must be run in a temperature range to ensure the same swapping probability as in a region with low specific heat. There are iterative methods of finding the most optimal temperature set that minimize the time a configuration takes going from the lowest temperature to the highest temperature and back [20]. Note that there is still a choice to be made for the size of the temperature set. If it is too small and the swap probability goes down due to energy differences being too large but with too many temperatures the configuration will take much longer to perform its random walk from highest to lowest temperature.

Data analysis methods

Although it is very important to gather data using efficient algorithms it is equally important to correctly analyse this data afterwards. In almost all cases are we interested in the behaviour of a system in the thermodynamic limit, meaning we would like to know what happens for large systems. Unfortunately, simulations only allow for the investigation of systems at finite size, but it is the behaviour of the system as a function of increasing system size that allows us to make predictions for the asymptotic case of an infinite system.

This is where finite-size scaling [13, 21] or other extrapolation methods come in.

Another very elegant analysis tool is the multi-histogram method [22, 23], where data obtained at specific temperatures is combined and extrapolated to give you a best-estimate analytical function of any observable based on the data. This method works particularly well for large systems for which data accumulation is more tedious than the post analysis.

Finite-size scaling

Finite-size scaling (FSS) is an analysis method to extrapolate simulation results for finite systems to the thermodynamic limit. The outcome of FSS used on a set of data obtained for finite-sized systems is entirely dependent on the data set and the assumed mathematical form of convergence to the asymptotic value.

In most cases an approximation for the behaviour of a certain observable for large system sizes is made, taking only the leading-order finite-size effects into account. This leads to the separation of the behaviour of an observable into a size-dependent part and some dimensionless function. If the large-system behaviour is assumed correctly and the fitting parameters valued correctly then all data for large enough systems will collapse onto the same unknown dimensionless function for which you do not need any prior knowledge. An example of FSS for the two-dimensional Ising model is shown in Fig. 0.1 in which the magnetic susceptibility per site χ for systems of various linear sizes L are collapsed onto each other.

For second-order phase transitions this works particularly well as power-law divergences can be scaled rather easily. The pre-factors and exponents that are obtained from FSS can then be used to extrapolate the behaviour of large enough systems. There are, however, also some challenges regarding FSS that have to do with the reliability of the data. The scaling assumptions work well for large systems close enough to the critical point, and so there are systematic deviations between the data and the dimensionless function for finite-sized systems and away from the critical point. Practically that means that data for small systems or away from the critical point must be assigned a larger systematic error on top of the random error, although it is hard to quantify. For large systems, or close to the critical point, random errors are typically large due to larger fluctuations that occur in these situations.

Many other techniques have been developed to extrapolate to the asymptotic limit. The scaling encountered in the Kibble-Zurek mechanism [24, 25] is interesting to mention as it describes a type of finite-time scaling that can be applied to non-equilibrium dynamics of a system that undergoes a continuous phase transition. The Binder cumulant [26] is a quantity in terms of higher-order cumulants of the order parameter that, in the asymptotic limit, has a different constant value at each side of the critical point. Since it only weakly depends on system size this quantity changes between these asymptotic values at the same (critical) point for various system sizes giving an accurate estimate for the critical value.

Multi-histogram method

The multi-histogram method [22, 23] is based on the idea that every measurement you do gives you information about the free energy. In principle, if you know the free energy you can extract any equilibrium property for the system. At a specific temperature your system will reach equilibrium with a certain average energy, but fluctuations allow for energies for the system above or below this average leading to a probability distribution of the energy. For slightly different temperatures this function of the energy will also differ only slightly, and so the whole probability function estimated at a certain temperature can be reweighed to approximate the probability function at a nearby temperature. In case of the multi-histogram method, all data collected at a set of temperatures is combined to give information over a larger temperature regime.

It is important to note that, unless an exact value for the partition function at some (typically zero or infinite) temperature is known, the partition function can only be estimated up to some overall factor. For most observables, however, this overall factor is divided out and of no importance. Therefore we omit this overall factors in the definitions below.

Let us assume that the simulations have been done at a set of inverse temperatures β_i with n_i measurements taken at β_i. The iterative expression for the best estimate, given the set of measurements, of the partition function Z_i at β_i can then be expressed as

$$Z_i = \sum_{k,s} \frac{1}{\sum_j n_j Z_j^{-1} \exp^{(\beta_i - \beta_j) E_{ks}}} \ , \tag{0.9}$$

where the sum is taken over all measurements and E is the total energy of the system. Starting from a set Z_i this expression allows for the convergence of Z_i to the true best estimate for $Z(\beta)$ given the set of measurements. The analytical expression for $Z(\beta)$ in terms of Z_i is given by

$$Z(\beta) = \sum_{k,s} \frac{1}{\sum_j n_j Z_j^{-1} \exp^{(\beta-\beta_j)E_{ks}}} \ . \tag{0.10}$$

Any observable O can be expressed in terms of the data similarly as for the partition function. Let O_{ks} be the s-th instantaneous value of some observable O measured in this system at β_k. The best estimate for $O(\beta)$ is then given by

$$O(\beta) = \frac{1}{Z(\beta)} \sum_{k,s} \frac{O_{ks}}{\sum_j n_j Z_j^{-1} \exp^{(\beta-\beta_j)E_{ks}}} \ . \tag{0.11}$$

To ensure accurate results measurements must be made over a complete range of the energy spectrum. This is satisfied when the energy probability functions at neighbouring temperatures all overlap. The energy probability functions for intermediate temperatures can then be interpolated accurately as enough measurements around this peak have been performed. The reason this method works so well with parallel tempering is that the requirement of overlapping energy probability functions needs to be met for both methods. One problem arising in the investigation of second order phase transitions is the divergence of the specific heat for increasing system size. In other words; around the critical temperature, a small change in temperature leads to a large difference in average energy, and so the temperature difference must be smaller to ensure overlap of the probability distributions of the energies. Luckily, for the F-model which we study in Chapter 3 and 4 of this Thesis, the specific heat per site is bounded, even for infinite sized systems, and so this problem does not arise.

In short, the multi-histogram method allows for the interpolation of any observable as a function of temperature that lies within the original set of temperatures at which the simulations were performed, as long as all instantaneous energies and values of that observable are saved. The only requirements are that the probability functions of the energies at neighbouring temperatures are reasonably close to ensure some overlap.

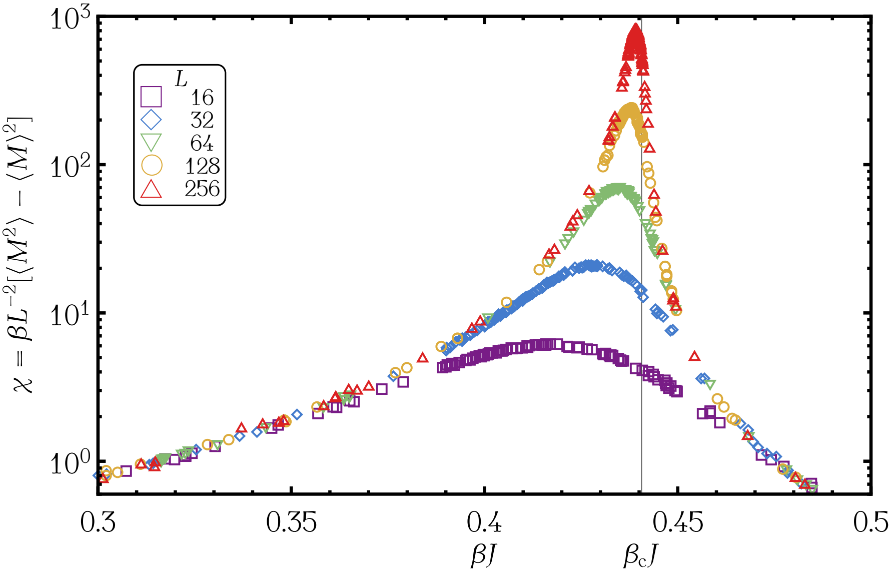

(a)

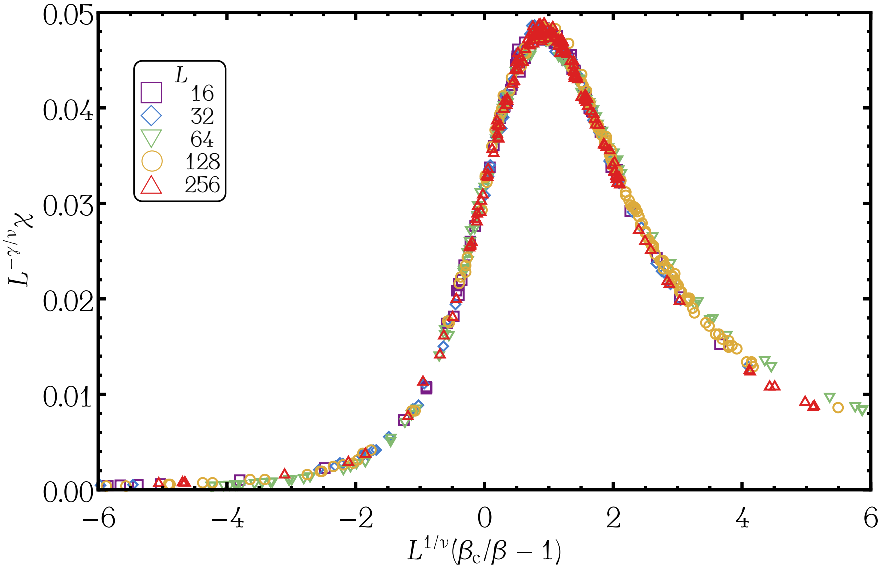

(b)

Figure 0.1. The magnetic susceptibility per site χ for the two-dimensional Ising Model is shown as a function of scaled inverse temperature βJ in (a) for various linear system sizes L and collapsed in (b). The data only collapses for correct values of exponents γ and ν as well as the inverse critical temperature β_c.

Magnets

Magnets are a part of daily life. Without these, many electrical devices simply would not work. Most of these magnets are not so much like the kitchen magnet, a ferromagnet that rarely changes its state, but more so like systems that can be changed on demand by means of some form of input. This allows devices, such as magnetic hard disks, to function and a lot of effort is put into researching how to improve upon our current systems by making them faster, cheaper to produce, smaller, and more energy efficient.

The basis for my research on skyrmions, a topologically protected magnetic configuration, in (anti)ferromagnets stems from the idea that spin textures can be manipulated and transported over two-dimensional wires. Various groups have shown that these skyrmions can be created, annihilated, moved, and detected. All ingredients are present to create a working memory track from materials in which these skyrmions are stable. An impression of how this works with domain walls rather than skyrmions is shown in Fig. 0.2. For skyrmion based racetrack memory devices the skyrmions would replace the magnetic domains as effective data carriers.

To understand magnets in which these more exotic spin textures can occur we must investigate the spin of elementary particles. In short, spin is an intrinsic form of angular momentum that induces a magnetic moment. The interplay of all these magnetic moments defines the type of magnet. Most notably, and relevant for the first two chapters, are the ferromagnet and antiferromagnet. In both cases the spins couple to an external magnetic field and want to align with it. For the ferromagnet, the spins want to align with each other. The spins in an antiferromagnet, in contrast with the ferromagnet, favour a configuration in which they are anti-parallel. Above the Curie temperature [27] the thermal fluctuations destroy the resulting order. The classical Heisenberg model describes these systems where the spins are assumed to be classical vectors on a sphere

$$H = -\sum_{\boldsymbol{r}\boldsymbol{r}'} J_{\boldsymbol{r}\boldsymbol{r}'} \boldsymbol{S}_{\boldsymbol{r}} \cdot \boldsymbol{S}_{\boldsymbol{r}'} - \boldsymbol{B} \cdot \sum_{\boldsymbol{r}} \boldsymbol{S}_{\boldsymbol{r}}, \tag{0.12}$$

with the sum taken over all spins. For $J_{\boldsymbol{r}\boldsymbol{r}'} > 0$ we obtain a model for the ferromagnet and for $J_{\boldsymbol{r}\boldsymbol{r}'} < 0$ it models an anti-ferromagnet The interaction strength is determined by many factors, such as the distance between the two spins and the atoms involved. In practice most higher order contributions are neglected and due to crystalline structures most of the interactions are equal in strength resulting in only a few non-zero values for the couplings $J_{\boldsymbol{r}\boldsymbol{r}'}$.

Until now we have not made any assumption regarding the geometric structure of the material. It turns out that the interplay between different materials and the complex inner structure of the materials can give rise to more exotic features. Igor Dzyaloshinskii and Toru Moriya found that two ions can couple indirectly via spin-orbit coupling with a third ion giving rise to an antisymmetric exchange interaction of the form $\boldsymbol{D}_{ij} \cdot (\boldsymbol{S}_i \times \boldsymbol{S}_j)$ [28, 29]. The form of $\boldsymbol{D}_{ij}$ depends on the symmetries of the system.

In the first two chapters we focus on two-dimensional square-lattice magnetic systems in which this asymmetry can be induced by enclosing the material of interest by two different types of materials on either side. This can also lead to anisotropy in which spins have a preferred alignment in a certain direction. For easy-axis anisotropy the spins want to align along the normal of the plane whereas for easy-plane the energy is reduced by aligning in-plane. This is described by a term of the form $K(\boldsymbol{S}_{\boldsymbol{r}} \cdot \hat{\boldsymbol{z}})^2$. We also neglect any Heisenberg interaction other than nearest-neighbour interaction and assume they are all of equal strength. The most general Hamiltonian that takes all the above into account can thus be written as

$$\begin{aligned} H = -J \sum_{\boldsymbol{r}\boldsymbol{r}'} \boldsymbol{S}_{\boldsymbol{r}} \cdot \boldsymbol{S}_{\boldsymbol{r}'} + K \sum_{\boldsymbol{r}} (\boldsymbol{S}_{\boldsymbol{r}} \cdot \hat{\boldsymbol{z}})^2 \\ + \sum_{\boldsymbol{r}\boldsymbol{r}'} \boldsymbol{D}_{\boldsymbol{r}\boldsymbol{r}'} \cdot (\boldsymbol{S}_{\boldsymbol{r}} \times \boldsymbol{S}_{\boldsymbol{r}'}) - \boldsymbol{B} \cdot \sum_{\boldsymbol{r}} \boldsymbol{S}_{\boldsymbol{r}}, \end{aligned} \tag{0.13}$$

where the sum is taken over nearest neighbours in the square lattice. In the first two chapters these types of systems, with exhibit more exotic spin textures than are usually present, are investigated.

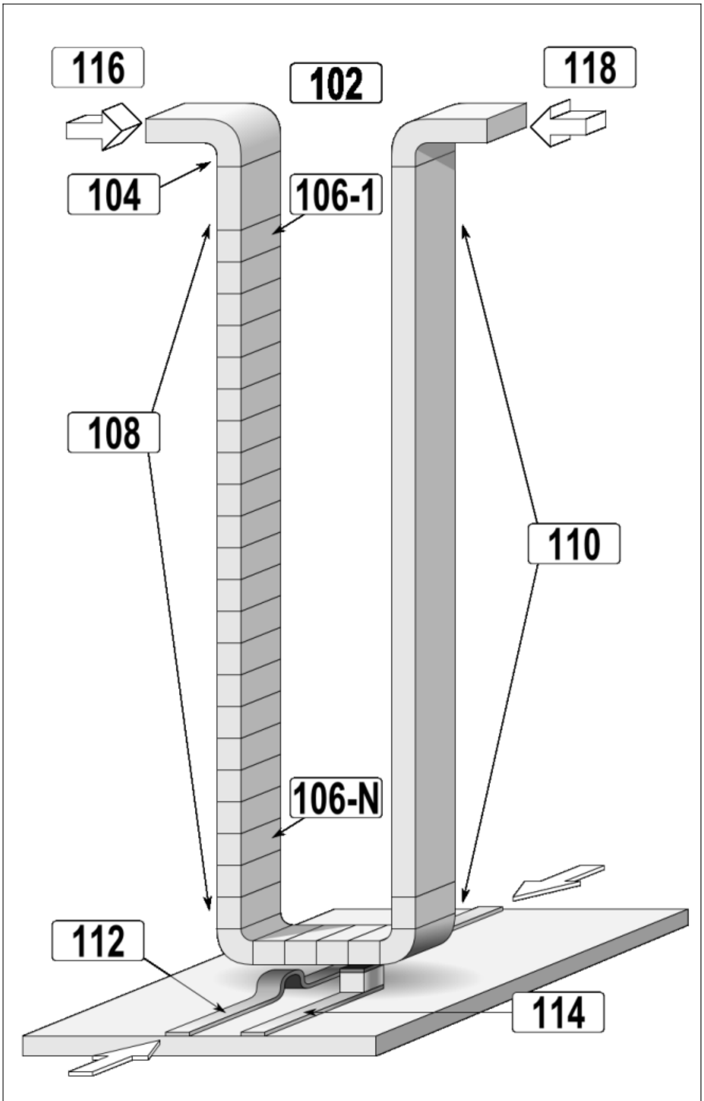

United States Patent
Patent No.: US 7,768,809 B2 Date of Patent: Aug. 3, 2010
WALL NUCLEATION PROPAGATION FOR RACETRACK MEMORY

Figure 0.2. This figure displays the diagram for wall nucleation propagation for racetrack memory from the original patent. Bits are made up by magnetic domains separated by domain walls. The wire containing the data can be build vertically rather in contrast to conventional two-dimensional data storage techniques. At 112 and 114 in the diagram the data can be written and read respectively. From 116 and 118 the data can be driven via a current pulse.

Ice

Ice as mentioned throughout this Thesis is not a typical form of ice but rather two-dimensional square-lattice ice. Similarly to the magnets the focus lies on fixed lattice systems with internal degrees of freedom at each vertex. There is, however, a link with actual three-dimensional frozen water (the conventional ice).

Although there are many different types of ice structures the most common type in nature, an hexagonal form of ice known as I_h, is shown in Fig. 0.3(a). In I_h each oxygen atom has four neighbouring oxygen atoms that form a regular tetrahedron around it. Hydrogen bonds, where hydrogen atoms bind tightly to one and loosely to another heavier atom, stabilize this structure. The energy is minimized when each oxygen atom has two hydrogen atoms nearby and two further away giving rise to a 'two in two out' rule also called the ice rule[30]. It was argued by Pauling[31] that there are still internal degrees of freedom for this system, even in the thermodynamic limit at zero temperature, giving rise to a residual entropy.

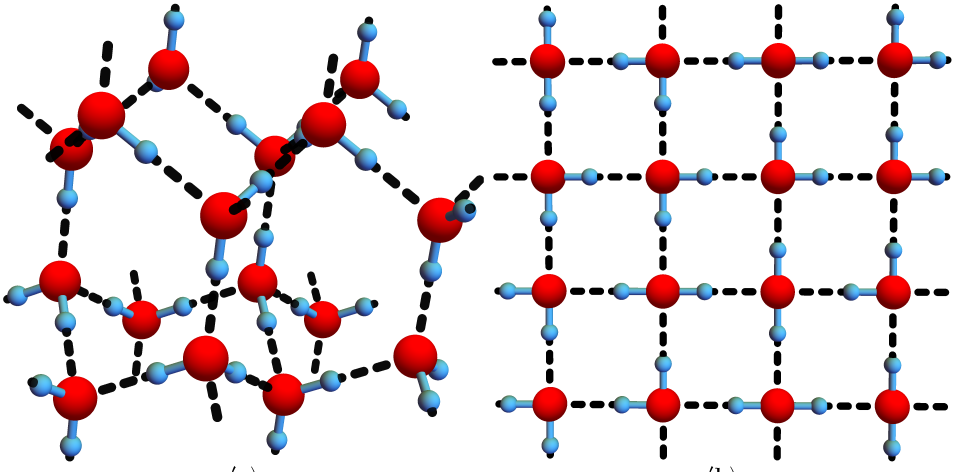
(a) (b)

Figure 0.3. Parts of typical configurations of ice are shown in its hexagonal I_h structure (a) and two-dimensional square structure (b). Red (blue) spheres denote the position of oxygen (hydrogen) atoms. Solid lines are shown for the intermolecular bonds and dotted lines for hydrogen bonds.

Two-dimensional square ice, see Fig. 0.3(b), has recently been realized[32] by trapping water in between two sheets of graphene. Similar to I_h it also has a residual entropy as a result of internal degrees of freedom[33]. These systems, at moderately low temperatures at which the crystalline structure is fixed, can be effectively modelled by a square-lattice model at which each vertex has two arrows going in and two arrows going out. These types of models are called ice-type models or six-vertex models since the ice rule restricts the system allowing exactly six different vertex configurations on a single site shown in Fig. 0.4.

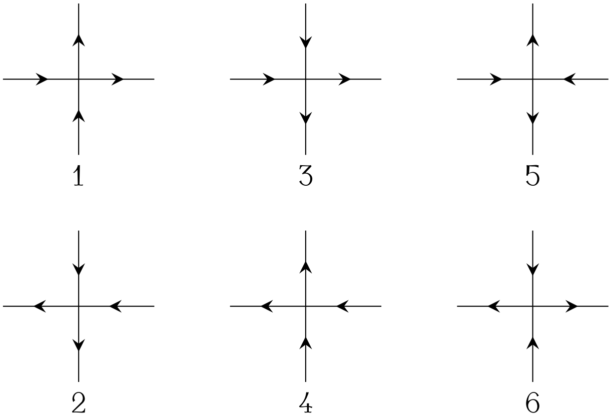

Figure 0.4. The ice rule dictates every vertex must have two arrows going in and two arrows going out which allows for six different vertices.

Energetic six-vertex models assign different weights to some of the vertices leading to phase transitions between a disordered phase and various ordered phases. In Chapter 3 and 4 the F-model, a specific type of energetic six-vertex model, is considered because of its interesting properties. Besides the infinite-order phase transition the system is also interesting due to the effects that boundaries can have on the system even in the limit of large systems. Normally the effects of the boundaries disappear for increasing system size but it can be shown for certain boundaries that the behaviour of systems changes dramatically. Another similarity between magnets and ice studied in this Thesis is that the F-model, here explained as a model for water ice, can also be viewed as a model for spin ice. Spin ices are magnetic materials in which the degrees of freedom are determined by the spins of certain fixed atoms. The F-model can be mapped onto the XY-model which in turn is a two-dimensional variant of the Heisenberg model, used to study magnets.

1 Degeneracies and fluctuations of Néel skyrmions in confined geometries

The recent discovery of tunable Dzyaloshinskii-Moriya interactions in layered magnetic materials with perpendicular magnetic anisotropy makes them promising candidates for stabilization and manipulation of skyrmions at elevated temperatures. In this chapter, we use Monte Carlo simulations to investigate the robustness of skyrmions in these materials against thermal fluctuations and finite-size effects. We find that in confined geometries and at finite temperatures skyrmions are present in a large part of the phase diagram. Moreover, we find that the confined geometry favors the skyrmion over the spiral phase when compared to infinitely large systems. Upon tuning the magnetic field through the skyrmion phase, the system undergoes a cascade of transitions in the magnetic structure through states of different number of skyrmions, elongated and half skyrmions, and spiral states. We consider how quantum and thermal fluctuations lift the degeneracies that occur at these transitions, and find that states with more skyrmions are typically favoured by fluctuations over states with less skyrmions. Finally, we comment on electrical detection of the various phases through the topological and anomalous Hall effects.[1]

1 Introduction

A skyrmion is a certain type of topological field configuration which was first introduced in particle physics. It corresponds to a classical stationary solution of the equations of motion with which one can associate a topological invariant and describes the emergence of a discrete particle from a continuous field [34].

---

[1] The contents of this chapter are largely based on the work of R. Keesman, A. O. Leonov, P. van Dieten, S. Buhrandt, G. T. Barkema, L. Fritz, and R. A. Duine [1]. Simulations were based on code provided by S. Buhrandt and L. Fritz, the quantum corrections in Sec. 1.4 are based on the work of P. van Dieten, and A. O. Leonov provided insightful comments and ideas that resulted in investigation of transitions in small wire-like systems as in Fig. 1.3. It is also a pleasure to thank G. Bauer, R. Lavrijsen, and H. Swagten for useful comments.

More recently, skyrmions have been considered in quantum Hall devices [35], Bose-Einstein condensates [36, 37], and liquid crystals [38, 39, 40]. Magnetic skyrmions were predicted [41] and recently observed in bulk materials like MnSi and Cu_2OSeO_3 at low temperatures [42, 43, 44]. In these materials, bulk inversion symmetry is broken which allows for nonzero Dzyaloshinskii-Moriya (DM) interactions [28, 29] that lead to helical, conical, and skyrmionic spin textures depending on the applied magnetic field [41]. It was proposed that skyrmions are promising candidates for encoding binary data that allow for high-density and low power consumption magnetic memories due to low critical currents for skyrmion motion and their inherent topological stability [45, 46, 47]. In addition to fundamental interest concerning the interplay between topology, geometry and fluctuations, it is therefore relevant to understand the behavior of skyrmions at high temperature and in confined thin-film geometries for realizing spintronic devices.

Motivated by recent experiments on domain wall motion in magnetic thin films with perpendicular magnetic anisotropy (PMA materials) that point to sizeable and tunable DM interactions [48, 49, 50, 51, 52, 53, 54] and anisotropy, we use Monte Carlo simulations to investigate the robustness of skyrmions in these systems in confined wire-like geometries against thermal fluctuations. Our main results are: i) The phase diagram in Fig. 1.1 that shows which spin textures are to be expected at a certain anisotropy strength and applied magnetic field at nonzero temperature. We find that the confining geometry extends (with respect to systems in the thermodynamic limit) the skyrmion phase at the expense of the spiral phase. ii) The cascade of transitions between different magnetic structures that the system undergoes upon lowering the magnetic field through the skyrmion phase, a typical example of which is shown in Fig. 1.3. iii) The temperature dependence of relative probabilities for occurrence of different skyrmions configurations that are degenerate at zero temperature, shown in Fig. 1.6. We find that at moderate temperature configurations with more skyrmions are typically entropically favored over configuration with less skyrmions. Moreover, we also consider quantum fluctuations and find that these also favor configurations with higher skyrmion number.

Skyrmions are predicted to occur in several varieties [41], two of which have by now been experimentally identified. One of these is the Néel (somtimes also called "hedgehog") skyrmion, i.e., a skyrmion in which the magnetization points radially outward from the skyrmion center. The other type of skyrmion (where the magnetization is perpendicular to radii pointing outward from the skyrmion center) is called a Bloch skyrmion. (See Fig. 1 of Ref. [46] for an illustration.) Which of the two types is favored depends on which type of DM interactions are present as dictated by the crystal and/or structural symmetry. In the long-wavelength limit, the DM interactions yield a contribution to the energy density that is a certain combination of so-called Lifshitz invariants, i.e., antisymmetric terms of the form

$$S_i \frac{\partial S_j}{\partial r} - S_j \frac{\partial S_i}{\partial r} \ , \tag{1.1}$$

with S_i the i-th cartesian component of the spin and $r = x, y$ or z, a spatial direction. In MnSi, one of the most-studied skyrmion materials, the DM interactions give a contribution proportional to

$$\boldsymbol{S} \cdot (\nabla \times \boldsymbol{S}), \tag{1.2}$$

which is straightforwardly shown to be a combination of terms of the form as in Eq. (1.1), and favors Bloch skyrmions. For the PMA materials that are the focus of this work, the DM interactions are interface-induced (see also Ref. [55]) and stabilize Néel skyrmions. They are proportional to the expression

$$(\boldsymbol{z} \cdot \boldsymbol{S})(\nabla \cdot \boldsymbol{S}) - (\boldsymbol{S} \cdot \nabla)(\boldsymbol{z} \cdot \boldsymbol{S}) \ , \tag{1.3}$$

and in this particular form are shown to explicitly depend on the symmetry-breaking direction $\boldsymbol{z}$ which denotes the normal to the interface. We note, however, that the above form of DM interactions also arises in crystals of symmetry class C_{nv} and therefore that Néel skyrmions are stabilized by bulk DM interactions in some materials. This was recently observed in the magnetic semiconductor GaV_4S_8 [56]. In this material there are no Lifshitz invariants in the z-direction and a conical phase is therefore not present. Our results therefore also apply to this case, and, particularly when grown in thin-film form on different substrates, the magnetic anisotropy of this material may be tuned between easy axis and easy plane which enables experimentally exploring the full phase diagram in Fig. 1.1.

Previous theoretical studies have focused on the skyrmion phase diagram of infinite systems at zero temperature [41, 57] and nonzero temperature in two and three dimensions [58, 59]. The first experimental results on bulk materials [42, 43, 44] have been extended to confined geometries, such as thin films, e.g. of MnSi [60] and FeGe [61]. Transitions between states with a different number of skyrmions and other (non-skyrmion) magnetic configurations as a function of field have been discussed experimentally and theoretically (at zero temperature) for thin films of MnSi (and thus for bulk DM interactions leading to Bloch skyrmions) in Refs. [62, 63]. Evidence for such a cascade of transitions in magnetoresistance measurements was very recently discussed in Ref. [64]. In these works, the Bloch skyrmion core lines (and field) lie in the plane of the thin film or along the wire direction due to strong easy-plane anisotropy induced by tensile strain from the substrate. As a result, only in-plane fields stabilize skyrmions whereas fields perpendicular to the thin film (and thus anisotropy plane) lead to conical phases. In the two-dimensional configuration that we consider, however, (see Fig. 1.3) the external field is perpendicular to the thin film and skyrmions may be observed for both easy-plane and easy-axis anistropy. For the form of the DM interactions considered here [Eq. (1.3)] the conical phase is absent and the easy-plane anisotropy leads to a large external-field range over which skyrmions are stable (see Fig. 1.1). Moreover, the confined geometry stabilizes skyrmions over spirals as the skyrmion phase becomes larger in the wire geometry with respect to the case of an infinite system.

Very recently, Du *et al.* reported on real-space observation of a cascade of transitions in the magnetic structure of a FeGe wire [65]. Although this system stabilizes Bloch skyrmions, this work gives experimental corroboration of many of our findings, such as the existence of elongated skyrmions, the creation of skyrmions from edge states, and the enhanced stability of skyrmions in the confining geometry. Moreover, these authors also observe that spirals orient themselves with their wave vector along the edge of the wires (see also Ref. [66]), which is in line with our results as well.

Finally, we note for completeness that single Bloch skyrmions in nanodisks were considered in Ref. [67] without taking into account anisotropy and that the effects of thermal fluctuations and confining geometry on single-skyrmion dynamics was considered in Refs. [59, 68, 69].

The remainder of this chapter is organized as follows. In Sec. 1.2 we discuss our model hamiltonian and the algorithm used in our simulations. Using these simulations we then construct the anisotropy-external field phase diagram for wire-like systems at moderate temperature and discuss the various magnetic phases and cascade of transitions between them in Sec. 1.3. Hereafter we focus on points in the phase diagram where degeneracies occur at zero temperature and investigate how fluctuations lift these degeneracies. We end with a conclusion and outlook, and briefly discuss electrical detection of the various magnetic configurations.

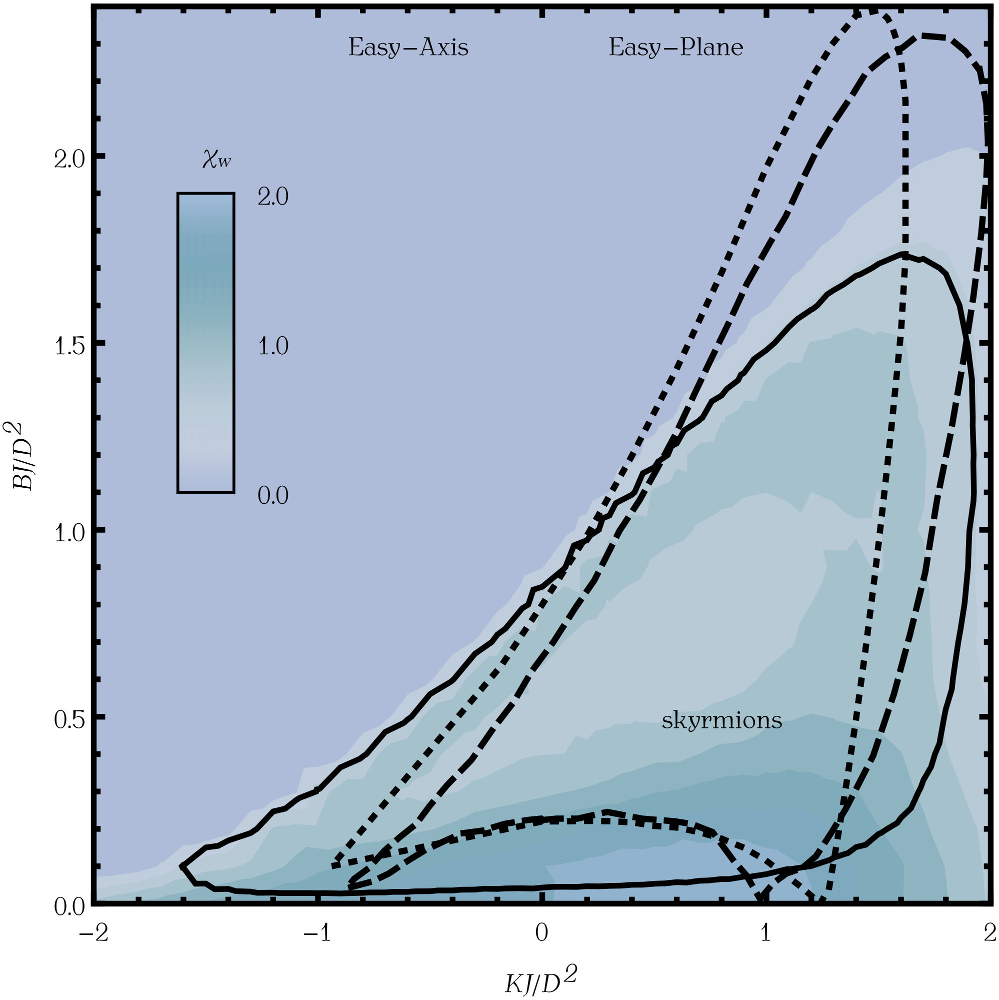

Figure 1.1. The anisotropy-external field phase diagram for a wire geometry with $L = 16$ and $p = 8$ at $k_BT/J = 0.5$ (solid line) and zero temperature (dashed line). The dotted line corresponds to the case of an infinite system at zero temperature [70]. These lines encircle the region where the winding number is larger than one half. The susceptiblity of the winding number at finite temperature χ_w is also indicated.

2 Model and simulations

We consider Heisenberg spins $\boldsymbol{S}_{\boldsymbol{r}}$ of unit length, where $\boldsymbol{r}$ denotes the location on a two-dimensional square lattice in the x-y-plane. The spins interact via a ferromagnetic Heisenberg coupling $J > 0$, Dzyaloshinskii-Moriya coupling D, and are subject to an anisotropy term K and an external magnetic field $\boldsymbol{B}$. The effective hamiltonian is given by

$$\begin{aligned} H = &-J\sum_{\boldsymbol{r}} \boldsymbol{S}_{\boldsymbol{r}} \cdot \left(\boldsymbol{S}_{\boldsymbol{r}+\hat{\mathbf{x}}} + \boldsymbol{S}_{\boldsymbol{r}+\hat{\mathbf{y}}}\right) \\ &+K\sum_{\boldsymbol{r}} (\boldsymbol{S}_{\boldsymbol{r}} \cdot \hat{\boldsymbol{z}})^2 - \boldsymbol{B} \cdot \sum_{\boldsymbol{r}} \boldsymbol{S}_{\boldsymbol{r}} \\ &-D\sum_{\boldsymbol{r}} \left(\boldsymbol{S}_{\boldsymbol{r}} \times \boldsymbol{S}_{\boldsymbol{r}+\hat{\mathbf{x}}} \cdot \hat{\boldsymbol{y}} - \boldsymbol{S}_{\boldsymbol{r}} \times \boldsymbol{S}_{\boldsymbol{r}+\hat{\mathbf{y}}} \cdot \hat{\boldsymbol{x}}\right). \end{aligned} \tag{1.4}$$

The above form of the DM interactions (i.e., the term in the hamiltonian proportional to D) corresponds to the discretized version of Eq. (1.3) and is therefore to lowest order in nearest-neighbor coupling appropriate for the PMA materials of interest to us here, i.e., for the situation that the DM interactions arise due to inversion asymmetry induced by the presence of an interface. In the hamiltonian we have neglected dipole-dipole interactions. This is appropriate in the limit of strong DM interactions that lead to small skyrmions and where the dipolar field will only renormalize parameters such as the anisotropy. We note that throughout this chapter we consider a wire geometry, i.e., a two-dimensional system with periodic boundary conditions in one direction and open boundary conditions in the other direction.

For simplicity we assume $\boldsymbol{B} = B\hat{\boldsymbol{z}}$ perpendicular to the x-y-plane and take $B > 0$ without loss of generality. The dimensionless parameters $k_B T/J \equiv 1/(\beta J)$, with $k_B T$ the thermal energy, BJ/D^2, and KJ/D^2 determine the state of the system. An important length scale is the pitch length p (in units of the lattice constant) that determines the periodicity of magnetic textures that arise due to competition between DM interaction D and exchange J. In case of a spiral state, for example, the pitch length will be the period of the spirals. In the absence of anisotropy, $K = 0$, the pitch length is given by [59] $D/J = \tan(2\pi/p)$ and we will use this definition throughout. This relation can be used to coarse-grain the system by keeping the ratio between the dimensions of the system and the pitch length constant while changing discretization.

We use classical Monte Carlo simulations to sample phase space at finite temperatures T. A typical simulation starts with a completely randomized square lattice of spins with $L \times L$ sites (with one open and one periodic boundary) at fixed parameters BJ/D^2 and KJ/D^2 at a scaled temperature $k_BT/J = 10.0$ far above the critical temperature of the system. After several lattice updates the temperature is lowered to a fraction of 0.95 of the last temperature until a temperature $k_BT/J = 0.01$ is reached. At each temperature data is collected and 100 simulations are independently run per set of parameters.

At every temperature the lattice is updated using the Metropolis algorithm followed by a cluster-flipping algorithm. The Metropolis algorithm consists of choosing a spin at random from the lattice and proposing a new direction for this spin. The proposed spin direction is chosen uniformly from the area that is the spherical cap around the original direction where the maximal angle between the original and the proposed spin direction is α, and α is dynamically adjusted so that the acceptance probability is approximately 50%. The cluster-flipping algorithm grows a cluster of spins and flips all the spins in the opposite direction similar to the Wolff algorithm for Ising spins. In both cases acceptance rates for changing a spin (or cluster of spins) are based on the energy difference between the spin states before and after the move such that the system is sampled according to the Boltzmann distribution [13].

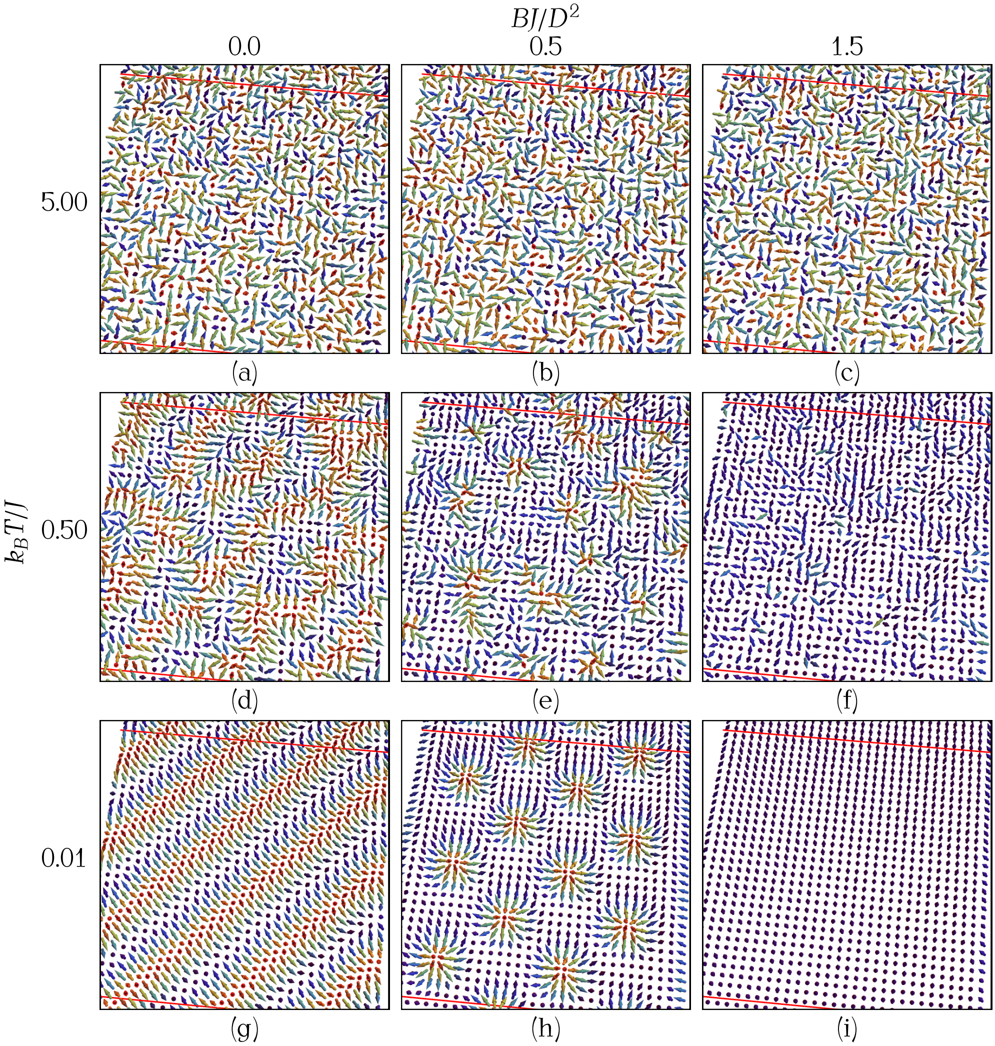

Figure 1.2. Simulations snapshots of spin systems of size $L \times L = 32 \times 32$ for different parameter values and temperatures with the parameter D/J chosen such that the pitch length $p = 8$. The periodic boundary is drawn as a red solid line and spin vectors are represented by colored arrows where the color scales linearly with the $\hat{\boldsymbol{z}}$-component of the vector to highlight spin textures. From top to bottom k_BT/J takes on values 5.00, 0.50, and 0.01 respectively and the system undergoes a transition from an unpolarized state to an ordered state in this temperature range. In all cases KJ/D^2 is zero and from left to right BJ/D^2 has values 0.0, 0.5, and 1.5, resulting in a spiral, skyrmion and polarized state, respectively, for low enough temperatures.

3 Magnetic phases and phase diagram

Throughout this chapter we use a nonstandard definition of phases and phase diagram. In the systems we consider there can, strictly speaking, not be any thermodynamic phase transition breaking a continuous symmetry for two reasons: (a) we always work at finite temperature in a two-dimensional system where the Mermin-Wagner theorem forbids the breaking of a continuous symmetry even in the thermodynamic limit; (b) we explicitly consider finite size systems where a real thermodynamic phase transition is also ruled out. Nonetheless, it is possible to identify phases that are distinct in their magnetic configurations, such as phases that may or may not have magnetic skyrmions.

In order to distinguish such phases, a useful quantity is the winding number w, which plays the role of a topological charge. It is quantized in a system with periodic boundary conditions and in terms of the unit vector $\boldsymbol{n} = \langle \boldsymbol{S} \rangle / |\langle \boldsymbol{S} \rangle|$ (we choose $\boldsymbol{n}$ instead of $\boldsymbol{S}$ to distinguish between the microscopic spin and the order parameter field) it reads

$$w = \frac{1}{4\pi} \int dx dy \boldsymbol{n} \cdot \left(\partial_x \boldsymbol{n} \times \partial_y \boldsymbol{n} \right) \,, \tag{1.5}$$

in the continuum limit. In the definition of $\boldsymbol{n}$ and throughout this chapter angular brackets denote the expectation value in the canonical ensemble. A single (anti-) skyrmion contributes (minus) one to the winding number. This effectively means that the number of skyrmions in an ordered state can be counted. From a set of independent simulations with identical parameters the susceptiblity of the winding number $\chi_w = \left(\langle w^2 \rangle - \langle w \rangle^2 \right) J / k_B T$ is calculated. In the latter expression the expectation values are determined by using Eq. (1.5), with $\boldsymbol{n}$ replaced by $\boldsymbol{S}$ and the integral replaced by a sum, for a given spin configuration in the simulations and then averaging over many such configurations. Whenever the system undergoes a transition between states with different number of skyrmions this susceptibility will be enhanced.

To determine the phase diagram we take the linear system size L equal to 16 with one periodic boundary condition (i.e., a wire geometry) at fixed parameter values BJ/D^2 and KJ/D^2. We note here that we simulate a square lattice for convenience throughout, and have not performed finite-size scaling as a function of wire length as we expect our findings to merely change quantitatively for larger system size in the periodic direction. We slowly cooled down the system below the critical temperature and measured the susceptibility of the winding number χ_w. For $k_B T / J = 0.5$ and zero temperature we find the phase diagram in Fig. 1.1, divided into an easy-axis ($K < 0$) and easy-plane ($K > 0$) part. Within the solid line in this figure, the average winding number is larger than one half, so that magnetic skyrmion configurations are expected. The dashed line corresponds to the zero temperature case for the same wire-like confined geometry. The dotted line corresponds to the infinite system at zero temperature [70]. Below the skyrmion phase boundary one finds a phase where spiral states rather than skyrmions are stabilized in the infinitely large system. At elevated temperatures ($k_B T/J = 0.5$) and in the confined geometry we also find spiral states for fields below the skyrmion phase, albeit that more complicated textures also appear (depending on system size, pitch length, and anistropy; below we discuss the magnetic configurations in this region in more detail). In the confined geometry the skyrmion phase becomes larger (with respect to the infinite system) at the expense of the spiral phase. We attribute this to the larger ability of skyrmions as compared to spirals to adapt to the repulsive forces away from the edges of the system [69]. Du *et al.* have observed this enhanced stability for Bloch skyrmions in FeGe nanowires [65].

For fields too large to stabilize skyrmions, the spins are uniformly polarized. In this part of the phase diagram and for fields larger than $2K$ (with $K > 0$) the spins are pointing along the field, i.e., along the z-direction. For smaller fields and $K > 0$ the easy-plane anisotropy tilts the spins away from the field direction.

The colors in the phase diagram indicate the susceptibility of the winding number. Depending on system size relative to pitch length, the magnetic configuration within the skyrmion phase may undergo transitions between phases with different number of skyrmions. At each such transition the winding number susceptibility is enhanced.

Finally, we note that the phase diagram at zero temperature was studied before for infinite system size with different methods [57]. Contrary to this latter work we do not find a tri-critical point where polarized, spiral and skyrmion phases meet in the easy-plane part of the phase diagram from our simulations. Representative spin configurations of the polarized state, the spiral state, and the skyrmion state at small temperature can be found in Fig. 1.2(g), (h), and (i), respectively. We also note that for Bloch skyrmions the role of anisotropy on the ground-state phase diagram was discussed in Ref. [60].

As we have already mentioned in the discussion of the phase diagram, the system goes through different magnetic configurations upon lowering

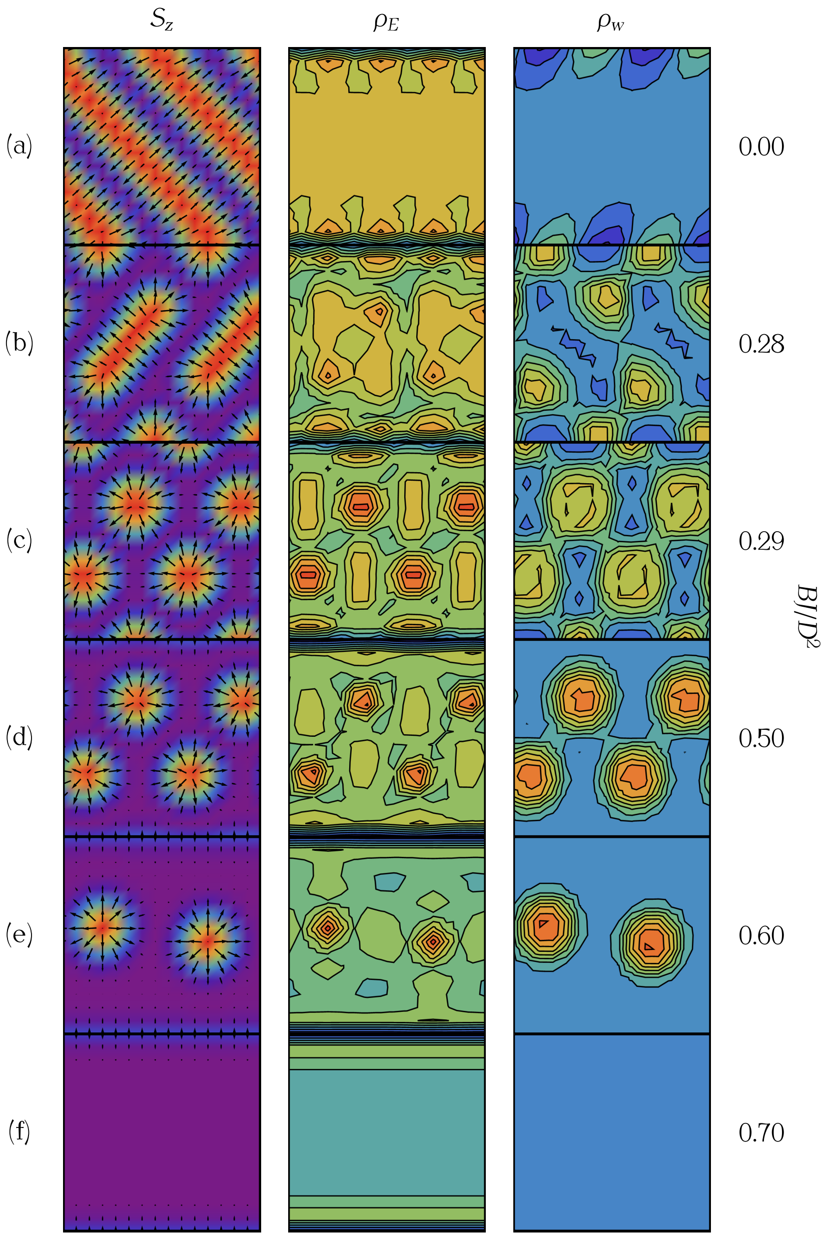

Figure 1.3. Magnetization (left column), energy density ρ_E (central column), and topological charge density ρ_w (right column) for different values of the field for a square system with linear size $L = 16$ with periodic boundaries in the horizontal direction. The pitch lengh is $p = 7$ and the temperature is zero. The color coding indicates out of plane magnetization (left column) and energy and topological charge densities (central and right column).

the field through the skyrmion phase to zero. The precise configuration depends on the ratio of system size to pitch length. In Fig. 1.3 we show the situation for a wire geometry with linear size $L = 16$ and one periodic boundary at zero temperature and for zero anisotropy. Starting from large fields (and hence from the polarized phase), at a certain field strength (see Fig. 1.1) the magnetic configuration changes from being uniformly polarized, into a configuration with skyrmions, upon lowering the field. As the distance between skyrmions depends on the field (with larger field leading to larger distance) the number of skyrmions increases discontinuously as the field is lowered. Roughly speaking, the number of skyrmions jumps once the field (and thus preferred skyrmion distance) is low enough to accommodate more skyrmions in the confined geometry. Note that this clearly depends on system size. For lower fields, the skyrmion configuration changes into a spiral state via a state where the skyrmions are elongated. Such extended skyrmions are reminiscent of "fingers" in liquid crystals that appear in many varieties [38, 39, 40]. Also note that for low enough fields half skyrmions appear at the edge of the system. For very low fields, the spiral state is stabilized and in the middle of the system the elongated skyrmions and spirals orient themselves 90 degrees with respect to the lattice to maximize the period of the spiral (and thus minimize exchange energy). Similar anisotropies may very well be present in some materials and in our simulations result from the underlying lattice. For simulations that would need to give quantitative predictions for continuum systems, one could add additional terms that make the exchange interactions more isotropic [58]. Here, we do not pursue this route as we are interested in the qualitative features of the phases and cascade of phase transitions. At the edge of the wire the influence of exchange is less important with respect to DM interactions and the spirals are parallel to the edge. Because of the strong easy-plane anisotropy of MnSi thin films, Wilson *et al.* considered helicoids with wave vector perpendicular to the edges, and, moreover, only considered edge states without internal structure [63]. In the geometry we consider, the edge states may also consist of half skyrmions, and, as a result, the spiral states that finger out of the skyrmions and half skyrmions upon lowering the field will have their wave vector parallel to the edges of the wire. Again, we note that several of the features we dicuss, such as half and elongated skyrmions, and spiral orientation at the edges, were very recently experimentally observed by Du *et al.* for Bloch skyrmions [65].

In Fig. 1.3 we show, in addition to the magnetization in the top row, the energy density ρ_E [the expectation value of the summand in Eq. (1.4)] in the middle row of figures, and the topological charge (winding number) density ρ_w [integrand in Eq. (1.5)] in the bottom row, where the brighter colors indicate higher values. At the skyrmion (and half skyrmion) positions the energy is largest as the spin at the skyrmion core points opposite to the external field. We also note that the figure of the magnetization clearly shows edge states where the magnetization tilts away from the field direction at the boundaries of the system [69]. The middle row shows that the energy density is minimized at the edges. Note that for low enough field the half skyrmions at the edge are formed from these edge states, as was also discussed in Ref. [71] for Bloch skyrmions. We note that in structures where half skyrmions appear the edges show alternating positive and negative contributions to the winding number, while in the skyrmion phase the contributions to the winding number are positive and due to the skyrmions only.

4 Degeneracies and fluctuations

At the transitions between different magnetic configurations as a function of field, two magnetic configurations are degenerate. Such degeneracies occur generically in a confining geometry as a function of field, ratio of DM to exchange interaction, or system size, because the geometry prevents the skyrmions from reaching their preferred (in an infinitely large system) position. This leads, at some particular set of values of the parameters, e.g. to a degeneracy between a state with fewer but larger skyrmions and a state with more but smaller skyrmions. An example of two degenerate spin configurations is given in Fig. 1.4. In this figure, the skyrmions are elliptical as the edge states effectively push the skyrmions away from the boundaries [69] thereby deforming the skyrmions. Skyrmion deformation due to anisotropy was discussed in Ref. [62]. We now turn to the question of how fluctuations lift zero-temperature degeneracies between two magnetic configurations, in particular for degenerate configurations containing a different number of skyrmions.

To investigate this in detail we look again at a wire geometry of size $L \times L = 16 \times 16$ with $KJ/D^2 = 0.0$ and $BJ/D^2 = 0.5$. We vary the pitch length p and determine the classical energy of different skyrmion configurations. These energies are found by initiating the simulations with a certain number of skyrmions and using simulated annealing to force the configuration to an energetic local minimum at zero temperature. The upper panel of Fig. 1.4(a) shows the classical ground-state energies for various configurations as a function of the pitch length relative to the energy of a system without any skyrmions. There is a range of pitch lengths $5.5 \lesssim p \lesssim 13.5$ for which the classical ground state is a configuration containing skyrmions.

We note that a similar result can be obtained by varying the system size rather than the pitch length, since the ratio between these two length scales determines the preferred amount of skyrmions in the system. This means that for a given material with certain values for J, D, and K and some applied magnetic field such that skyrmions are expected, wires can be made with a certain thickness so that their classical magnetic ground state is degenerate.

To investigate the effect of quantum and thermal spin-wave (magnon) fluctuations at zero and nonzero temperature, respectively, we use the method outlined in Refs. [72] and [73]. We quantize the spins and use a Holstein-Primakoff transformation to bosonic operators $\hat{a}_{\boldsymbol{r}}$ and $\hat{a}^\dagger_{\boldsymbol{r}}$. It is given by

$$\begin{aligned} \hat{\boldsymbol{S}}_{\boldsymbol{r}} \cdot \boldsymbol{\Omega}_{\boldsymbol{r}} &= S - \hat{n}_{\boldsymbol{r}} \, ; \\ \hat{S}^-_{\boldsymbol{r}} &= \hat{a}_{\boldsymbol{r}} \sqrt{2S - \hat{n}_{\boldsymbol{r}}} \; , \end{aligned} \tag{1.6}$$

where $\hat{S}^-_{\boldsymbol{r}}$ is the usual spin-lowering operator and $\hat{n}_{\boldsymbol{r}} = \hat{a}^\dagger_{\boldsymbol{r}} \hat{a}_{\boldsymbol{r}}$. Moreover, $\boldsymbol{\Omega}_{\boldsymbol{r}}$ denotes the classical spin configuration that is found from the simulations at zero temperature and S is the spin quantum number (which we take equal to one as the simulations are done for normalized spins). We insert the above transformation in the hamiltonian and keep terms up to quadratic order in the creation and annihilations operators which amounts to a linear approximation in which interactions between spin waves are neglected, which is sufficient for low temperatures. The hamiltonian acquires terms $\sim \hat{a}\hat{a}$ and $\sim \hat{a}^\dagger \hat{a}^\dagger$ that are removed by a Bogoliubov transformation to new bosonic operators $\hat{\gamma}^\dagger_i$ and $\hat{\gamma}_i$ that respectively create and annihilate a spin wave with energy ϵ_i. Here, i is an index that labels the spin-wave modes. After the Bogoliubov transformation, the hamiltonian is in the above-mentioned harmonic approximation given by [72]

$$H = E_{\text{cl}} + E_0 + \sum_i \epsilon_i \left(\hat{\gamma}^\dagger_i \hat{\gamma}_i + \frac{1}{2} \right) \, . \tag{1.7}$$

The first term is the classical ground-state energy as found in the simulations whereas the second term is a quantum contribution that arises in the Bogoliubov approach outlined aboved. This latter contribution is absent at the classical level.

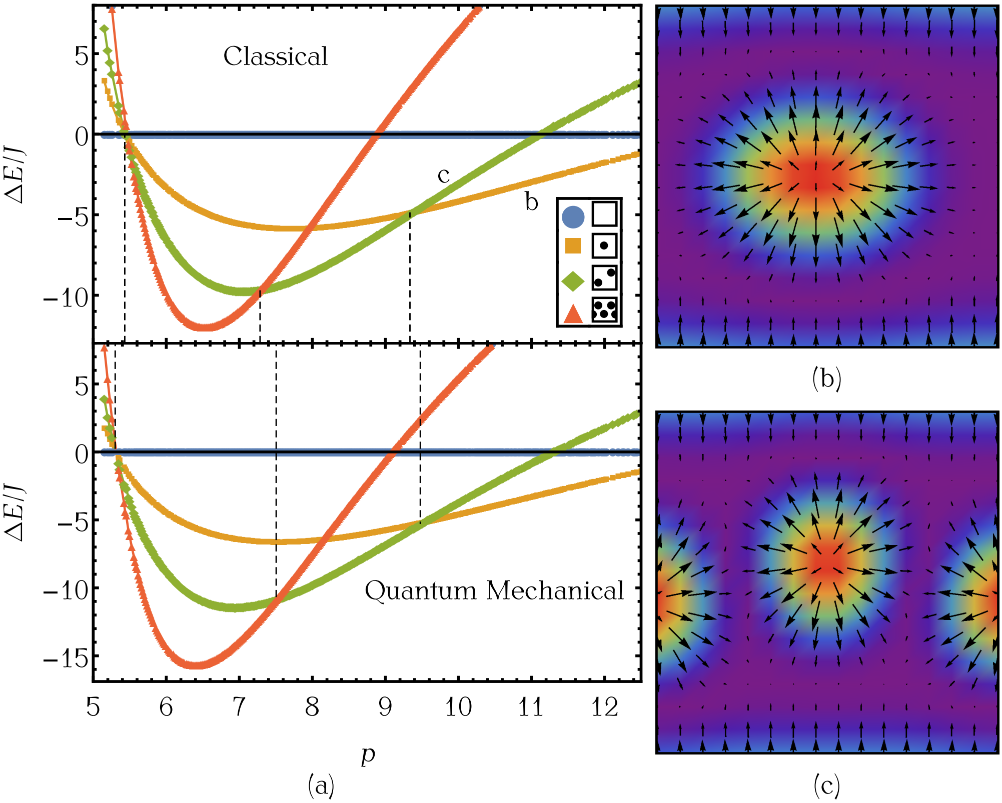

Figure 1.4. (a): Difference in energy (upper panel: classical energy, lower panel: energy including quantum correction) between configurations with skyrmions and the state without skyrmions at zero temperature versus pitch length, for various numbers of skyrmions and system size $L \times L = 16 \times 16$ with one periodic and one open boundary and parameters $KJ/D^2 = 0.0$ and $BJ/D^2 = 0.5$. The blue circular, yellow rectangular, green diamond-shaped, and red triangular data points correspond to systems with 0, 1, 2, and 4 skyrmions respectively. (b) and (c): Magnetic configuration of two classically-degenerate ground states with energy $E = -596.17J$ of a system at pitch length $p = 9.336$ deep in the skyrmion regime with one periodic (horizontal direction) and one open (vertical direction) boundary.

Using the above hamiltonian, the ground-state energy including quantum corrections is found to be

$$E = E_{\mathrm{cl}} + E_0 + \sum_i \frac{\epsilon_i}{2} \ . \tag{1.8}$$

At a point where two magnetic configurations in our simulations are found to be degenerate, the first term E_{cl} is equal for them. The spin-wave spectrum (and hence the quantum correction represented by the last two terms in the above expression for the energy) is, however, generically different for two classically degenerate configurations, so that quantum fluctuations may indeed remove classical degeneracies. In the lower panel of Fig. 1.4(a) we show the energy including quantum corrections for magnetic configurations containing up to four skyrmions as a function of pitch length and for the same parameters as the upper panel of this figure. This result shows that the energies are shifted by the quantum corrections. Moreover, they are shifted in such a way that the region where the configuration with four skyrmions is the true lowest-energy state is enlarged with respect to the classical result. This conclusion is in line with the finding of Roldán-Molina *et al.* [73] that quantum fluctuations stabilize skyrmion textures over the collinear ferromagnetic phase. Loosely speaking this comes about because larger gradients in the spin direction lead to more quantum fluctuations.

Having discussed the effect of quantum, i.e., zero-temperature, fluctuations, we now turn to thermal fluctuations. To investigate which configuration is entropically preferred, we i) compute the entropy due to the spin waves around two degenerate skyrmion configurations (an approach appropriate at low temperatures), and ii) directly measure the relative probability of occurrence of configurations at nonzero temperatures within our simulations (and approach valid at intermediate and high temperatures). In the first approach the spin waves (or magnons) are considered as non-interacting bosonic particles thus taking into account their quantum statistics. We refer to this approach as the spin-wave analysis.

We look at a system with $p = 9.336$ and $p = 7.284$. At these values of the pitch length, the classically degenerate ground states contain either one or two skyrmions for $p = 9.336$ as in Fig. 1.4 or two or four skyrmions for $p = 7.284$. At nonzero temperature, the total energy of the system is in the harmonic approximation given by

$$E(T) = E_{\mathrm{cl}} + \sum_i \epsilon_i n_i \ , \tag{1.9}$$

with the Bose-Einstein distribution function $n_i = [\exp(\beta\epsilon_i) - 1]^{-1}$. In the above equation and following discussion we neglect the quantum corrections to the energy discussed previously. The spin-wave entropy is given by

$$S(T) = -k_B \sum_i \left[n_i \ln n_i - (1 + n_i) \ln(1 + n_i)\right] . \tag{1.10}$$

Since the simulations are classical we expect them to correspond to the Rayleigh-Jeans limit, $n_i \to 1/\beta\epsilon_i$, of the above formulas, which leads to equipartition of energy such that in this limit the total energy is equal to Nk_BT, with N the number of spins. In Fig. 1.5 we display the average energies of the degenerate ground states as a function of temperature. As expected, at low temperatures the simulation agrees with this classical equipartition result, whereas the quantum-mechanical result is suppressed with respect to equipartition. This is because apart from a few (nearly) zero modes, most spin-wave excitations have energies $\sim B$, such that at temperatures $k_BT \ll B$ our simulations overestimate their contribution to the energy. The deviation of the simulations from equipartition at high temperatures is because in this limit the harmonic approximation starts to break down.

At nonzero temperatures, the probability of the system being in one out of two degenerate ground states depends on their difference in entropy. Besides the entropy due to magnons there is also translational entropy that depends on the number of skyrmions, and that needs to be included in the overall entropy of a configuration. The simulations automatically include this extra entropy, but it is not accounted for in the expression in Eq. (1.10) and needs to be included on top of this expression. For example, the skyrmion configurations in Fig. 1.4 can be translated in the periodic direction by a lattice constant. For a single skyrmion there are 16 (for system size 16 in the periodic direction) translations, whereas for two skyrmions the configuration can be mapped onto itself by a translation over 8 lattice site in combination with a reflection. Hence, the configurations with one and two skyrmions have the same translational entropy. Similar counting leads to the conclusion that there are twice as much translations possible for the situation of two, as compared to four skyrmions so that the translational entropy of the configuration with two skyrmions is $k_B \ln 2$ higher than that of four skyrmions.

Figure 1.6 displays the ratio of probabilities for occurrence of skyrmion configurations with different number of skyrmions: two and one skyrmions for $p = 9.336$, and four and two skyrmions for $p = 7.284$, as a function of temperature. In this figure, both simulation results (dots) and results from

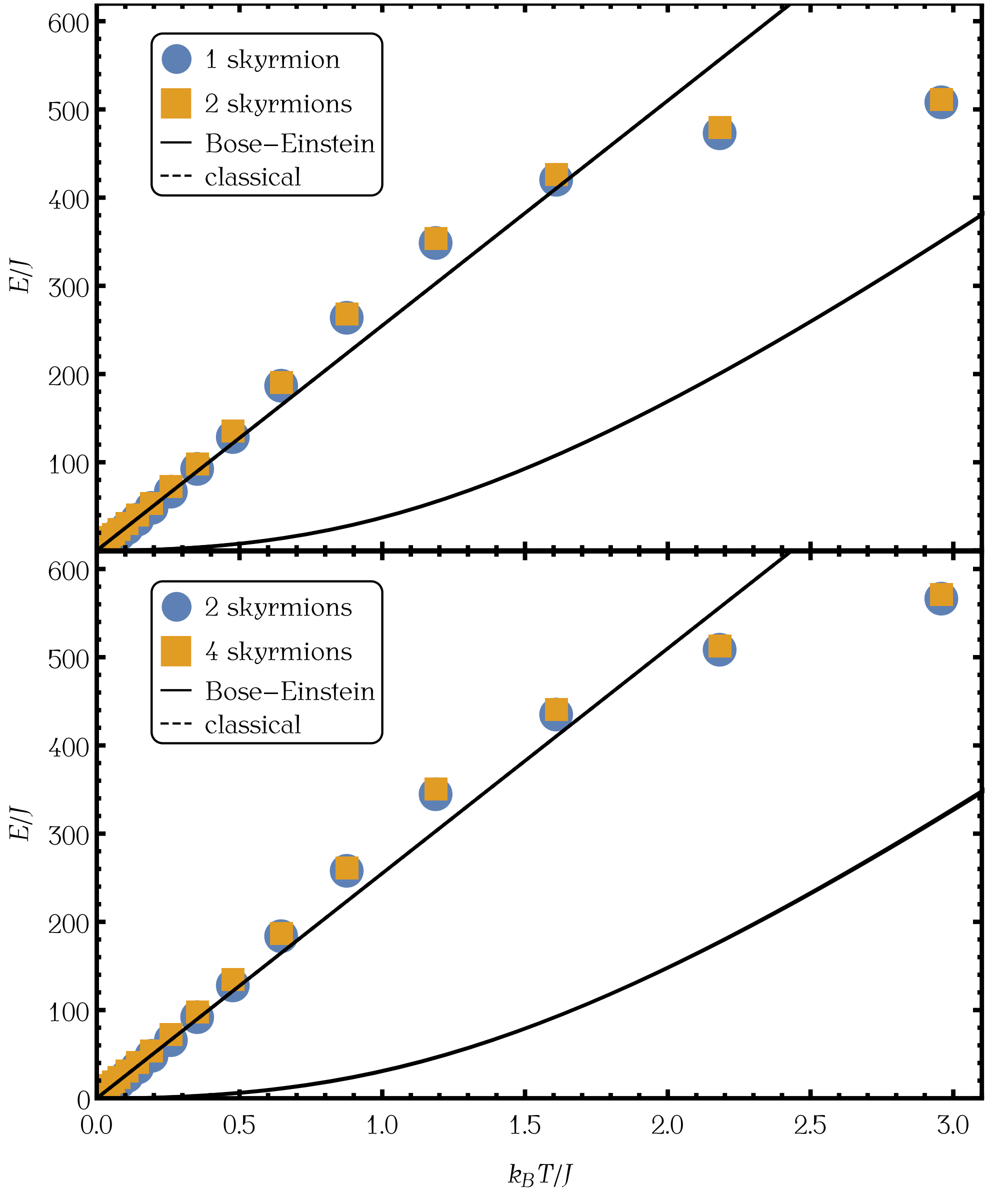

Figure 1.5. The energy of various spin configurations, with pitch length $p = 9.336$ (top panel) and $p = 7.284$ (bottom panel), as a function of temperature $k_B T/J$ and where E_{cl} is put equal to zero. In both cases the parameters are $KJ/D^2 = 0.0$ and $BJ/D^2 = 0.5$. The data points represent data from Monte Carlo simulations that are in agreement with results from the equipartition theorem at low temperatures (shown by the black dashed line). The solid black lines represent the energies resulting from the spin-wave analysis.

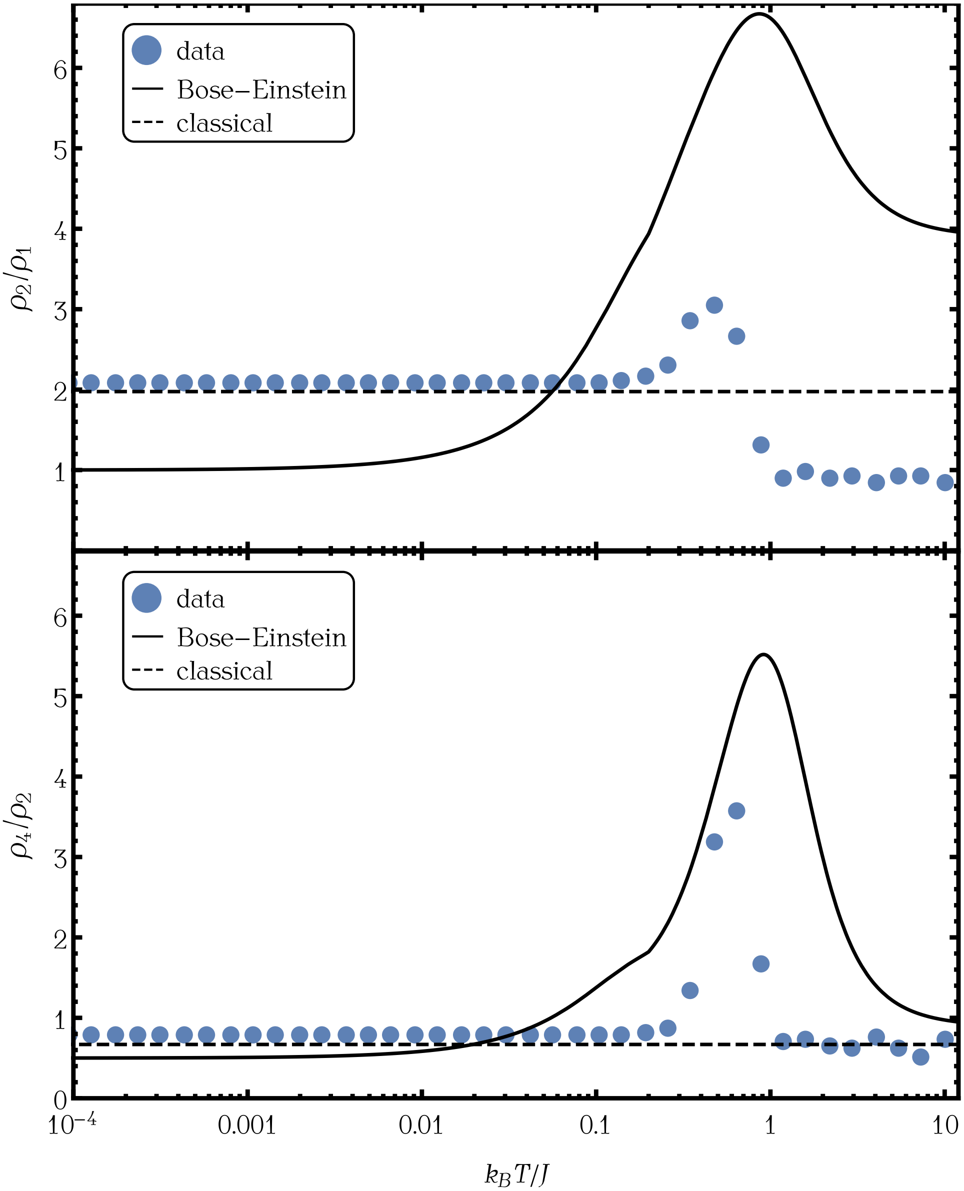

Figure 1.6. Ratio of probabilities of having a certain amount of skyrmions for two different situations with parameters $KJ/D^2 = 0.0$ and $BJ/D^2 = 0.5$ and pitch length $p = 9.336$ (top panel) and $p = 7.284$ (bottom panel) as a function of temperature. The dots correspond to results from the Monte Carlo simulations, the solid-line from the spin-wave analysis not including translation entropy, and the dashed line to the zero-temperature classical limit.

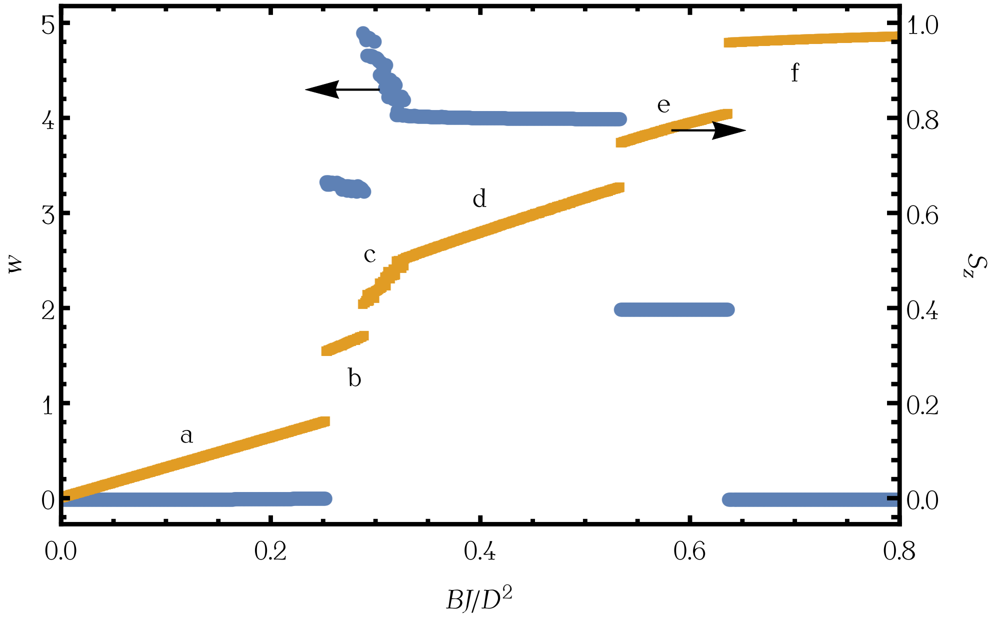

Figure 1.7. Winding number (left axis) and average magnetization in the z-direction (right axis) as a function of magnetic field for the same parameters as Fig. 1.3. Labels a-f refer to states in Fig. 1.3. All parameters are taken the same as for the results in Fig. 1.3.

the spin-wave analysis without the translational entropy are shown (black solid line). The probability that results from the classical limit of the entropy [Eq. (1.10) with the replacement $n_i \to 1/\beta\epsilon_i$, dashed black line] leads to a probability ratio that agrees with the low-temperature limit of our simulations, where the ratio was measured by cooling a system down 10^4 times while measuring the number of skyrmions in the system. According to the spin-wave analysis, the probability ratio is in the low-temperature only determined by translation entropy. Both the quantum-mechanical result for the entropy as well as the simulations show a peak around the ferromagnetic phase transition $k_B T/J \sim 1$. At moderate temperatures $(0.1J - 0.5J)$ our results show that the configuration with the most skyrmions is entropically favored.

5 Conclusions, discussion, and outlook

In this chapter we have shown that in finite systems and at elevated temperatures skyrmions are present in a large part of the phase diagram. We have also discussed how the magnetic field tunes the system through a cascade of transitions between different magnetic configurations, and how zero-temperature degeneracies between such magnetic configurations are lifted by fluctuations. Throughout this chapter we have focused on PMA materials where the DM interactions are believed to arise due to interfaces between very thin layers of magnetic materials (such as Co) and materials with strong spin-orbit coupling (such as Pt) [48, 49, 50, 51]. Such DM interactions give rise to Néel skyrmions. Because the magnetic layers in these system are very thin (only a few atoms), our two-dimensional treatment is appropriate. In particular, the two-dimensional nature and form of the DM interactions prevent the formation of conical phases in the phase diagram. This situation is different from the situation of thin films of MnSi in which Bloch skyrmions are stabilized and conical phases are present [62, 63].

In this chapter we have focused on the confined geometry of a wire. The cascade of transitions as a function of field is generic and appears for any confined geometry because the field influences the preferred skyrmion distance. Which particular magnetic structures occur in the cascade depends on the confined geometry, however, and on the form of the DM interactions and anisotropy. In particular, we expect that the half-skyrmions that we have found will only appear in a wire geometry.

Jumps in the magnetoresistance in MnSi nanowires have been observed recently, and were attributed to changes in the number of skyrmions in the magnetic configuration [64]. Measurements of changes in the topological Hall effect due to the appearance of single skyrmions in a confined geometry were performed on FeGe [74]. Motivated by these experiments we now investigate whether the transitions between various configurations that appear in our system as a function of field (see Fig. 1.3) can be detected electrically. To this end, we compute the total winding number and the total magnetization in the z-direction as a function of field for the same parameters as Fig. 1.3 (see Fig. 1.7). The total winding number determines (up to prefactors) the topological Hall signal, provided spin-orbit coupling is small [75, 76]. The result in Fig. 1.7 clearly shows jumps in the winding number as the magnetic configuration undergoes a structural transition. For PMA materials, however, the topological Hall signal is expected to be very small [77]. An alternative for electrical detection of the magnetization configuration is then the anomalous Hall signal that is proportional to the total magnetization in the z-direction for our geometry. Figure 1.7 shows that this quantity also jumps as the magnetization configuration undergoes a transition as a function of field. Based on this analysis we conclude that the transitions between various magnetic configurations that have we found may be detected electrically.

Using experimental parameters for PMA materials from Ref. [48] we estimate that $KJ/D^2 \sim -1$ and $BJ/D^2 \sim 10^{-4} - 10^{-1}$ for these experiments. The route to observe skyrmions in these systems would therefore be to increase the field and lower the anisotropy (or preferably make it easy-plane). Very recently, Moreau-Luchaire *et al.* have reported the observation of skyrmions at room temperature in multilayers of Co and Pt with PMA [78]. The skyrmions observed in these measurements are rather large and stabilized as a result of both dipole-dipole and DM interactions, and are therefore in a somewhat different regime from the skyrmions that we have studied in this chapter.

In future work, we will investigate how current-induced torques manipulate the skyrmionic magnetic structures we have found. Finally, motivated by the recent experimental results of Du *et al.* [65] we also intend to consider Bloch skyrmions.

2 Skyrmions in square-lattice antiferromagnets

The ground states of square lattice two-dimensional antiferromagnets with anisotropy in an external magnetic field are determined using Monte Carlo simulations and compared to theoretical analysis. We find a new phase in between the spin–flop and spiral phase that shows strong similarity to skyrmions in ferromagnetic thin films. We show that this phase arises as a result of the competition between Zeeman and Dzyaloshinskii-Moriya interaction energies of the magnetic system. Moreover, we find that isolated (anti-)skyrmions are stabilized in finite-sized systems, even at higher temperatures. The existence of thermodynamically stable skyrmions in square-lattice antiferromagnets provides an appealing alternative over skyrmions in ferromagnets as data carriers.[1]

1 Introduction

Skyrmions have been the topic of intense research, in ferromagnetic materials [41, 42, 43, 44, 57, 58, 59, 61, 66] as well as numerous other systems [35, 36, 37, 38, 39, 40]. Skyrmions in ferromagnets have promising characteristics that make them suitable for data storage and transfer: they can be driven by low critical currents [45, 46], and they are able to move past pinning sites [79].

Skyrmions in antiferromagnetic (AFM) thin films are perhaps more suitable as data carriers than their ferromagnetic counterparts. Firstly, antiferromagnets are more prevalent in nature than ferromagnets, allowing for a wider range of material properties. Secondly, skyrmions in an antiferromagnet are less sensitive to magnetic fields. Thirdly, they move faster, and in the direction of the charge current (while skyrmions in ferromagnets experience a Magnus force with a significant component perpendicular to their trajectory), which makes it easier to control them [80]. For these reasons, skyrmions have been investigated in many different antiferromagnetic systems, ranging from doped bulk materials [81], Bose-Einstein condensates [82], various triangular lattice antiferromagnets [83, 84], to nanodisks [85]. Isolated AFM skyrmions [86, 87], as well as moving skyrmions in AFMs have been considered theoretically [88, 89, 90].

---

[1] The contents of this chapter are largely based on the work of R. Keesman, M. Raaijmakers, A. E. Baerends, G. T. Barkema, and R. A. Duine [2]. M. Raaijmakers and A. E. Baerends were actively involved in the construction of the hamiltonian density in Eq. (2.2) and calculating the energy densities of various phases as described in Sec 2.5. We thank A. Roldán-Molina and A. S. Núñez for their feedback.

In this chapter we study thermodynamically stable inhomogeneous magnetization textures in square-lattice antiferromagnets (SLA's) with Dzyaloshinskii-Moriya (DM) interactions. The DM interactions that we consider arise either from bulk inversion asymmetry (symmetry class C_{nv}) or from structural inversion asymmetry along the thin-film normal direction. An example of the latter is an interface between a magnetic metallic system and a non-magnetic metal with strong spin-orbit coupling. For ferromagnetic systems, tunable interface-induced DM couplings have indeed been demonstrated [48, 49, 50, 51, 52, 53, 54]. Such interfaces typically also give rise to perpendicular anisotropies, which we therefore also take into account. Finally, we also consider an external magnetic field normal to the thin film. Previous work by Bogdanov *et al.* [86] considered the same system at zero temperature and in the continuum limit. These authors identified three phases: an antiferromagnetic phase, a spin–flop phase, and a phase where inhomogeneous structures persist. While examples of structures in the latter phase were given, no further phase boundaries were identified within this phase. One of our main results is that we find a distinct phase pocket that bounds a $2q$ skyrmionic phase and separates it from a spiral ($1q$) phase. Furthermore, while in infinite systems skyrmions are not found as thermodynamically stable regions of the phase diagram, we confirm the existence of stable skyrmions in finite-sized systems below the Curie temperature.

The chapter is organized as follows: first, we present the system under study, by defining the hamiltonian that is used in Monte Carlo (MC) simulations. After that, we discuss the various spin textures and their characteristics that arise in SLA's. We also construct the phase diagram from MC simulations, complemented by analytical results based on a continuum model. We dedicate the last two sections to the interaction energies of skyrmions, and to skyrmions in finite-sized systems, respectively, after which we conclude with a discussion and summary of our results.

2 Model

We are interested in the equilibrium spin configurations in films of SLA materials. For this purpose, we consider a square lattice of length L in the xy-plane with Heisenberg spins $\boldsymbol{S_r}$ of unit length at position $\boldsymbol{r}$. Nearest neighboring spins are coupled through an antiferromagnetic Heisenberg term $J > 0$ and a Dzyaloshinskii-Moriya term D and are affected by anisotropy K and an external magnetic field B in the $\hat{\boldsymbol{z}}$-direction. The effective hamiltonian that is used in our MC simulations is given by

$$\begin{aligned} H =& J \sum_{\boldsymbol{r}} \boldsymbol{S_r} \cdot \left(\boldsymbol{S}_{\boldsymbol{r}+\hat{\boldsymbol{x}}} + \boldsymbol{S}_{\boldsymbol{r}+\hat{\boldsymbol{y}}} \right) \\ &+ K \sum_{\boldsymbol{r}} (\boldsymbol{S_r} \cdot \hat{\boldsymbol{z}})^2 - B \sum_{\boldsymbol{r}} \boldsymbol{S_r} \cdot \hat{\boldsymbol{z}} \\ &- D \sum_{\boldsymbol{r}} \left(\boldsymbol{S_r} \times \boldsymbol{S}_{\boldsymbol{r}+\hat{\boldsymbol{x}}} \cdot \hat{\boldsymbol{y}} - \boldsymbol{S_r} \times \boldsymbol{S}_{\boldsymbol{r}+\hat{\boldsymbol{y}}} \cdot \hat{\boldsymbol{x}} \right). \end{aligned} \tag{2.1}$$

For theoretical analysis, we consider a continuous field description of the discrete hamiltonian in Eq. (2.1) (see also Ref. [9]). Because of the antiferromagnetic nature of these materials, it is natural to define sublattices with magnetization $\boldsymbol{m}_1$ and $\boldsymbol{m}_2$ organized in a checkerboard configuration and put the lattice constant to unity. For antiferromagnets with large Heisenberg interaction we expect slowly varying periodic structures and the staggered magnetization $\boldsymbol{l} = (\boldsymbol{m}_1 - \boldsymbol{m}_2)/2$ to be large while the total magnetization $\boldsymbol{m} = (\boldsymbol{m}_1 + \boldsymbol{m}_2)/2$ is expected to be much smaller, ie, $|\boldsymbol{l}| \approx 1$ and $|\boldsymbol{m}| \ll |\boldsymbol{l}|$ [91]. We also assume that the spatial derivatives of $\boldsymbol{m}$ can be neglected and that the contribution of the total magnetization to the anisotropic term is negligible compared to that of the staggered magnetization. This results in the following hamiltonian density

$$\begin{aligned} \mathcal{H} =& \frac{J}{2} \left[\left(\frac{\partial \boldsymbol{l}}{\partial x} \right)^2 + \left(\frac{\partial \boldsymbol{l}}{\partial y} \right)^2 + 8\boldsymbol{m}^2 \right] - Bm_z + Kl_z^2 \\ &+ D \left(l_z \frac{\partial l_x}{\partial x} - l_x \frac{\partial l_z}{\partial x} + l_z \frac{\partial l_y}{\partial y} - l_y \frac{\partial l_z}{\partial y} \right). \end{aligned} \tag{2.2}$$

Since spins are normalized to unity, such that $|\boldsymbol{m}_i| = 1$, the staggered and total magnetization must satisfy $\boldsymbol{m}^2 + \boldsymbol{l}^2 = 1$ and $\boldsymbol{m} \cdot \boldsymbol{l} = 0$ and minimizing the hamiltonian density results in $\boldsymbol{m} = -\boldsymbol{l} \times (\boldsymbol{l} \times \boldsymbol{h})/(8J)$. Substitution leads to a hamiltonian density that is only dependent on the staggered magnetization:

$$\begin{aligned}\mathcal{H} =& \frac{J}{2}\left[\left(\frac{\partial \boldsymbol{l}}{\partial x}\right)^2 + \left(\frac{\partial \boldsymbol{l}}{\partial y}\right)^2\right] + \frac{B^2}{16J}\left[l_z^2 - 1\right] + K l_z^2 \\ &+ D\left(l_z \frac{\partial l_x}{\partial x} - l_x \frac{\partial l_z}{\partial x} + l_z \frac{\partial l_y}{\partial y} - l_y \frac{\partial l_z}{\partial y}\right).\end{aligned} \tag{2.3}$$

Our simulations focus on systems for which the DM coupling and the coupling to the magnetic field are of the order of the Heisenberg coupling but assume that anisotropy strength is small. For small fields all higher order interactions like dipole-dipole interactions are negligible in antiferromagnets because the net magnetization is small. Note that the continuous field description is only valid for small fields and small DM coupling where modulations are large compared to the lattice distance.

3 Phases

We find that systems described by the hamiltonian given by Eq. (2.1) have four distinct phases at zero temperature: the antiferromagnetic and spin–flop phase are both homogeneous, whereas the spiral and $2q$ phases are modulated, i.e., inhomogeneous phases with 1 and 2 dominating wave modes respectively.

There are two homogeneous phases: the antiferromagnetic phase in which the staggered magnetization points along the z-axis, and the spin–flop phase in which the staggered magnetization lies in the xy-plane. The spiral phase emerges for large enough DM coupling for which the staggered magnetization shows the same characteristics as ferromagnetic spins in a spiral state. Finally, there is a bounded region for which the $2q$ phase emerges, which has a similar texture to the spiral phase but in which the width of the spirals varies in length periodically. Configurations of these phases in real space, in terms of the staggered magnetization, and the norm of their Fourier modes are shown in Fig. 2.1. The Fourier modes are defined as

$$\boldsymbol{A}_{\boldsymbol{q}} = \frac{1}{L^2}\sum_{\boldsymbol{r}} \boldsymbol{S}_{\boldsymbol{r}} \exp\left[\frac{2\pi i}{L}\boldsymbol{q}\cdot\boldsymbol{r}\right]. \tag{2.4}$$

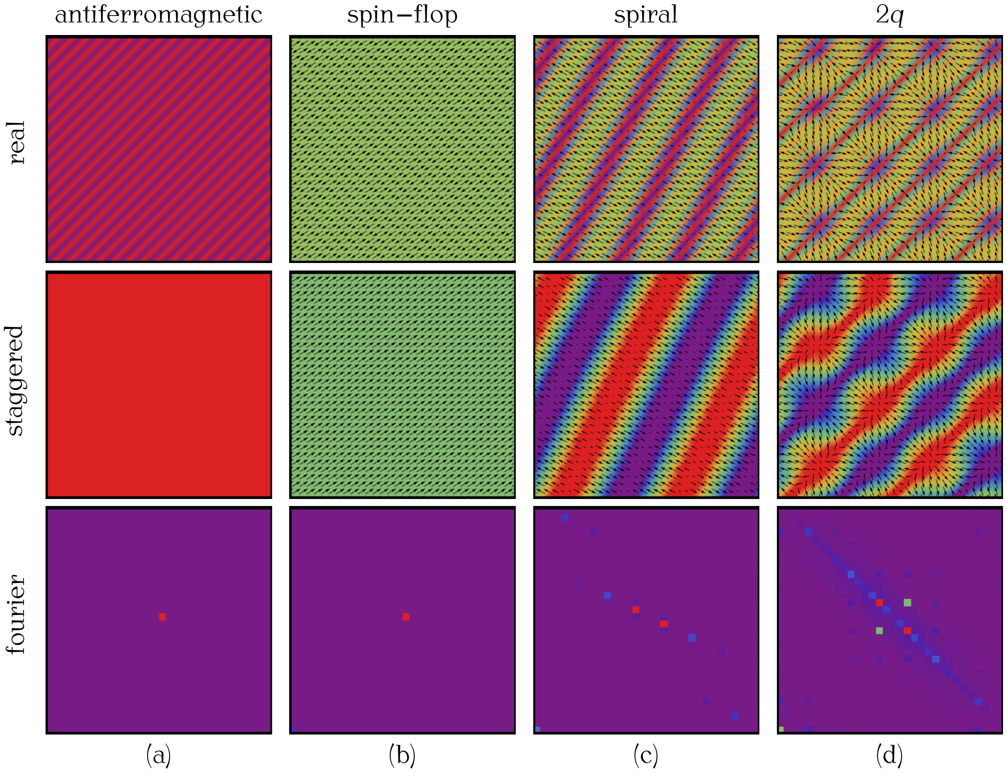

(a) (b) (c) (d)

Figure 2.1. Various types of configurations encountered in MC simulations of the model described by the Hamiltonian in Eq. (2.1). The antiferromagnetic (a), spin–flop (b), spiral (c), and $2q$ phase (d) are shown from left to right in typical real spin configuration (top) and staggered magnetization (middle) for an antiferromagnetic system of size $L = 32$ at zero temperature. The arrows represent the local magnetization in the xy-plane and the background colour shows the magnetization pointing up (red) or down (purple). The norm of the Fourier modes (bottom), as defined in Eq. (2.4), of these configurations show the distinctive modes that define the phases.

4 Phase diagram from simulations

In one elementary move of our MC simulations, a random spin is selected and replaced by a new spin vector, drawn uniformly from a spherical cap around the original spin vector. The size of this cap is chosen such that the acceptance rate in the Metropolis algorithm is roughly 50%. The time step is defined such that each spin makes an elementary move once per unit of time. At each temperature typically 4500 time steps are taken before measurements are done. During annealing, the temperature is reduced from well above the critical temperature to well below it in 200 temperature steps. These measurements result in data obtained over a wide range of parameters and temperatures.

We consider the Fourier transform of the spin vectors as defined by Eq. (2.4) below. All four phases can be characterized by Fourier peaks. We define the homogeneous, spiral, and $2q$ phases as having 1, 2, or 4 nonzero-mode peaks respectively. To construct the phase diagram from Monte Carlo simulations based on the discrete hamiltonian from Eq. (2.1) we first anneal 10 different systems of size $L = 32$ at some parameter values J, D, B, and K. From these states the one with the lowest energy is chosen, and the process is repeated for different parameter values. For all these prospective ground states the phase and the area in the phase diagram for which they have the lowest energy is determined. From this the B-D-phase diagram can be constructed for various values of anisotropy K. The phase diagrams are qualitatively different for systems with easy-axis ($K < 0$) or easy-plane ($K > 0$) anisotropy, as can be seen in Fig. 2.2.

5 Analytical phase diagram

We also construct the phase diagram by using a number of Ansätze for the various phases. The parameters in these Ansätze are obtained from minimizing the hamiltonian density from Eq. (2.3) for these phases. For the antiferromagnetic phase we assume $\boldsymbol{l} = (0, 0, 1)$, resulting in an energy density $\mathcal{H}_{\mathrm{AF}} = K$. The spin–flop phase is characterized by $\boldsymbol{l} = (\cos\phi, \sin\phi, 0)$ with energy density $\mathcal{H}_{\mathrm{SF}} = -B^2/(16J)$. For the spiral phase, $\boldsymbol{l}$ is dominated by a rotation along the direction of the wave in the $(1, 1)$ direction such that $\boldsymbol{l} = (\sin(\boldsymbol{q}\cdot\boldsymbol{r})\cos\theta, \sin(\boldsymbol{q}\cdot\boldsymbol{r})\sin\theta, \cos(\boldsymbol{q}\cdot\boldsymbol{r}))$. Averaging over the length of one modulation and minimizing with respect to $\boldsymbol{q}$ leads to an energy density

$\mathcal{H}_{\mathrm{SP}} = -B^2/(32J) - D^2/(2J) + K/2$. A phase transition between the antiferromagnetic and spiral, and the spin–flop and spiral phase occurs along the lines

$$B = 4\sqrt{-(JK \pm D^2)}, \tag{2.5}$$

for easy-axis anisotropy. For easy-plane anisotropy, we assume for the spiral phase that the length is also variable, i.e., $\boldsymbol{l} = l(\sin(\boldsymbol{q} \cdot \boldsymbol{r}) \cos\theta, \sin(\boldsymbol{q} \cdot \boldsymbol{r}) \sin\theta, \cos(\boldsymbol{q} \cdot \boldsymbol{r}))$. Following the same procedure, we find that $l = \sqrt{B^2 + 8D^2 - 8JK}/B$ minimizes the energy. The energy density for the spiral is $\mathcal{H}_{\mathrm{SP}} = -(B^2 + 8D^2 - 8JK)^2/(32B^2J)$. In the case of easy-plane anisotropy, the phase transition between the spiral and spin–flop phase is then given by

$$B = 2\sqrt{2(1+\sqrt{2})}\sqrt{D^2 - JK}. \tag{2.6}$$

From simulations we find, as is explained further below, that the $2q$ phase lies in a K-independent regime of moderate values for D/J. With very small modulated structure like these, assumptions, such as very small total magnetization $\boldsymbol{m}$ do not hold any longer, and so the continous field description in Eq. (2.3) does not apply. These fast varying structures, including many higher-order Fourier modes, as can be seen in Fig. 2.1(d), mean a simple Ansatz, to reliably calculate energy densities for the $2q$ phase, could not be found.

We have constructed similar phase diagrams for various strengths of anisotropy $K/J \in 0, \pm 0.02, \pm 0.04, \pm 0.1$. The critical strengths B_0 at $D = 0$ and D_0 at $B = 0$ at which the transitions take place are obtained from Eqs. (2.5,2.6), yielding $B_0 \sim 4\sqrt{|JK|}$ and $D_0 \sim \sqrt{JK}$, consistent with results in Ref. [22]. These become larger for increasing strengths of anisotropy. In the simulations, the size of the system limits the longest wave length of the magnetization texture. For larger anisotropy, simulations in finite sytems are therefore in better agreement with analytical calculations. An interesting point is that the $2q$ phase is always sandwiched between the spin–flop and spiral phase, at constant values of DM interaction. Its size is relatively insensitive to the strength of anisotropy. This implies that the size of modulations in the $2q$ phase in antiferromagnets is related to the pitch length $p \sim J/D$, which is a measure for the length of modulation. Therefore, p only has a limited range of values, unlike the size of skyrmions in ferromagnets.

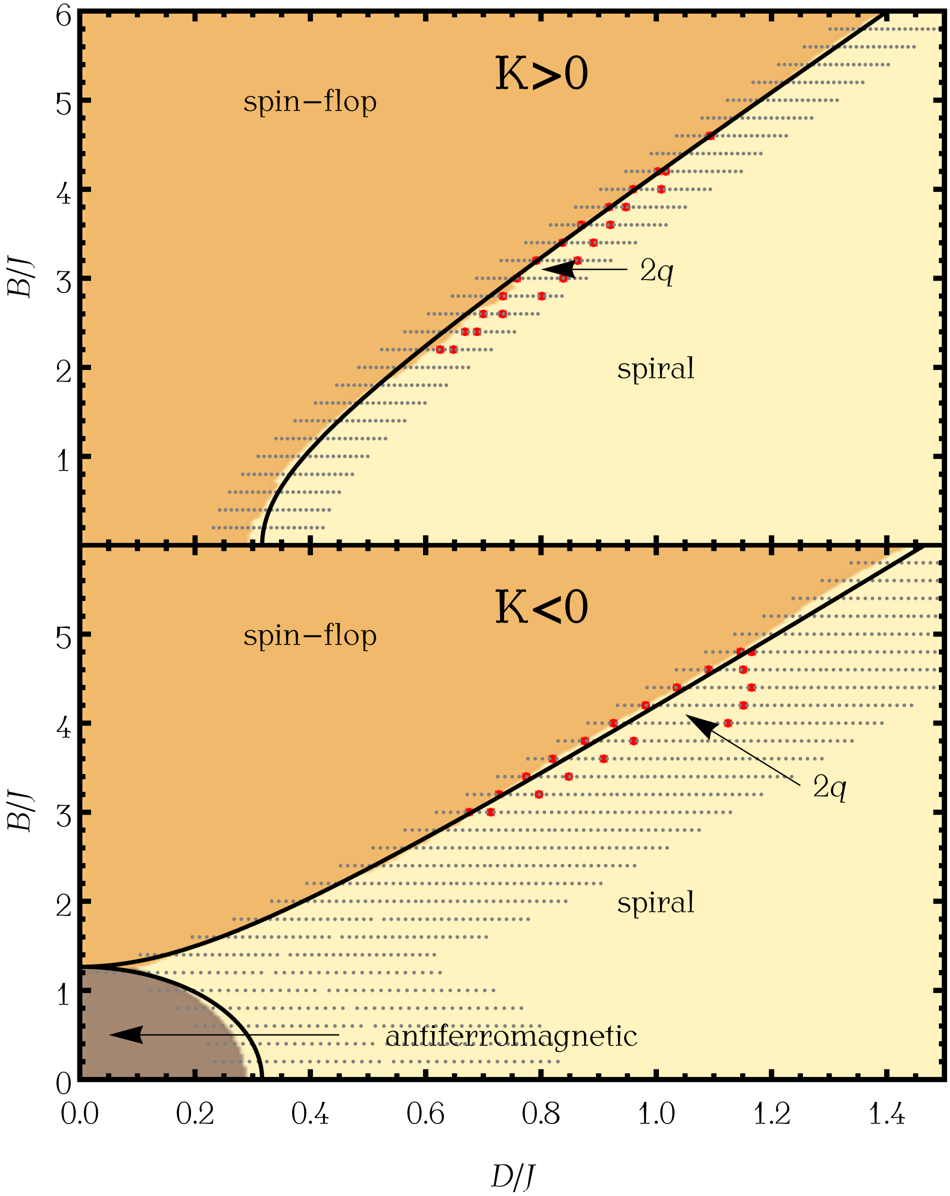

Figure 2.2. The complete B–D phase diagram for antiferromagnetic materials with easy-plane anisotropy $K/J = 0.1$ (top panel) and easy-axis anisotropy $K/J = -0.1$ (bottom panel) at zero temperature. The grey data points display parameter values at which Monte Carlo simulations were performed. From these simulations, the phases were determined, shown as different colours. The red data points show the boundary of the $2q$ phase, as obtained from these MC simulations for fixed values of B/J. The analytical solutions for the phase transitions as given by Eqs. (2.5,2.6) are shown as solid black lines.

6 Interaction energies

To investigate further the stability of the $2q$ phase in this model, we look at the energy contributions E of all interactions in the model along a line with fixed $B/J = 3.2$, through the $2q$ phase in the phase diagram. With increasing DM interaction and no anisotropy, there is a transition from the spin–flop phase to the $2q$ phase at $D/J = 0.76$. If the DM interaction is increased further, the spiral phase is entered at $D/J = 0.84$, as can be seen in Fig. 2.3. At the phase transition the contributions of the external field B and the DM interaction D to the total energy make distinctive jumps. While the spin–flop state minimizes the energy by having a net magnetization along the external field direction, the spiral mode makes optimal use of the DM interaction. The $2q$ phase gives a compromise between the two, and so a finite area between the two emerges in which neither of them is optimal, and the $2q$ phase prevails.

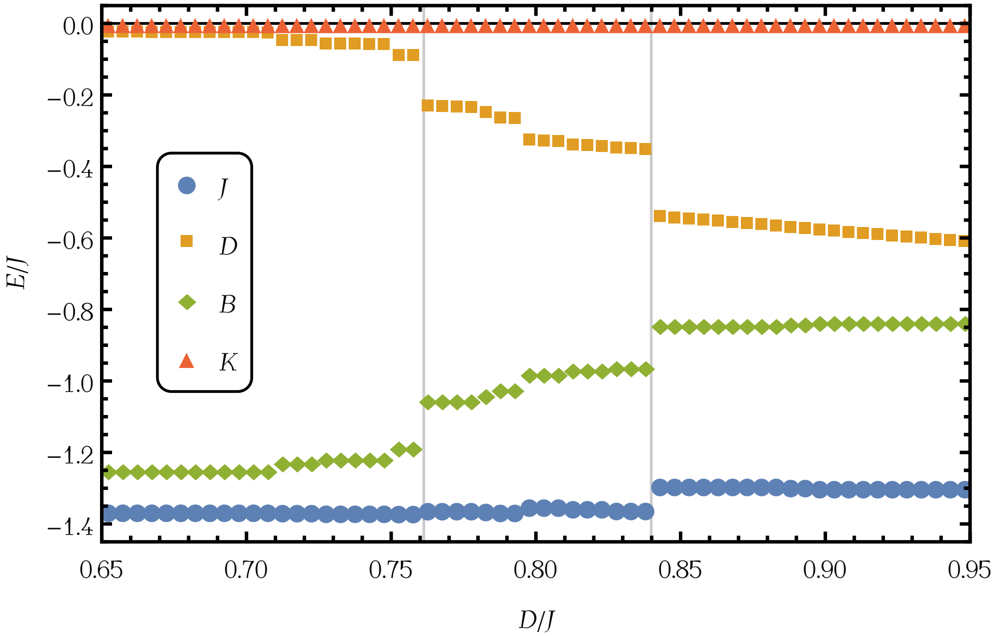

Figure 2.3. The energy contributions E/J to the ground state of the interactions with coupling parameters J, D, B, and K are shown as a function of D/J at parameter values $J = -1$, $B = 3.2$, and $K = 0$ for system of size $L = 32$. The system undergoes two phase transitions at $D/J = 0.76$ and $D/J = 0.84$ between the spin–flop, $2q$, and spiral phase, respectively. These are depicted as vertical grey lines. The discrete jumps in various energy contributions suggest first-order phase transitions.

7 Skyrmions

An important question is whether the objects in the $2q$ phase as shown in Fig. 2.1 can be called skyrmions, as they are not fully isolated topological objects. For a ferromagnet, the (anti)skyrmion is defined as a topological object for which the winding number w of the magnetization is nonzero:

$$w = \frac{1}{4\pi} \int dxdy\ \boldsymbol{n} \cdot \left(\partial_x \boldsymbol{n} \times \partial_y \boldsymbol{n}\right). \tag{2.7}$$

In case of the antiferromagnet, the winding number w of the staggered magnetization can be defined instead. Although the staggered magnetization in an antiferromagnet behaves similarly as the normal magnetization in a ferromagnet there are some distinctive differences. The antiferromagnet is symmetric under the $\boldsymbol{n} \to -\boldsymbol{n}$ transformation, such that there is no difference between a skyrmion and an antiskyrmion, and neither the up or down regime in terms of the staggered magnetization is favoured over long distances. Thus there can be no lattice of isolated thermally-activated topological objects like in a ferromagnetic system, without breaking this symmetry.

In finite-size systems with open boundaries, skyrmions can, however, be stable as the boundaries break the sublattice symmetry. We find that skyrmions in finite-sized systems persist even if the temperature is increased up to the Curie temperature. To show this, we investigate a single skyrmion in a small system of size $L = 8$ with open boundaries at $D/J = 1$, $B/J = 4$ and $K = 0$, deep in the $2q$ phase (see inset of Fig. 2.4(a)). The system size is chosen as the maximum size at which at most one skyrmion forms. Starting well above the critical temperature we anneal the system as discussed above. Due to sublattice symmetry, the system gets trapped in a state with either a skyrmion or an antiskyrmion in the center. From the susceptibility $\chi_w = \langle w^2 \rangle - \langle w \rangle^2$ of the winding number of the staggered magnetization, which is at a minimum at the critical temperature $\beta_c^{-1} \equiv k_B T_c / J$, we find $\beta_c \approx 3.9$. Results from 10^4 annealings allow for an accurate picture of the expected number of skyrmions in this system at a certain temperature. In particular, we determine the probability density $\rho(w, T)$ for a value w of the winding number at temperature T. Results for χ_w and $\rho(w, T)$ are shown in Fig. 2.4. Within margins of error, the system contains roughly half of the time ($49.54 \pm 1.0\%$) a skyrmion instead of an antiskyrmion, as expected from symmetry arguments for temperatures below the critical temperature. Notice that the winding number is not exactly an integer due to edge effects. In short, this shows that (anti)skyrmions as stable isolated topological objects can exist in finite-sized systems at temperatures below the Curie temperature. Moreover, the finite size turns out to stabilize skyrmionic structures well outside the parameter range where the $2q$ phase is stable[2].

---

[2] We thank A. Roldán-Molina and A. S. Núñez for correspondence about this point.

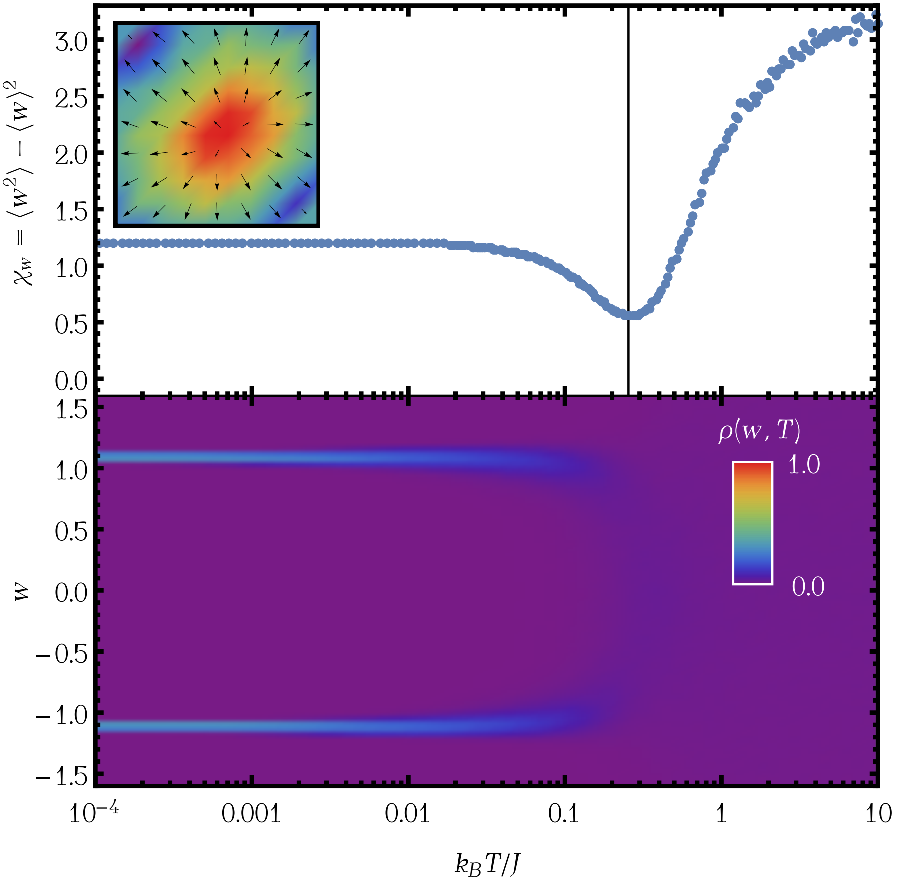

Figure 2.4. Upper panel: susceptibility of the winding number of the staggered magnetization χ_w as a function of temperature $k_B T/J$, for a system of size $L = 8$ with couplings $D/J = 1$, $B/J = 4$ and $K = 0$. These parameters are chosen such that a single skyrmion emerges (see inset). The arrows represent the local Néel vector in the xy-plane and the background colour shows the z-component as positive (red) or negative (purple). A vertical line is drawn at the temperature $k_B T/J \approx 0.25$ at which point the susceptibility is minimal. Lower panel: probability density $\rho(w, T)$ of the winding number w of the staggered magnetization as a function of temperature. Below $k_B T/J \approx 0.25$, indicated by a vertical line, the system chooses a configuration with either a skyrmion or an antiskyrmion.

8 Discussion and conclusion

In summary we have shown that certain types of antiferromagnetic thin films have four phases at zero temperature including a $2q$ phase which was not reported before. With Monte Carlo simulations and Fourier analysis, we constructed a phase diagram. The $2q$ phase has close relations to skyrmions in ferromagnetic systems, but due to symmetries a lattice of topologically isolated objects is not expected. We have shown however, that in finite-sized systems and at nonzero temperatures (anti-)skyrmions can be thermodynamically stable configurations. The existence of thermodynamically stable skyrmions in SLAs provides an appealing alternative over skyrmions in ferromagnets as data carriers.

To address finite-size effects and effects of periodic boundaries, we verified that for smaller systems of size $L = 16$ the phase diagram is not significantly different. At very low B and D finite-size effects are stronger as long-wave-length modulated states do not fit into the small systems anymore. For parameters yielding the $2q$ phase, we verified that the conclusions presented above, which were obtained for systems of size $L = 32$, still hold if the system size is increased to $L = 128$. We also verified that helical boundaries with a shift up to half a period of the $2q$ phase only result in a rotation of the q-vector but otherwise do not affect the phase diagram.

Since stabilizing the $2q$ phase requires large fields $B \sim J$, the best candidates for experimental verification are antiferromagnets with low critical temperature $T_c \sim J/k_B$ so that the required fields can be more easily achieved. A possibility for experimental observation would be a monolayer of an antiferromagnetic compound that is probed by a scanning tunneling microscope, similar to the experiments with Fe [66] in which temperature and fields have similar energy scales.

In future work we intend to study quantum fluctuations of the ground states in the phase diagram, and how the antiferromagnetic textures interact with spin and heat current.

3 Finite-size scaling at infinite-order phase transitions

For systems with infinite-order phase transitions, in which an order parameter smoothly becomes nonzero, a new observable for finite-size scaling analysis is suggested. By construction this new observable has the favourable property of diverging at the critical point. Focussing on the example of the F model we compare the analysis of this observable with that of another observable, which is also derived from the order parameter but does not diverge, as well as that of the associated susceptibility. We discuss the difficulties that arise in the finite-size scaling analysis of such systems. In particular we show that one may reach incorrect conclusions from large-system size extrapolations of observables that are not known to diverge at the critical point. Our work suggests that one should base finite-size scaling analyses for infinite-order phase transitions only on observables that are guaranteed to diverge.[1]

1 Introduction

The study of phase transitions is a central topic in physics. In statistical physics these drastic changes in the physical properties of a system show up in non-analytic behaviour of quantities such as the free energy f per volume. For finite-order phase transitions (FOPTs) this takes the form of non-smoothness, where some derivative of f makes a jump at the critical temperature. Such discontinuous functions provide suitable observables for numerical investigation into universal as well as model-specific properties of the phase transition. In this setting finite-size scaling (FSS) is a powerful tool to quantitatively extrapolate the power-law behaviour of observables near criticality [13, 21].

---

[1] The contents of this chapter are largely based on the work of R. Keesman, J. Lamers, R. A. Duine, and G. T. Barkema [3]. This work has come to fruition due to collaboration with J. Lamers. His focus was on everything mathematical and analytical whereas mine was on the simulation and finite-size scaling. Special thanks go out to H. van Beijeren, H. Blöte, and H. Stoof for insightful discussions.

For infinite-order phase transitions (IOPTs) the situation is more subtle since the transition is not as abrupt as for FOPTs. In the prototypical example, the XY-model in two dimensions, the critical—or perhaps more appropriately 'transition'—temperature marks the point at which free vortices start to dominate the physics, even though the susceptibility, which characterizes the single-vortex fluctuations, has a peak away from this temperature [92]. From a more mathematical perspective the non-analyticity marking IOPTs is rather weak: the free energy depends smoothly on the temperature, where f and all its derivatives are continuous, but it has an essential singularity at the critical temperature. (Recall that, unlike in the complex case, there are smooth functions that are not real-analytic; a standard example is the function given by $\exp(-1/x)$ for $x > 0$ and zero elsewhere.) In addition IOPTs often exhibit logarithmic finite-size corrections [93, 94, 95]; although this does not make FSS impossible [96, 97] it has been shown to give rise to difficulties [98], and rather large systems must be investigated to accurately analyse the scaling. Accordingly, various other numerical methods for studying IOPTs have also been developed [99, 100, 101].

In such a more delicate setting one has to take care to select appropriate observables for numerical analysis using FSS. Order parameters do not directly allow one to locate the critical point for IOPTs since the numerical determination of the point at which a function smoothly becomes nonzero is a futile task. For this reason observables that diverge at the critical point, e.g. susceptibilities for second-order phase transitions, are more suitable for studying a model's behaviour near criticality [98, 102, 103]. One should also keep in mind that for IOPTs there are also observables, such as the specific heat, that do not diverge for increasing system size; they peak away from the critical temperature and do not tend to a Dirac delta function in the thermodynamic limit of infinite system size [94]. In this work we propose a new observable that, by construction, peaks at the critical temperature in the thermodynamic limit for any model with an IOPT that is characterized by a smooth order parameter.

Specifically we consider the F model, which is an interesting test case since it was solved analytically on a square lattice with periodic boundaries in the thermodynamic limit [33, 104]. At the same time it is related to the XY-model via a series of dualities involving the discrete Gaussian solid-on-solid model and the Coulomb gas [33, 105, 106, 107]. Our new observable is essentially the logarithmic derivative of the spontaneous staggered polarization P_0, for which an asymptotic analytical expression is known for all temperatures [108]. We use a FSS analysis to compare the new observable with the ordinary derivative of P_0 and the susceptibility associated with P_0. These observables behave quite differently: the logarithmic derivative nicely diverges at the critical point in the thermodynamic limit, the ordinary derivative has a bounded peak elsewhere for all system sizes, and for the susceptibility—which is commonly used to analyse critical behaviour—the scaling near criticality in the thermodynamic limit has been conjectured [109]. In our estimates of characteristics such as the critical temperature, however, identical analyses of these observables lead to similar asymptotic results. This once more illustrates that one should be careful in numerical analyses of IOPTs. In particular, our work thus suggests that one should base FSS analyses for IOPTs only on observables that are guaranteed to diverge.

This paper is organised as follows. In Section 3.2 we recall the basics of the F model and discuss the relevant observables and their known asymptotic expression. The Monte Carlo cluster algorithm and data processing are treated in Section 3.3. The analysis of the three observables is performed in Section 3.4, and the results are discussed in Section 3.5. We end with a conclusion in Section 3.6.

2 The F model and observables

The six-vertex model, or ice-type model, is a lattice model for which each vertex is connected to four others by edges carrying an arrow pointing in or out of the vertex, such that precisely two arrows point towards each vertex. Thus there are six allowed configurations around each vertex as shown in Fig. 3.1. To each such vertex configuration i one assigns a (local) Boltzmann weight $\exp(-\beta\,\epsilon_i)$, where $\beta := 1/(k_\mathrm{B}T)$ is the inverse temperature and ϵ_i the energy of that configuration. The (global) Boltzmann weight of the entire configuration is the product of the local weights of all vertex configurations. The F model [110] is given by the particular choice $\epsilon_1 = \epsilon_2 = \epsilon_3 = \epsilon_4 = \epsilon > 0$ and $\epsilon_5 = \epsilon_6 = 0$. This is the prototype of the antiferroelectric regime of the six-vertex model, where vertex configurations 5 and 6 are energetically favourable. At sufficiently low temperatures the system orders in an antiferroelectric fashion, with vertices 5 and 6 alternating in a chequerboard-like fashion. From now on we consider the F model on a square $L \times L$ lattice with periodic boundary conditions in both directions, and set $k_\mathrm{B} = \epsilon = 1$.

The free energy (per site) in the thermodynamic limit was found analytically

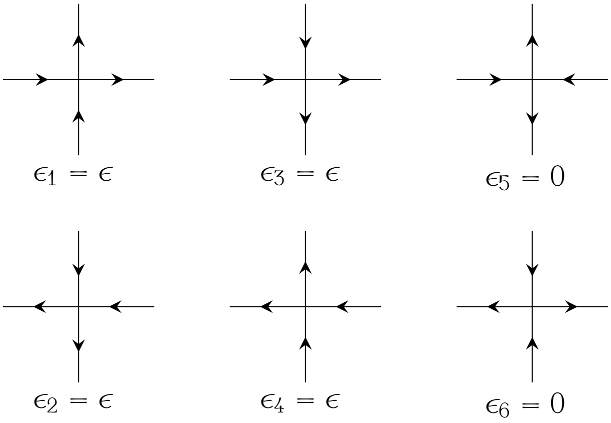

Figure 3.1. The six allowed vertices with associated energies for the F model, where $\epsilon > 0$.

for the F model by Lieb [33, 104] using a Bethe-ansatz analysis. There is an IOPT with critical (or 'transition') temperature $\beta_c = \ln 2$, or $\Delta_c = -1$ where $\Delta := 1 - \exp(2\beta)/2$. In the low-temperature regime the free energy can be expressed as a convergent series,

$$\beta f^{\text{ana}}(\lambda) = \beta - \lambda - \sum_{n=1}^{\infty} \frac{\exp(-n\lambda)\sinh(n\lambda)}{n\cosh(n\lambda)} \tag{3.1}$$

where $\lambda := \operatorname{arccosh}(-\Delta) > 0$ parametrizes $\beta > \beta_c$, while at high temperatures one has an integral representation

$$\beta f^{\text{ana}}(\mu) = \beta - \frac{1}{4\mu} \int_0^{\infty} \frac{dt}{\cosh(\pi t/2\mu)} \ln\!\left(\frac{\cosh(t) - \cos(2\mu)}{\cosh(t) - 1} \right) \tag{3.2}$$

for $\mu := \arccos(-\Delta)$, $0 < \mu < \pi/2$, parametrizing $\beta < \beta_c$. The entire high-temperature region can be regarded as critical in the sense that correlations decay as inverse power laws rather than exponentially [93].

Although the six-vertex model has not been solved in the presence of an external staggered electric field, Baxter [108] found an exact expression for the spontaneous staggered polarization P_0 per site. To each microstate C one can associate an 'instantaneous' spontaneous staggered polarization $P_0(C)$, which can be computed as the 'staggered' sum of the net polarizations at the vertices, where the direction of the net polarization is flipped at every other site (in a chequerboard-like way). Then the thermal average $P_0 := \langle P_0(C)\rangle$ is an order parameter for the F model, vanishing for $\beta < \beta_c$ and becoming nonzero at the critical temperature. When $\beta > \beta_c$ it is given by

$$P_0^{\text{ana}}(\lambda)^{1/2} = \sqrt{\frac{2\pi}{\lambda}} \sum_{n=1}^{\infty} \exp\biggl(-\frac{(n-1/2)^2\pi^2}{2\lambda}\biggr). \tag{3.3}$$

Like the free energy this function is smooth with an essential singularity at $\beta = \beta_c$, which is very weak: the functions and all their derivatives do tend to zero as β approaches β_c from above. When the F model is reinterpreted as a height model (the body-centred solid-on-solid model) the IOPT is a roughening transition [105].

The observables on which we will focus are the derivatives $\beta^2\,\partial_\beta \ln P_0$ and $\beta^2\,\partial_\beta P_0$, where $\partial_\beta := \partial/\partial\beta$, together with the susceptibility $\chi := \beta\,[\langle P_0(C)^2\rangle - \langle P_0(C)\rangle^2]$ of the staggered polarization, which is called the spontaneous staggered polarizability. Baxter [109] conjectured the following form of the susceptibility in the low-temperature regime

$$\chi(\lambda) \sim \lambda^{-2}\exp(\pi^2/2\lambda)\,. \tag{3.4}$$

The preceding discussion ensures that $\beta^2\,\partial_\beta \ln P_0$ diverges at the critical temperature whereas $\beta^2\,\partial_\beta P_0$ has a (finite) peak at some $\beta_{\max} > \beta_c$. To the best of our knowledge neither $\beta^2\,\partial_\beta \ln P_0$ nor $\beta^2\,\partial_\beta P_0$ have been considered before in the literature. The latter is included to demonstrate one has to be careful in FSS for IOPT: we show that it is hard to extrapolate numerical data to the thermodynamic limit, even when the exact limiting expressions are known.

3 Simulations

Our Monte Carlo simulations are based on a cluster algorithm that uses the (one-to-three) mapping from the six-vertex model to a three-colouring of the square lattice [33, Note added in proof]. Choose three colours, ordered in some way, and use one of them to colour any single plaquette (face) of the lattice. Then any configuration of the six-vertex model uniquely determines a three-colouring, where the direction of the arrow on an edge dictates whether the colour increases or decreases (modulo three), and the ice rule ensures that the colouring is well defined. For the F model vertices surrounded by all three colours (configurations 1 to 4 in Fig. 3.1) are energetically less favourable than those at which only two colours meet (configurations 5 and 6).

The multi-cluster algorithm builds clusters containing adjacent faces of two colours, and patches these clusters together diagonally with a probability that is such that required detailed balance is met. After no more clusters can be included the colours in the clusters are swapped and one cluster update has been performed [13]. Because of the small autocorrelation times at the temperatures near the phase transition, we take measurements after 10 of these cluster updates for system sizes $L < 128$, and after each cluster update for larger systems. At least 10^6 measurements are made per temperature per system, at minimally 15 different temperatures. For the largest system that we consider, with $L = 512$, we simulate at 29 different temperatures with slightly over 8×10^6 measurements performed per temperature.

From expressions (3.1)–(3.2) for the free energy we can estimate the mean and variance in energy measurements for finite systems at a given temperature. Moreover the specific heat $C_v = \beta^2 \partial_\beta^2 (\beta f)$ is bounded and, in leading order, does not scale with L. Together these ensure that the parallel-tempering and multi-histogram methods can be applied successfully.

Parallel tempering is a simulation method in which systems are simulated at various temperatures and periodically swapped [14]. Here the probability of swapping two configurations at different temperatures is given by $P_{\text{swap}} = \min[1, \exp(\delta_\beta\, \delta_E)]$, where $\delta_\beta := \beta_{\text{high}} - \beta_{\text{low}}$ and $\delta_E := E_{\text{high}} - E_{\text{low}}$ are the difference in inverse temperature and energy between the two configurations, respectively. To make sure that P_{swap} is large enough for configurations to move reasonably fast through this temperature landscape we want the histograms of the energies at different temperatures to overlap significantly. Starting from some temperature for which we know the average energy $U := \langle E(C) \rangle$ and the standard deviation σ_U from the analytical expression of the free energy, a neighbouring temperature is chosen such that the difference in energies is roughly σ_U, *viz.*, $\beta' = \beta \pm \beta/\sqrt{C_v}$. After each measurement we may swap the configuration with one at such a neighbouring temperature, with acceptance probability P_{swap} between 47% and 53% for all simulations at large system sizes.

At each measurement we record the energy $E(C)$ and instantaneous spontaneous staggered polarization $P_0(C)$ for various temperatures. Using the multi-histogram method any function of the values $E(C)$ and $P_0(C)$ can then be reliably estimated as a function of temperature [23]. For this method to work the energy histograms must have significant overlap; we have ensured that this is indeed the case for our data. Figure 3.2 shows the result for $\beta^2\,\partial_\beta \ln P_0$, $\beta^2\,\partial_\beta P_0$ and χ, together with their known and conjectured analytical form. Note that the data in the low-temperature regime are in agreement with the analytical forms of $\beta^2\,\partial_\beta \ln P_0$ and $\beta^2\,\partial_\beta P_0$. For χ the data collapse in this regime and support the conjecture (3.4).

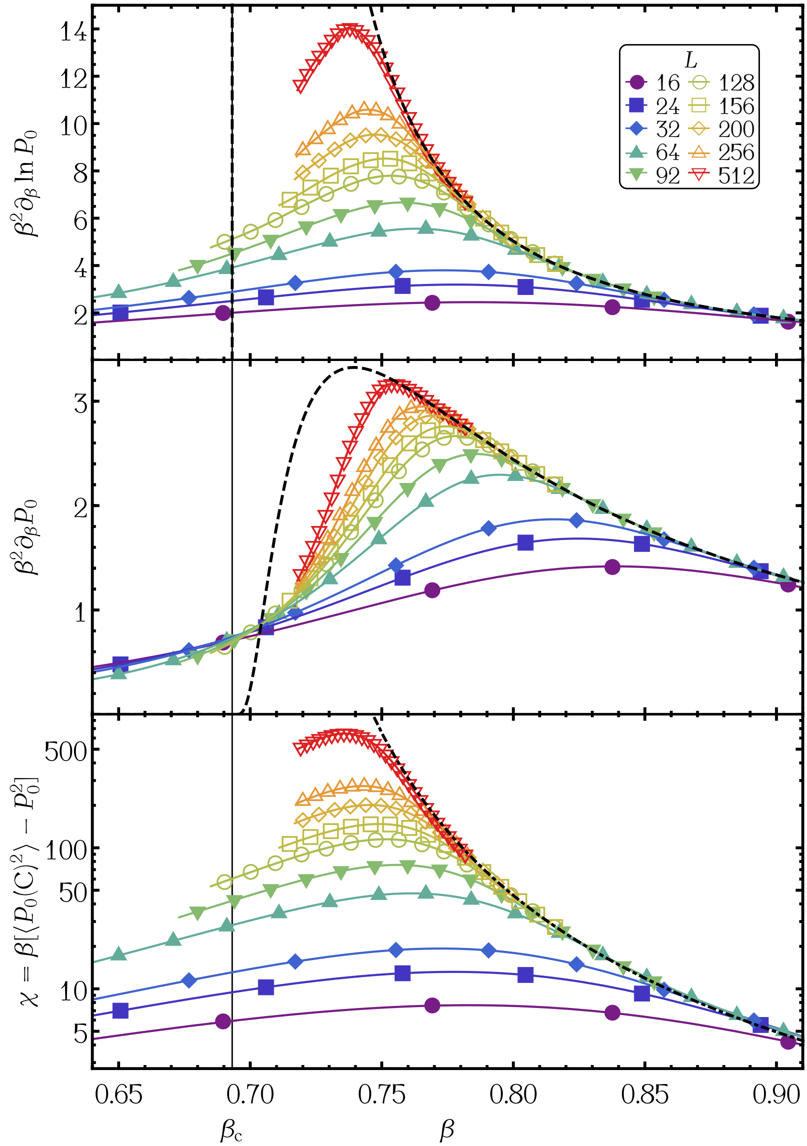

Figure 3.2. The observables $\beta^2\,\partial_\beta \ln P_0$ (upper panel), $\beta^2\,\partial_\beta P_0$ (central panel), and χ (lower panel) versus β for system sizes up to $L = 512$. The data points show the temperatures at which the simulations were run, while the solid lines are the functions extracted from this data using the multi-histogram method. When available the analytical form for infinite systems [cf. Eq. (3.3)] is shown by a dashed black line. For sufficiently low temperatures all graphs collapse onto these dashed black lines, corroborating the validity of our simulations. For $L \to \infty$ we know that $\beta^2\,\partial_\beta \ln P_0$ must diverge at the critical temperature $\beta_c = \ln 2$, indicated by a vertical line, whereas $\beta^2\,\partial_\beta P_0$ is bounded and peaks elsewhere. A fit to the conjectured form of χ, Eq. (3.4), is indicated by a dotted-dashed black line in the lower panel.

4 Analysis

The usual finite-size scaling procedure is to take the data, see Fig. 3.2, and collapse the graphs by scaling the distance to the critical temperature and the height as functions of the system size L. For the F model there are large logarithmic corrections due to 'quasi' long-range correlations [92] as well as higher-order finite-size corrections [103]. The systems size at which the finite-size corrections become negligible do not yet seem to be within reach, so we cannot perform a data collapse based purely on analytical expressions.

Instead we will perform a numerical data collapse. For each of the three observables that we are interested in we determine the coordinates $(\beta_{\max}, h_{\max})$ of the maximum, together with the peak width w. Here we define the width by demanding that the function passes through the point $(\beta_{\max} + w, 0.95\, h_{\max})$. This definition is chosen such that w can be accurately measured for large systems given the simulation data; we focus on lower temperatures (higher β) because of the asymmetry of the observables around the critical temperature. Thus we have three characteristics, which are well defined since any observable is smooth and bounded for finite systems. This allows for a numerical data collapse by shifting $(\beta_{\max}, h_{\max})$ and $(\beta_{\max} + w, 0.95\, h_{\max})$ on top of each other. The result for our three observables is shown in Fig. 3.3. Sufficiently close to the critical point $\beta^2\, \partial_\beta \ln P_0$ and χ scale well, which is a positive sign for scalability to the thermodynamic limit. Note that $\beta^2\, \partial_\beta P_0$, for which we know the (bounded) asymptotic solution, does not exhibit scalability for the system sizes that we investigate. We extrapolate the characteristics $(\beta_{\max}, h_{\max})$ and w, extracted from the data for various system sizes, to the thermodynamic limit.

4.1 Peak position $\beta_{\max}$

The analytic expression in Eq. (3.3) reveals that $\beta^2\, \partial_\beta \ln P_0$ must develop a Dirac delta-like peak at $\beta_c \approx 0.6931$ as $L \to \infty$. Instead, the peak of $\beta^2\, \partial_\beta P_0$ remains finite and shifts to $\beta_{\max}^{\text{ana}} \approx 0.7394$. The large-$L$ behaviour of the spontaneous staggered polarizability χ is not analytically known. The form of the leading finite-size corrections can be obtained by expanding the inverse temperature in L as [103]

$$\beta_{\max}(L) = \beta_c + \frac{A_\beta}{\ln^2 L} + \frac{B_\beta}{\ln^3 L} + \frac{C_\beta}{\ln^4 L}\,. \tag{3.5}$$

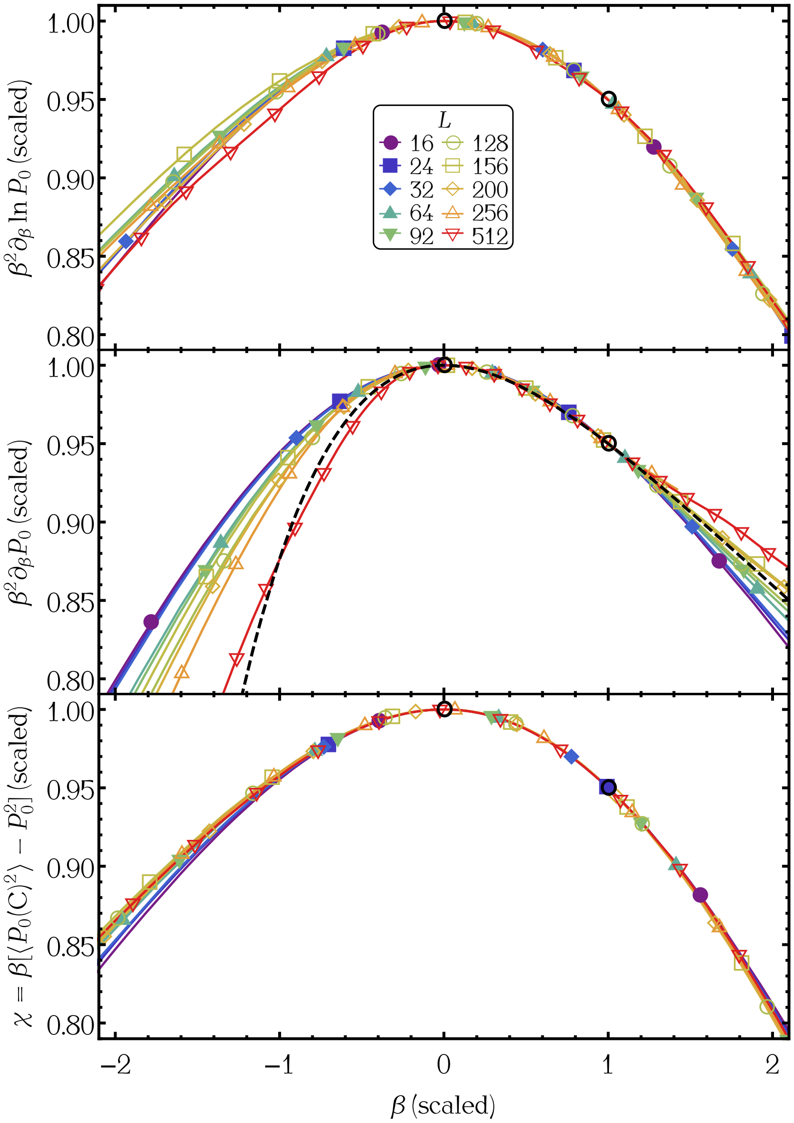

Figure 3.3. The three observables scaled such that for each system size $(\beta_{\max}, h_{\max}) \mapsto (0, 1)$ and $w \mapsto 1$. This scaling works well in the low-temperature regime for $\beta^2\,\partial_\beta \ln P_0$ (upper panel) and χ (lower panel). For $\beta^2\,\partial_\beta P_0$ (central panel) it seems to fail, cf. the deviation from the asymptotic analytical result indicated by a dashed black line.

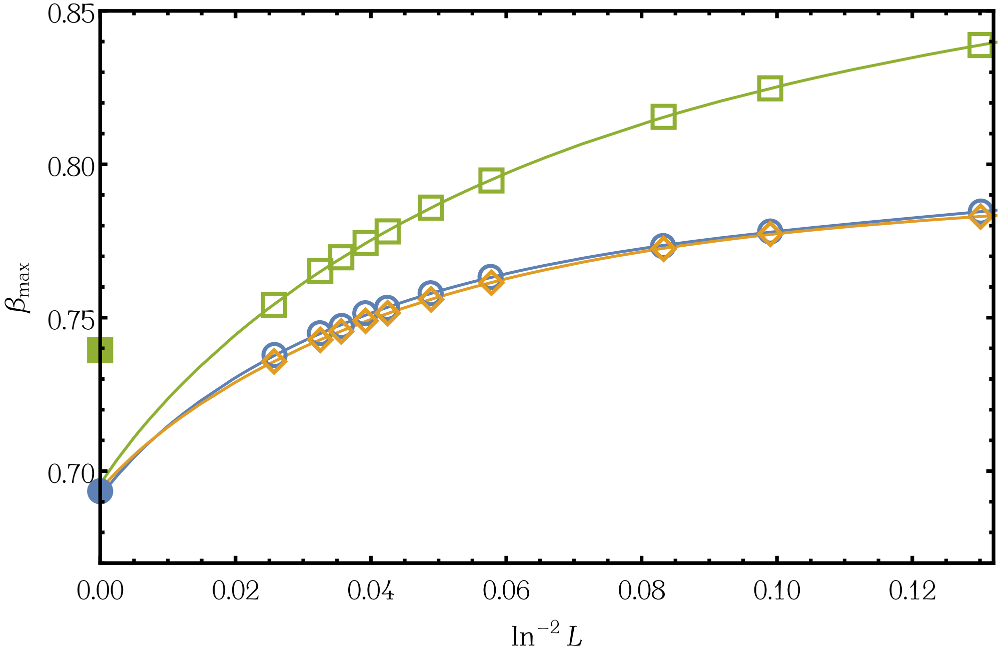

Figure 3.4. The inverse temperatures at which $\beta^2\,\partial_\beta \ln P_0$ (blue circles), $\beta^2\,\partial_\beta P_0$ (green squares), and χ (yellow diamonds) are maximal, here shown as functions of the system size. The asymptotic solutions, $\beta_{\mathrm{c}} = \ln 2$ for $\beta^2\,\partial_\beta \ln P_0$ and $\beta^{\mathrm{ana}}_{\max} \approx 0.7394$ for $\beta^2\,\partial_\beta P_0$, are shown at $\ln^{-2} L = 0$. Best fits of the form Eq. (3.5) to the data are shown as solid lines, and all seem to converge to β_{c}.

Figure 3.4 displays our results for $\beta_{\max}$ as a function of L as obtained from our three observables, together with the analytic asymptotic values, and the best fits to Eq. (3.5). These fits yield $\beta^{\mathrm{fit}}_{\max} = 0.6914(28)$ for $\beta^2\,\partial_\beta \ln P_0$, $\beta^{\mathrm{fit}}_{\max} = 0.6955(17)$ for $\beta^2\,\partial_\beta P_0$, and $\beta^{\mathrm{fit}}_{\max} = 0.6937(11)$ for χ.

4.II Peak height $h_{\max}$

Since we know from the asymptotic formula for P_0 that $\beta^2\,\partial_\beta \ln P_0$ diverges as $L \to \infty$ let us consider inverse heights. The inverse peak height of $\beta^2\,\partial_\beta P_0$ tends to $(h^{\mathrm{ana}}_{\max})^{-1} \approx 0.3009$. If a naive linear fit is applied to h^{-1} as a function of $\ln^{-2} L$ the extrapolation yields $(h^{\mathrm{fit}}_{\max})^{-1} \approx -0.0095(16)$ for $\beta^2\,\partial_\beta \ln P_0$ and $(h^{\mathrm{fit}}_{\max})^{-1} \approx 0.2161(17)$ for $\beta^2\,\partial_\beta P_0$. Adding finite-size corrections to the

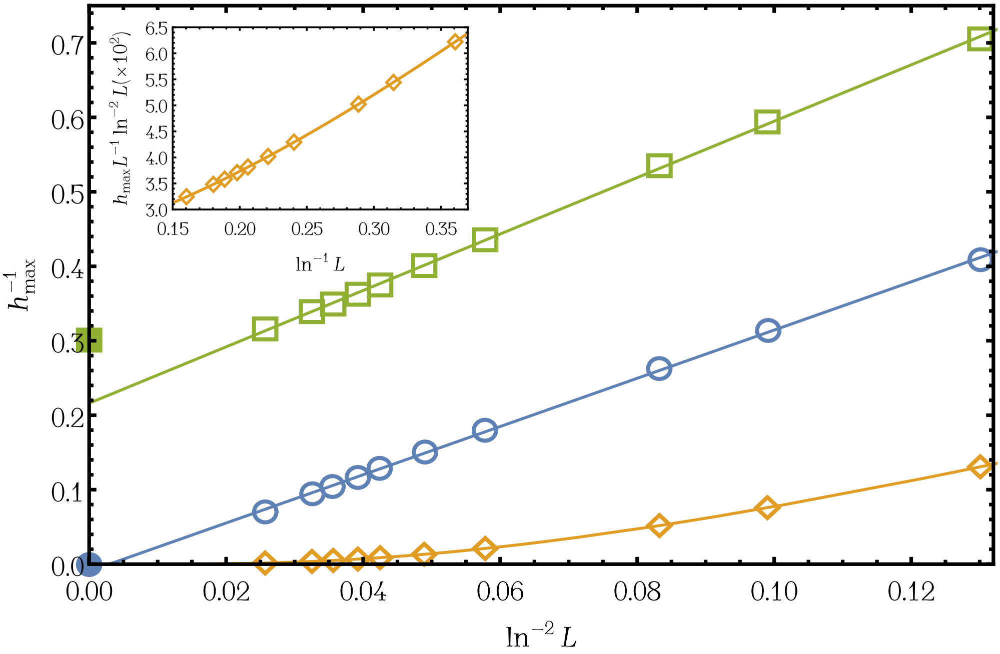

Figure 3.5. The inverse maximal heights of $\beta^2 \, \partial_\beta \ln P_0$ (blue circles), $\beta^2 \, \partial_\beta P_0$ (green squares) and χ (yellow diamonds) as functions of $\ln^{-2} L$. The inset shows the peak height of χ with differently scaled axes. The asymptotic values, $(h_{\max}^{\text{ana}})^{-1} = 0$ for $\beta^2 \, \partial_\beta \ln P_0$ and $(h_{\max}^{\text{ana}})^{-1} \approx 0.3009$, are included at $\ln^{-2} L = 0$. Data indeed suggests that $\beta^2 \, \partial_\beta \ln P_0$ and χ diverge while $\beta^2 \, \partial_\beta P_0$ stays finite. Best linear fits as functions of $\ln^{-2} L$ are shown as solid blue and green lines for $\beta^2 \, \partial_\beta \ln P_0$ and $\beta^2 \, \partial_\beta P_0$, respectively, while the best fit for χ as in Eq. (3.6) is displayed in yellow.

conjectured form of χ in Eq. (3.4) gives [103]

$$h_{\max}(L) = A_\chi \, L \ln^2 L \left(\frac{B_\chi}{\ln L} + \frac{C_\chi}{\ln^2 L} + \frac{D_\chi}{\ln^3 L} \right) \tag{3.6}$$

for the maximum of the susceptibility. The peak heights of the three observables and corresponding best fits are shown as function of system size in Fig. 3.5.

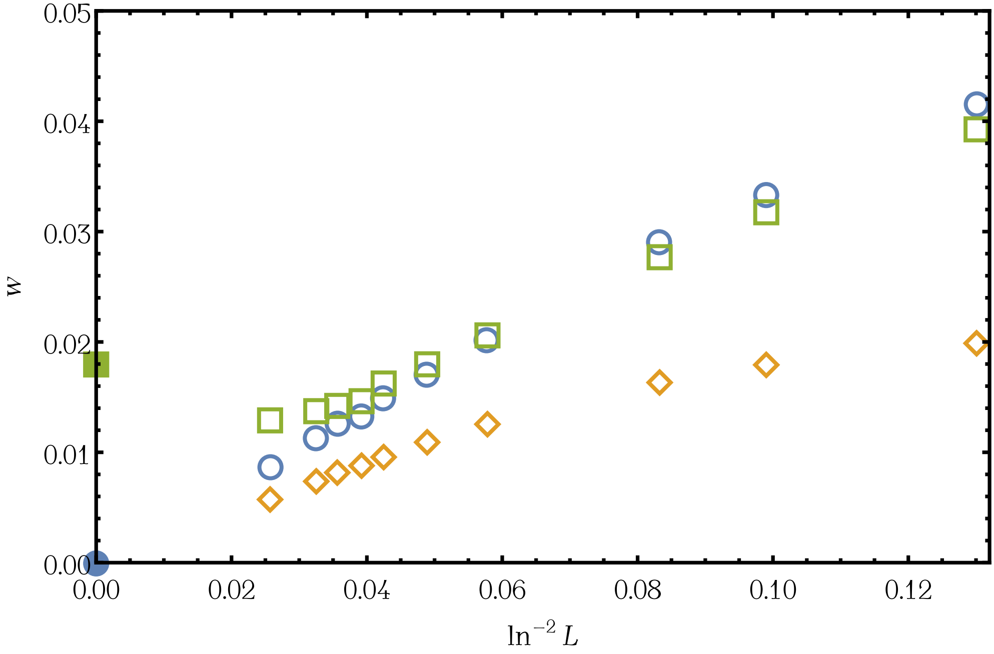

Figure 3.6. The width, defined as the distance between the peak and the (lower-temperature) position at which the curve reaches 95% of the maximal height, shown for $\beta^2\,\partial_\beta \ln P_0$ (blue circles), $\beta^2\,\partial_\beta P_0$ (green squares), and χ (yellow diamonds) at various system sizes. The asymptotic values, $w^{\text{ana}} = 0$ for $\beta^2\,\partial_\beta \ln P_0$ and $w^{\text{ana}} \approx 0.0180$ for $\beta^2\,\partial_\beta P_0$, are indicated at $\ln^{-2} L = 0$. Note that in the observed regime all observables decrease monotonically with L, yet $\beta^2\,\partial_\beta P_0$ must increase at some point to reach its asymptotic value.

4.III Peak width w

From the asymptotic expression we know that $w^{\text{ana}} = 0$ for $\beta^2\,\partial_\beta \ln P_0$ and $w^{\text{ana}} \approx 0.0180$ for $\beta^2\,\partial_\beta P_0$ in the thermodynamic limit. Our data, together with these analytic values, are shown in Fig. 3.6. Since the analytic form of the scaling behaviour for w is lacking no best fit is performed.

5 Comparison of observables

Using our results we can compare the performance of our new observable for the F model, $\beta^2\,\partial_\beta \ln P_0$, with that of $\beta^2\,\partial_\beta P_0$ and that of χ. Asymptotic

		$\beta^2\,\partial_\beta \ln P_0$	$\beta^2\,\partial_\beta P_0$	χ
$\beta_{\max}$	ana	$\ln 2 \approx 0.6931$	0.7394	$\ln 2$ (conj)
	fit	0.6914(28)	0.6955(17)	0.6937(11)
$h_{\max}^{-1}$	ana	0	0.3009	0 (conj)
	fit	−0.0095(16)	0.2161(17)	0
w	ana	0	0.0180	0 (conj)
	fit	—	—	—

Table 3.1. All analytically known and conjectured asymptotic values of our characteristics, together with our numerically extrapolated best values, are shown for our three observables.

analytical and numerically extrapolated values for the three characteristics of these observables are collected in Table 3.1 if available.

5.I Logarithmic derivative of P_0

Our claim is that for an IOPT the logarithmic derivative of the order parameter is a suitable observable for numerical analysis: it must, by construction, tend to a Dirac delta-like distribution at the critical point in the thermodynamic limit. The extrapolated characteristics $\beta_{\mathrm{c}}^{\mathrm{fit}}$ and $h_{\max}^{\mathrm{fit}} = -0.0095(16)$ for $\beta^2\,\partial_\beta \ln P_0$ are in agreement with this claim. Note that a linear fit for the inverse peak height as a function of $\ln^{-2} L$ yields a negative asymptotic result, albeit close to zero, which indicate that there must be other leading finite-size corrections that become important for system sizes outside the reach of the simulations performed here.

5.II Ordinary derivative of P_0

It is instructive to compare our new observable with a similar observable that, by construction, should not be suitable for numerical analysis. Interestingly, when the temperature at which $\beta^2\,\partial_\beta P_0$ peaks is extrapolated in a similar fashion as for the logarithmic derivative the results are comparable. By construction, however, we know that $\beta_{\max}$ must go to a much higher value in the thermodynamic limit; there must be an inflection point outside the range of simulated system sizes. Similarly, a linear extrapolation for the inverse peak height matches with the data, yet is far from the known asymptotic expression. Concerning the peak width one notes that the observed peaks for $L \geq 128$ are less wide than the peak of the asymptotic expression, cf. the central panel in Fig. 3.2; thus w must start to increase at some larger system size, even though it decreases monotonically in the simulated regime.

5.III Polarizability

Finally we turn to χ. Recall that this quantity is not known analytically but there is a conjecture, Eq. (3.6), for its scaling behaviour. The observed $\beta_{\max}$ for χ are very close to those of $\beta^2\,\partial_\beta \ln P_0$ (cf. Fig. 3.4), and the extrapolated value $\beta_{\max}^{\text{fit}} = 0.6937(11)$ is in agreement with $\beta_c = \ln 2$. Together with the steadily decreasing width for growing system sizes the data suggests that χ also tends to a Dirac delta-like distribution. Our data fits well with the conjectured form if higher-order finite-size corrections are taken into account, although it must be noted that many alternative forms are also consistent with the data for systems of sizes investigated here.

6 Conclusion

In this work we looked at infinite-order phase transitions (IOPTs), with the case of the F model as a guiding example. We have suggested a new observable that can be used for finite-size scaling analyses. For any system exhibiting an IOPT with a smooth order parameter this observable is basically the logarithmic derivative of the order parameter, which by construction diverges in the thermodynamic limit. For the F model this is $\beta^2\,\partial_\beta \ln P_0$, where P_0 is the spontaneous staggered polarization. Since the exact asymptotic form of P_0 is known in the thermodynamic limit the F model is a good test case to study the performance of our new observable in a finite-size scaling analysis.

For comparison we also have analysed two other observables. The first is $\beta^2\,\partial_\beta P_0$, which we know to be bounded with peak away from the critical point for all system sizes. Although it must therefore behave quite differently when $L \to \infty$, its observed characteristics turned out to be rather similar to that of $\beta^2\,\partial_\beta \ln P_0$ at the system sizes investigated. This illustrates that seemingly reasonable yet incorrect conclusions, cf. the extrapolation to the critical point in Fig. 3.4, may be reached for an IOPT when no analytical expressions are available. The logarithmic corrections and large finite-size corrections for the

F model require utmost caution in finite-size analysis; in particular one has to take care to select appropriate observables in order to make hard claims by means of extrapolation to the thermodynamic limit. Given the similarities in FSS of different observables our work thus suggests choosing an observable that is guaranteed to diverge at the critical point. In this way we ensure that the FSS analysis is formally correct, although system sizes large enough to reveal all leading-order corrections will likely be hard to reach.

The final observable that we have investigated is the (spontaneous staggered) susceptibility $\chi = \beta\,[\langle P_0(C)^2\rangle - \langle P_0(C)\rangle^2]$, which is widely used to analyse phase transitions. The observed characteristics show striking similarities with those of $\beta^2\,\partial_\beta \ln P_0$ and suggests that χ also diverges in the thermodynamic limit. The data are compatible with Baxter's conjecture for χ's scaling behaviour near criticality

Due to the ice rule the F-model is sensitive to the choice of boundary conditions [111, 112]. Certain choices for fixed boundary conditions have already been subjected to some numerical investigations [113, 114, 115]. In the near future we intend to analyse the influence of boundary conditions using finite-size scaling. More generally it would be interesting to test our observable for other models with an IOPT such as the XY-model.

4 Numerical study of the F model with domain-wall boundaries

We perform a numerical study of the F model with domain-wall boundary conditions. Various exact results are known for this particular case of the six-vertex model, including closed expressions for the partition function for any system size as well as its asymptotics and leading finite-size corrections. To complement this picture we use a full lattice multi-cluster algorithm to study equilibrium properties of this model for systems of moderate size, up to $L = 512$. We compare the energy to its exactly known large-L asymptotics. We investigate the model's infinite-order phase transition by means of finite-size scaling for an observable derived from the staggered polarization in order to test the method put forward in our recent joint work with Duine and Barkema. In addition we analyse local properties of the model. Our data are perfectly consistent with analytical expressions for the arctic curves. We investigate the structure inside the temperate region of the lattice, confirming the oscillations in vertex densities that were first observed by Syljuåsen and Zvonarev, and recently studied by Lyberg *et al.* We point out '(anti)ferroelectric' oscillations close to the corresponding frozen regions as well as 'higher-order' oscillations forming an intricate pattern with saddle-point-like features.[1]

1 Introduction

The F model for antiferroelectric materials [110] is a special case of the six-vertex, or ice-type, model that exhibits an infinite-order phase transition

---

[1] The contents of this chapter are largely based on the work of R. Keesman and J. Lamers[4]. J. Lamers contributions, besides extensive knowledge of relevant literature on the topic, is the translation of general mathematical work into our physics framework as well as working out the exact solution of the partition function for finite-sized systems including the staggered polarization field in Section 4.2. R. Keesman has performed the simulations and analyses in Sections 4.3 and 4.4. We thank P. Zinn-Justin for bringing CFTP under our attention, G. Barkema and F. Colomo for feedback on earlier versions of this work, P. Bleher for correspondence, and C. Hagendorf, I. Lyberg, and K. Johansson for useful discussions.

(IOPT) [104]. Amongst others, studying the F model may thus be instructive to get a better grasp of the well-known IOPT of the two-dimensional XY-model as it offers a more simple setting in which the microscopic degrees of freedom are discrete. By definition, at an IOPT the physics of a system does not change as abruptly as it does for finite-order phase transitions, which makes numerical investigations a rather subtle issue. In Ref. [3], together with Duine and Barkema, we proposed a new observable for numerical studies of IOPTs: the logarithmic derivative of the (smooth but not analytic) order parameter for the IOPT. By construction this quantity exhibits a peak at the critical — or rather 'transition' — temperature β_c of the model, which makes it a suitable candidate for the analysis of the physics near the IOPT. We used a finite-size scaling analysis to compare the performance of our observable with that of other observables commonly used in the literature, focussing on the F model with periodic boundary conditions (PBCs) in both directions. In the present work we test the observable in a different, yet closely related, setting. At the same time this allows us to investigate other intriguing features of the F model, such as the dependence of its thermodynamics, i.e. the behaviour at asymptotically large system size, on the boundary conditions.

The microscopic degrees of freedom of the six-vertex model are arrows pointing in either direction along the edges of a square lattice. Around each vertex the arrows have to obey the so-called ice rule, which turns out to be rather restrictive[2]. On the one hand this condition famously allows for a Bethe-ansatz analysis that provides *exact* results (see, e.g., Ref. [117] and references therein) in the thermodynamic limit. On the other hand it causes the model's thermodynamics to depend on the *choice of boundary conditions* used at the intermediate analysis for finite size [111, 112, 116]. (In fact, this phenomenon in the context of graphene [118] originally motivated Ref. [3] and the present work.) PBCs are commonly employed and are compatible with the translational invariance that is present for infinite systems. For the six-vertex model this choice is important for the Bethe ansatz; cf. Ref. [104]. This choice was also used in our previous work [3]. The same thermodynamic behaviour is obtained for 'free' and (conjecturally) 'Néel' boundary conditions, where the arrows on the external edges are respectively left free or fixed to alternate [115, 116]. This is not true for 'ferroelectric' boundary conditions, where the arrows at the boundary all point, e.g., up or to the right, but with a single allowed microstate the resulting thermodynamics is trivial.

---

[2] To see that the ice rule is crucial here consider the eight-vertex model, where the ice rule is slightly relaxed. This model cannot be tackled with a straightforward Bethe-ansatz analysis, and its thermodynamics are insensitive to the choice of boundary conditions; cf. Ref. [116] below.

An interesting intermediate case is provided by *domain-wall boundary conditions* (DWBCs), where on two opposite boundaries the arrows all point outwards whereas on the other two boundaries all arrows point inwards. Such boundary conditions first appeared in the calculation of norms of Bethe vectors in the quantum inverse-scattering method (QISM) in the work of Korepin [119]. Indeed, the QISM allows for an algebraic construction of the Bethe-ansatz vectors for the Heisenberg XXX and XXZ spin chains and the six-vertex model with PBCs. These algebraic Bethe-ansatz vectors simultaneously diagonalize the spin-chain Hamiltonian and the transfer matrix of the six-vertex model provided the parameters featuring in the ansatz obey constraints known as the Bethe-ansatz equations; see, e.g., Ref. [117]. The partition function of the six-vertex model with DWBCs, also known as the *domain-wall partition function*, is related to the norm of the algebraic Bethe-ansatz vectors [119]. Later this quantity was found to have applications ranging from the combinatorics of alternating-sign matrices [120, 121] (see also the book [122]) to one-dimensional quantum systems with inhomogeneous initial conditions that are relevant for cold-atom physics [123] to three-point amplitudes in $\mathcal{N} = 4$ super Yang–Mills theory [124, 125].

The domain-wall partition function admits a concise closed expression for all system sizes [126, 127]. From this the infinite-size asymptotics can be found [111, 128], as well as the form of the leading finite-size corrections [129, 130, 131, 132]. The phase diagram of the six-vertex model has the same form for PBCs and DWBCs, but the details are different [93, 111, 128]; for example, even though the F model exhibits an IOPT in both cases, the free energy per site of the F model is larger for DWBCs than for PBCs. In the past decade or so DWBCs have also attracted considerable attention in relation to the arctic-curve phenomenon: they lead to coexisting phases that are spatially separated, with an *arctic curve* separating the 'frozen' (ordered) and 'temperate' spatial regions. This has been investigated from numerical [113, 133, 134, 135] as well as analytic [123, 136, 137, 138, 139, 140, 141, 142] viewpoints.

The remainder of this paper is organized as follows. In Sec. 4.2 we review the F model with DWBCs, its partition function, and the relevant observables; in particular we give a description of the staggered six-vertex model (cf. Ref. [108]) in the framework of the QISM. The Monte Carlo cluster algorithm and data processing are discussed in Sec. 4.3. The results are treated in Sec. 4.4. We fit the exact asymptotic expressions for the energy, giving best estimates for the free parameters in the finite-size corrections, and perform a finite-size scaling analysis to test our observable at the IOPT. Besides these global averaged properties we use our simulations to examine local properties: the coexisting phases, arctic curves, and the structure in the temperate region of the lattice. We conclude with a summary and outlook in Sec. 4.5. In App. 4.A we review the global symmetries of the F model and describe how these can be exploited to sample the full phase space.

2 Theory

2.1 The *F* model and domain walls

The six-vertex model, or (energetic) ice-type model, is a vertex model on a square lattice. The arrows on the edges are restricted by the *ice rule*, which demands that at every vertex two arrows point inwards and two point outwards. This leaves the six allowed vertex configurations shown in Fig. 3.1. To each such vertex configuration i one assigns (local) Boltzmann weight $\exp(-\beta\,\epsilon_i)$, with $\beta := 1/(k_B T)$ the inverse temperature, $k_B > 0$ the Boltzmann constant that we put to unity from here on, and ϵ_i the energy of the vertex configuration. The energy is additive, so the weight of a configuration is the product of these local weights. Summing these over all allowed configurations, subject to some choice of boundary conditions, one obtains the model's partition function.

The F model can be obtained by taking $\epsilon_1 = \epsilon_2 = \epsilon_3 = \epsilon_4$ and $\epsilon_5 = \epsilon_6$ such that the corresponding vertex weights are related by $a = b = \exp(-\beta\,\epsilon)\,c$ for some $\epsilon > 0$, making vertices 5 and 6 energetically favourable. Interestingly, this model has experimental realizations using artificial spin ice [143][3]. The phase diagram is shown in Fig. 4.2. For low enough temperatures the system is in the antiferroelectric (AF) phase. As temperature increases there is a transition to the disordered (D) phase. For PBCs the ground state consists of vertices 5 and 6 alternating in a chequerboard-like manner; this global AF order persists throughout the AF phase and is destroyed upon entering the D phase.

The six-vertex model does not have a thermodynamic limit in the usual sense: the physical properties of macroscopic systems remain sensitive to the choice of boundary conditions. Rather than imposing PBCs we consider an

---

[3] We thank P. Henelius for making us aware of this.

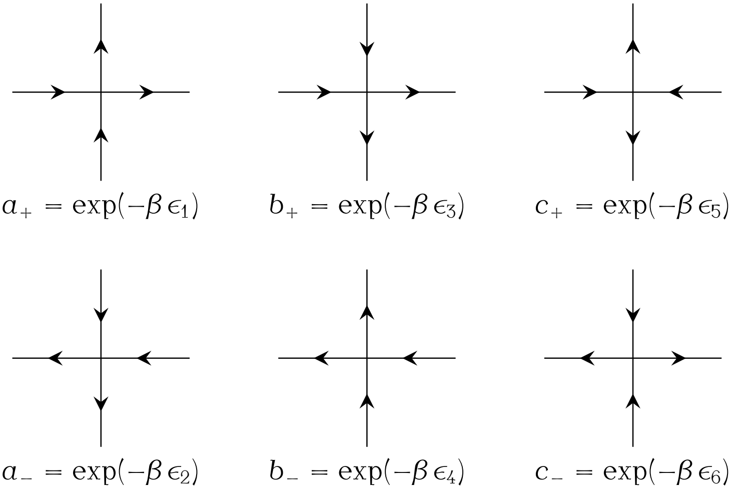
$a_+ = \exp(-\beta\,\epsilon_1)$
$b_+ = \exp(-\beta\,\epsilon_3)$
$c_+ = \exp(-\beta\,\epsilon_5)$
$a_- = \exp(-\beta\,\epsilon_2)$
$b_- = \exp(-\beta\,\epsilon_4)$
$c_- = \exp(-\beta\,\epsilon_6)$

Figure 4.1. The six vertices allowed by the ice rule and their weights for the six-vertex model. Often one assumes arrow-reversal symmetry: $a_\pm = a$, $b_\pm = b$, $c_\pm = c$. The F model is defined by $a = b < c$.

$L \times L$ portion of the lattice with *domain-wall boundary conditions* (DWBCs), where the arrows on external edges are fixed and point out (inwards) on all horizontal (vertical) edges, say. This change in boundary conditions has several interesting consequences that will be reviewed momentarily. Similarly to the case of PBCs (see, e.g., Refs. [93, 144] for reviews) one obtains exact results for the DWBC F model by extending it to the six-vertex model with general vertex weights a, b, and c as in Fig. 3.1. The 'reduced coupling constant' is defined as

$$\Delta := \frac{a^2 + b^2 - c^2}{2\,ab} \; . \tag{4.1}$$

The phase diagram looks again like in Fig. 4.2. At high temperatures the system is in the D phase, $-1 < \Delta < 1$. As the temperature is lowered it transitions into the AF phase, $\Delta < -1$, or one of the two the ferroelectric (FE) phases, $\Delta > 1$, depending on the ratio $a : b : c$. The D–AF phase transition is of infinite order for PBCs [104] as well as DWBCs (cf. the end of the following subsection) [128, 131], while those between the D and FE phases are of first order for PBCs [145] but of second order for DWBCs [111, 146].

In the FE phase the DWBCs are compatible with the FE order, while for $\Delta < 1$ (including the F model) the boundaries raise the free energy per site

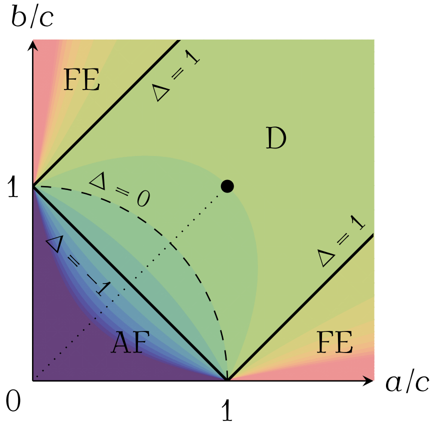

Figure 4.2. The phase diagram of the six-vertex model, parametrized by the ratios a/c and b/c since common rescalings of the vertex weights yield only an overall factor for the partition function. The colours show contours for Δ at steps of 1/2 for $-4 \leq \Delta \leq 4$. The dashed arc is the so-called free-fermion line. The dotted line corresponds to the F model, with an infinite-order phase transition between the antiferroelectric (AF) and disordered (D) phases. The thick dot is the ice point $a = b = c$, which can be interpreted as $\beta = 0$. There are two ferroelectric (FE) phases.

with respect to the case of PBCs. Zinn-Justin [112] suggested that this can be understood as a consequence of coexisting phases that are spatially separated. This phenomenon had also been found for various choices of fixed boundary conditions for the ice model ($a = b = c$) before [147]. Through the ice rule the DWBCs induce ordered regions that extend deep into the bulk, and translational invariance is lost even far away from the boundary. For example, the ground state is no longer a chequerboard-like configuration of vertices 5 and 6 as for PBCs, which would after all lead to alternating arrows along the boundary. Instead the DWBC ground state consists of a central diamond-shaped area with AF order [see also Fig. 4.7(a) below], consisting of vertices 5 and 6 like before, enclosed by corners that each possess FE order, containing a homogeneous configuration of one of the vertices 1 to 4. (When L is even there are two ground-state configurations of this form.) The domain walls thus raise the ground-state energy per site in the thermodynamic limit from 0 for PBCs to $\epsilon/2$ for DWBCs. When the temperature becomes nonzero a disordered region appears that separates the regions of AF and FE order, and above the critical temperature the region with AF order disappears to leave a central disordered region surrounded by FE-ordered regions [113, 133]. There are sharp transitions between the regions, and the curves separating the 'frozen' (AF or FE ordered) and 'temperate' regions in the scaling limit (i.e. let $L \to \infty$ while decreasing the lattice spacing to keep total system size fixed) are known as *arctic curves*. These curves have four contact points with the boundary, which for the F model lie in the middle of each side [140]. For the 'free-fermion point' $\Delta = 0$ the arctic curve is a circle [136] up to fluctuations of order $\sim L^{1/3}$ governed by an Airy process [137, 138]. The arctic curve has also been conjectured for $|\Delta| < 1$ [139, 140] and $\Delta < -1$ [141], where the latter focusses on the curve separating the FE and D regions.

Because we are interested in the F model from now on we focus on the D and AF phases. The following (real) parametrization of the vertex weights are often used in these regimes[4]:

$$\text{D:} \begin{cases} a = \sin(\gamma - t) \\ b = \sin(\gamma + t) \, , \\ c = \sin 2\gamma \end{cases} \qquad \text{AF:} \begin{cases} a = \sinh(\gamma - t) \\ b = \sinh(\gamma + t) \, . \\ c = \sinh 2\gamma \end{cases} \tag{4.2}$$

Here $t \in [-\gamma, \gamma]$ is called the spectral parameter, while $\gamma \geq 0$ is the crossing parameter, which for the D phase is further restricted to $\gamma < \pi/2$; it is related to (4.1) via $\Delta = -\cos 2\gamma$ for D and $\Delta = -\cosh 2\gamma$ for AF. The F model then corresponds to $t = 0$, with $\Delta = 1 - e^{2\beta\epsilon}/2$ or γ encoding the temperature as

$$e^{\beta\epsilon} = \frac{c}{a} = \frac{c}{b} = \begin{cases} 2\cos\gamma \, , & \gamma \in [0, \pi/3] \quad (\text{D}) \, , \\ 2\cosh\gamma \, , & \gamma \geq 0 \quad (\text{AF}) \, . \end{cases} \tag{4.3}$$

The phase transition of the F model occurs at $\beta_c \epsilon = \ln 2$ ($\Delta = -1$, $\gamma = 0$). At this point the parametrization (4.2) vanishes identically, which can be avoided by simultaneously rescaling the weights to set c equal to unity. At the level of the partition function this may be implemented by keeping (4.2) with $t = 0$ but considering the 'renormalized' partition function $c^{-L^2} Z_L(a, b, c) = Z_L(a/c, b/c, 1)$. We will denote this quantity simply by Z_L.

---

[4] Computations using quantum integrability for finite size are often done over $\mathbb{C}$, for which $a = \sinh(u + \eta)$, $b = \sinh u$, $c = \sinh \eta$ is another convenient parametrization. Setting $u = -\gamma - t$ and $\eta = 2\gamma + i\pi$ yields the AF parametrization in (4.2) up to a common sign; including a factor of i in front of γ and t gives that for D up to a common factor of i.

2.II The domain-wall partition function

In some sense the six-vertex model with DWBCs is a theorist's dream. Unlike for PBCs, for which exact results are only available for asymptotically large systems, the domain-wall partition function Z_L can be found exactly for *all* system sizes. In brief the computation goes as follows; see, e.g., Ref. [121] for more details. For the ith row (jth column) of the lattice one introduces a parameter u_i (v_j). This allows one to further extend the model to an inhomogeneous version where the weight (4.2) at position (i,j) features $u_i - v_j$ instead of t. Korepin [119] showed that Z_L, viewed as a function of the u_i, obeys certain properties that determine it uniquely in the inhomogeneous setting; most importantly there is a recursion relation that expresses Z_L with one u_i specialized to a specific value in terms of Z_{L-1}. Izergin [126, 127] found a remarkably concise expression in the form of a determinant of an $L \times L$ matrix. Since it meets all Korepin's requirements, Izergin's determinant provides a formula for the domain-wall partition function valid for all L. Upon carefully evaluating the homogeneous limit, $u_i - v_j \to t$ for all i and j, this results in a Hankel determinant:

$$Z_L = \frac{(ab/c)^{L^2}}{\prod_{k=0}^{L-1}(k!)^2} \det_{L\times L} M \,, \qquad M_{i,j} \coloneqq \partial_t^{i+j-2} \frac{c}{ab} \,, \tag{4.4}$$

where the definition of $M_{i,j}$ assumes a parametrization of the form (4.2). Specializing this quantity to the ice (or 'combinatorial') point $a = b = c$ (so $\Delta = 1/2$) one finds that the number of domain-wall configurations for $L = 1, 2, \dots$ is 1, 2, 7, 42, 429, 7436, 218348, … [121]. For the F model the domain-wall partition function factorizes as $Z_{2L} = 2\, X_{2L} X_{2L+1}$, $Z_{2L+1} = X_{2L+1} X_{2L+2}$ for certain polynomials X_L [121, Thm. 3]; cf. Ref. [148, Thm. 4].

Using the explicit results found by Korepin–Izergin the bulk free energy was evaluated in the thermodynamic limit by Korepin and Zinn-Justin [111] and Zinn-Justin [128]. Prior to that only some special cases in the D phase were known: the free-fermion point ($\Delta = 0$, $\gamma = \pi/4$) corresponding to the 2-enumeration of alternating-sign matrices [120, Sec. 6], and the ice point ($\Delta = 1/2$, $\gamma = \pi/3$) as well as the point $\Delta = -1/2$ ($\gamma = \pi/6$) related to the 3-enumeration of alternating-sign matrices [121]. Here we recall that the 'c^2-enumeration of alternating-sign matrices' (cf., e.g., Refs. [121, 122]), is given by $c^L Z_L(1,1,c)$ since the DWBCs imply that $\#c_- = L + \#c_+$.

A rigorous and more detailed analysis for the D and AF phases and the corresponding transition, which is most relevant for us, was given by Bleher *et al.* [129, 130, 131, 132]. The asymptotic expressions for the domain-wall partition function Z_L, together with the first subleading terms in system size, are as follows for the F model. In the disordered regime one has [129]

$$Z_{\mathrm{D}}^{\mathrm{asym}} = C_{\mathrm{D}}(\gamma)\, f_{\mathrm{D}}(\gamma)^{L^2} L^{\kappa(\gamma)} \left[1 + O(L^{-\alpha})\right] , \tag{4.5}$$

where $C_{\mathrm{D}}(\gamma) > 0$ and $\alpha > 0$ are unknown, while

$$f_{\mathrm{D}}(\gamma) = \frac{\pi \tan \gamma}{4\gamma} , \qquad \kappa(\gamma) = \frac{1}{12} - \frac{2\gamma^2}{3\pi(\pi - 2\gamma)} . \tag{4.6}$$

For the antiferroelectric regime one finds [130]

$$Z_{\mathrm{AF}}^{\mathrm{asym}} = C_{\mathrm{AF}}(\gamma)\, f_{\mathrm{AF}}(\gamma)^{L^2} \vartheta_4(L\pi/2) \left[1 + O(L^{-1})\right] , \tag{4.7}$$

with $C_{\mathrm{AF}}(\gamma) > 0$ another unknown normalization factor, and the extensive part of the free energy is

$$f_{\mathrm{AF}}(\gamma) = \frac{\pi \tanh \gamma}{4\gamma} \, \frac{\vartheta_1'(0)}{\vartheta_1(\pi/2)} , \tag{4.8}$$

where ϑ_1 and ϑ_4 denote the Jacobi theta functions with temperature-dependent elliptic nome $q := \exp(-\pi^2/2\gamma)$.

From these exact asymptotics of the domain-wall partition function it can be shown that, as for PBCs, the phase transition is of infinite order [128, 131]. Indeed, when subtracting the regular part, $(\pi/4\gamma) \tanh \gamma$ [differing from (4.6) only in the parametrization used], from the AF free energy (4.8) one is left with an expression that is smooth but exhibits an essential singularity as $\gamma \to 0^+$.

2.III The staggered polarization

An order parameter for the D–AF phase transition is defined as follows. For any microstate C one can compute the spontaneous staggered polarization $P_0(C)$. This quantity is a measure of the likeness of C to one of the two AF ground states C' of the system with PBCs. At each vertex the local spontaneous staggered polarization can be defined as $\sum_i \sigma_i \sigma_i'/4$, where the sum is taken over the four edges surrounding the vertex, and $\sigma_i = \pm 1$ ($\sigma_i' = \pm 1$) depending on whether arrows on those edges point outwards or inwards in C (C'). Then $P_0(C)$ is the sum over all these local quantities; since the AF ground state is two-fold degenerate its sign depends on the choice of C' to which C is compared. Additionally, for even L states come in pairs with equal energy but opposite spontaneous staggered polarization. To avoid cancellation of these contributions one defines the *staggered polarization* as the thermal average $P_0 := \langle\, |P_0(C)|\, \rangle$ of the absolute value of $P_0(C)$. Note that the situation is analogous to what happens for the magnetization in the two-dimensional Ising model.

For the system with PBCs Baxter derived the exact large-L asymptotics of P_0 for all temperatures [108]. This quantity becomes smoothly nonzero when the system transitions from the D to the AF phase. Let us assume that it continues to be a valid order parameter for the transition of the system with DWBCs. For this case an expression for P_0 that is manageable for all system sizes is not known. We still have

$$P_0 = \frac{d \ln Z_L^+(s)}{ds}\bigg|_{s=0} , \tag{4.9}$$

where $Z_L(s)$ is the partition function of the F model on an $L \times L$ lattice with DWBCs in the presence of an external staggered electric field of strength $s \geq 0$. The superscript '$+$' in (4.9) indicates that the absolute value of each coefficient is to be taken in order to prevent the aforementioned cancellation. No analogue of (4.4) is known when $s \neq 0$. Nevertheless the framework of the quantum inverse-scattering method (QISM) does allow for the direct computation of $Z_L(s)$, and thus P_0, for low system size. Let us indicate how this works; we refer to Ref. [117] and references therein for more about the QISM.

Let us give a description of the *staggered six-vertex model* based on Baxter [108]. We focus on the homogeneous case; inhomogeneities may be incorporated as usual. View the square lattice as being bipartite by dividing its vertices into two sets in a chequerboard-like manner. The vertex weights from Fig. 3.1 are given by $a_\pm = a$, $b_\pm = b$, while $c_\pm$ is equal to $e^{\pm s}c$ on one sublattice ('black' vertices) and to $e^{\mp s}c$ on the other ('white' vertices). These vertex weights can be encoded in the so-called *R-matrix*[5]

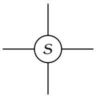

$$R(s) = \quad = \begin{pmatrix} a & 0 & 0 & 0 \\ 0 & b & e^{s}\,c & 0 \\ 0 & e^{-s}\,c & b & 0 \\ 0 & 0 & 0 & a \end{pmatrix}, \qquad (4.10)$$

defined with respect to the basis $|{}^{\rightarrow}\!\uparrow\rangle$, $|{}^{\rightarrow}\!\downarrow\rangle$, $|{}^{\leftarrow}\!\uparrow\rangle$, $|{}^{\leftarrow}\!\downarrow\rangle$ for the 'incoming' lines and $\langle\uparrow_{\rightarrow}|$, $\langle\downarrow_{\rightarrow}|$, $\langle\uparrow_{\leftarrow}|$, $\langle\downarrow_{\leftarrow}|$ for the 'outgoing' lines at the vertex. In the diagrammatic notation in (4.10) one should think of time running along the diagonal from bottom left to top right. $R(s)$ contains the vertex weights for the 'black' vertices and $R(-s)$ for the 'white' vertices.

A row of the lattice is described by the staggered (row-to-row) *monodromy matrix*

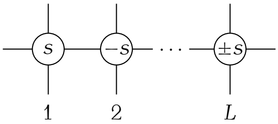

$$T(s) := \qquad (4.11)$$
$$= R_L(\pm s) \cdots R_2(-s)\, R_1(s) \ ,$$

where R_j contains the weights for the jth vertex in that row. It is customary to write $B(s)$ for the $2^L \times 2^L$ matrix sitting in the upper right quadrant of $T(s)$. This matrix accounts for a row of the staggered six-vertex model with arrows on the horizontal external edges pointing outwards as for DWBCs:

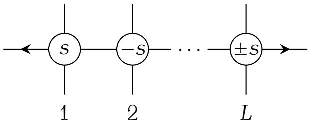

$$B(s) = \quad . \qquad (4.12)$$

The staggered domain-wall partition function can then be expressed as an entry of a 'staggered' product of L such matrices[6]:

$$Z_L(s) = \langle\downarrow\downarrow\cdots\downarrow|\, B(\pm s) \cdots B(-s)\, B(s)\, |\uparrow\uparrow\cdots\uparrow\rangle \ . \qquad (4.13)$$

---

[5] Note that $R(s) = (\delta_{s/2} \otimes \delta_{-s/2})\, R(0)\, (\delta_{-s/2} \otimes \delta_{s/2})$ for $\delta_s := \exp(s\,\sigma^z/2)$ with σ^z the third Pauli matrix, and $R(0)$ the R-matrix of the ordinary (zero-field) six-vertex model. By the ice rule one can rewrite $R(s) = (I \otimes \delta_{-s})\, R(0)\, (\delta_s \otimes I) = (\delta_s \otimes I)\, R(0)\, (\delta_{-s} \otimes I)$ with I the 2×2 identity matrix. Direct horizontal and vertical fields would correspond to $(\delta_h \otimes \delta_v)\, R(0)\, (\delta_h \otimes \delta_v)$, which can be used to compute the direct polarization in a similar fashion.

[6] The partition function for an $L \times L$ lattice with L even and PBCs (cf. Ref. [3]) is obtained by defining the staggered transfer matrix $t(s) := \mathrm{tr}\, T(s) = A(s) + D(s)$, where $A(s)$ and $D(s)$ are similar to (4.12) but with both arrows pointing left and right, respectively. Then the partition function is $Z_L^{\mathrm{PBC}}(s) = \mathrm{tr}\{[t(-s)\, t(s)]^{L/2}\}$.

For example, if $L = 1$ then $B(s)$ is $\begin{pmatrix} 0 & 0 \\ e^s c & 0 \end{pmatrix}$ and $Z_1(s) = e^s c$. The ordinary domain-wall partition function is recovered in this algebraic language as $Z_L = Z_L(0)$. We have evaluated (4.13) for general s up to $L = 12$, accounting for little over 10^{16} configurations.

To conclude this section let us comment on whether quantum integrability may be used to get some concise expression for $Z(s)$ valid for all L. The answer appears to be negative; at least the Korepin–Izergin approach mentioned in Sec. 2.II does not simply extend to $s > 0$. Indeed, one can still write four recursion relations obeyed by the inhomogeneous extension of (4.13), namely for $u_1 = v_1 - \gamma$, $u_1 = v_L + \gamma$, $u_L = v_1 + \gamma$ and $u_L = v_L - \gamma$. However, for $s \neq 0$ the inhomogeneous partition function is not symmetric in the u_i, so one does not get further Korepin-like recursion relations and the conditions do not uniquely determine $Z(s)$ for general L. The failure of $Z(s)$ to be symmetric in the u_i is of course closely related to the fact that the staggered R-matrices (4.10) do not obey a Yang–Baxter equation; even writing the latter is problematic since the triangle featuring in that relation is not bipartite. The latter also obstructs the computation of P_0 using the so-called F-basis [149].

3 Simulations

Recall that the six-vertex model is equivalent to a height model known as the (body-centred) solid-on-solid model [105]. In this picture fixed boundary conditions ensure that the height of a configuration is bounded from below and above. Going around the boundary in some direction the DWBCs correspond to the height increasing along two opposite ends, say from 0 to L, and then decreasing from L back to 0 along the other two ends. There are unique configurations of minimal and maximal height: the former corresponds to a valley of height 0 running along one diagonal, and the latter to a ridge of height L along the other diagonal. (Note that these are the ground-state configurations of the two FE phases. The AF ground state corresponds to a diamond-shaped plateau, of height as close as possible to $L/2$, surrounded by steep slopes to the pits and peaks at the corners.) The existence of configurations of minimal and maximal height allows one to use *coupling from the past* (CFTP) algorithms [150, 151], which ensure that one draws configurations from the equilibrium distribution making it a perfect simulation. Although CFTP can in principle be 'shelled' around a variety of updating schemes, in practice it is used only in combination with local updates due to the difficulties that arise when the same global update needs to be performed on both the lower and higher configuration. In this work we prefer speed over sample accuracy as this allows us to investigate much larger systems, thus improving the reliability of our subsequent analysis of the thermodynamic limit. Rather than CFTP we thus use the full lattice multi-cluster algorithm [152], as in Ref. [3], with a reported dynamic exponent $z = 0.005 \pm 0.022$ for PBCs [153], so that the correlation time can be considered independent of system size in practice. The accuracy of our simulations is checked in Sec. 4.4 against the theoretical expressions that were reviewed in Sec. 4.2.

Our results are procured from Monte Carlo simulations using the full lattice multi-cluster algorithm in combination with parallel tempering [14]. We use the multi-histogram method [22, 23] to interpolate observables, the energy and staggered polarization in particular, in a temperature range around the critical temperature. The F model is well suited for both parallel tempering and the multi-histogram method as the specific heat is analytically known and bounded [cf. (4.14) below] such that a set of temperatures can be constructed *a priori* at which the energy distributions of 'adjacent' configurations overlap significantly. Given a configuration at inverse temperature β, its neighbouring configurations are set at $\beta' = \beta \pm \beta/\sqrt{C_v}$. In each simulation the acceptance probability of swapping two configurations is never less than 47%. After each update a measurement is taken, with a minimum of 10^6 measurements per system size per temperature, at up to 30 different temperatures per system size. At each measurement we determine the total energy and staggered polarization, calculated based on the description in the first paragraph of Sec. 2.III, of the system as well as the local vertex density at each vertex in the system. In principle one can estimate the thermal average of any time-independent (local) observable that can be defined for the system, such as arrow correlations, in a similar fashion. Note that all cluster updates that would change the arrows on the boundary are rejected to preserve the DWBCs.

4 Results

4.1 Energy and specific heat

Unlike the energy, the partition function itself can not be directly measured in Monte Carlo simulations. Exceptions are very small systems ($L \leq 6$) for which our simulations happen to sample all microstates so that we are able to reconstruct the full staggered partition function. The resulting expressions for $E(\beta) = \langle E(C) \rangle$ and $P_0(\beta)$ precisely match those obtained via the QISM as described in Sec. 2.III. In general just a part of the phase space is sampled so the partition function cannot be reconstructed as the total energy $E(\beta)$ is not known for all temperatures. However, the multi-histogram method allows us to use simulations done at finitely many temperatures to determine the partition function, up to an overall factor, on some finite temperature range.

Figure 4.3 shows the energy per site $e(\beta) := E(\beta)/L^2$ and the specific heat per site $c_v(\beta) := C_v(\beta)/L^2$ as functions of inverse temperature. The simulation data are shown together with the exact expressions for infinite size extracted from Eqs. (4.5) and (4.7) using

$$E(\beta) = -\frac{\partial \ln Z}{\partial \beta} , \quad \frac{C_v(\beta)}{\beta^2} = -\frac{\partial E}{\partial \beta} = \frac{\partial^2 \ln Z}{\partial \beta^2} , \tag{4.14}$$

which yields $e(\beta_c) = 2/3$ and $c_v(\beta_c) = 8 \ln^2(2)/45$. We observe a convergence of the simulation data to the analytically known asymptotic values over all simulated temperature ranges.

To investigate the effects of the subleading corrections in the system size for the partition function further we focus on the critical point. Because of the smoothness of the partition function we can take the expressions for the disordered regime and evaluate them at the phase transition. Starting from Eq. (4.5) we find the following expression for the energy per site $e_L(\beta_c)$ at the critical point for system size L:

$$e_L(\beta_c) = \frac{2}{3} - \frac{4}{3\pi^2} \frac{\ln L}{L^2} - \frac{C_1}{L^2} + O(L^{-(\alpha+2)}) , \tag{4.15}$$

with $C_1 = -\lim_{\gamma \to 0^+} C'_D(\gamma)/[\gamma\, C_D(\gamma)]$ an unknown parameter. Equation (4.15) can be checked against the expression for the energy derived directly from (4.4) for small system sizes ($L \leq 16$) as well as the simulation data for moderate system sizes. This is shown in Fig. 4.4 where $e_\infty(\beta_c) - e_L(\beta_c)$ and $E_\infty(\beta_c) - E_L(\beta_c)$ are plotted versus system size. The best unweighed fit, including only the asymptotically next-to-leading correction $C_1 = 0.669 \pm 0.019$, already shows very good agreement with both the exact and numerically obtained values. For $L \leq 141$ this next-to-leading correction, $\sim 1/L^2$, is more important than the asymptotically leading correction, $\sim \ln L/L^2$. This means that even at $L \sim 10^{21}$ the two corrections in (4.15) just differ by a factor 10. Also note the high precision at which both the leading and first subleading corrections are measurable for systems as large as $L = 256$, for which these corrections are of the order 10^{-5}.

A best estimate for the value of α can be found by assuming that the subleading terms in (4.5), i.e. the $O(L^{-\alpha})$, is of the form $g(\gamma)\, L^{-\alpha}$. This yields

$$e_L(\beta_c) \simeq \frac{2}{3} - \frac{4}{3\pi^2}\frac{\ln L}{L^2} - \frac{C_1}{L^2} + \frac{C_2}{L^2\,(L^\alpha + C_3)}\ , \tag{4.16}$$

where $C_2 = \lim_{\gamma\to 0^+} g'(\gamma)/\gamma$ and $C_3 = \lim_{\gamma\to 0^+} g(\gamma)$ are again unknown. We assume that these limits make sense; the corrections are finite and must disappear for infinite systems. If we use our best value for C_1 and fit Eq. (4.16) to the energies of small systems obtained from direct computation of (4.13) (see again Fig. 4.4), the best estimates are $C_2 = 1.6 \pm 1.2$, $C_3 = 14 \pm 12$, and $\alpha = 1.91 \pm 0.36$[7]. The inclusion of these subleading correction does improve the fit qualitatively although error margins for best estimates of the parameters C_2 and C_3 are very large. With these values the crossover point where the terms proportional to C_1 and C_2 become comparable occurs already at $L = 3.9$. The exact analytical values for the energy can be computed using (4.4) or (4.13). We have done so for $L \leq 16$; in either case most computation time was spent on the derivation of the energy from the partition function at the critical point rather than the calculation of the partition function itself.

---

[7] In fact, Ref. [132, Thm. 6.1.3] shows that $\alpha \geq 1$. Our value would mean that $b_1 = 0$ in the proof of that result. In principle it is possible to check this analytically, but the expression for b_1 is rather complicated. We thank P. Bleher for correspondence about this point.

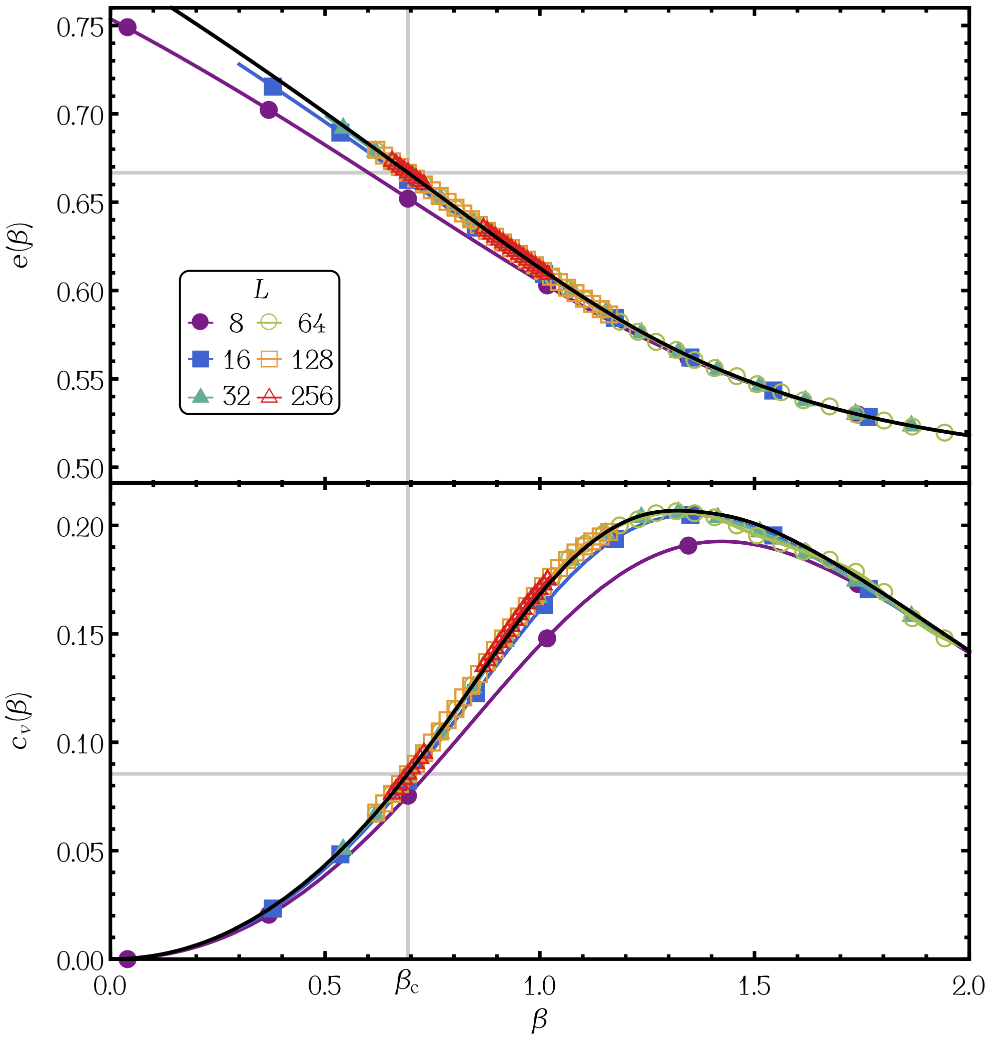

Figure 4.3. The average energy per site $e(\beta)$ (top) and specific heat per site $c_v(\beta)$ (bottom) as functions of inverse temperature β. The critical points at β_c are indicated by the gray lines. The black lines are the exact asymptotic expressions extracted from Eqs. (4.5) and (4.7). From the data points, indicating the temperatures at which the simulations are done, the coloured solid lines are calculated using the multi-histogram method. For both observables we see a convergence of the data to the analytically known expressions in the thermodynamic limit.

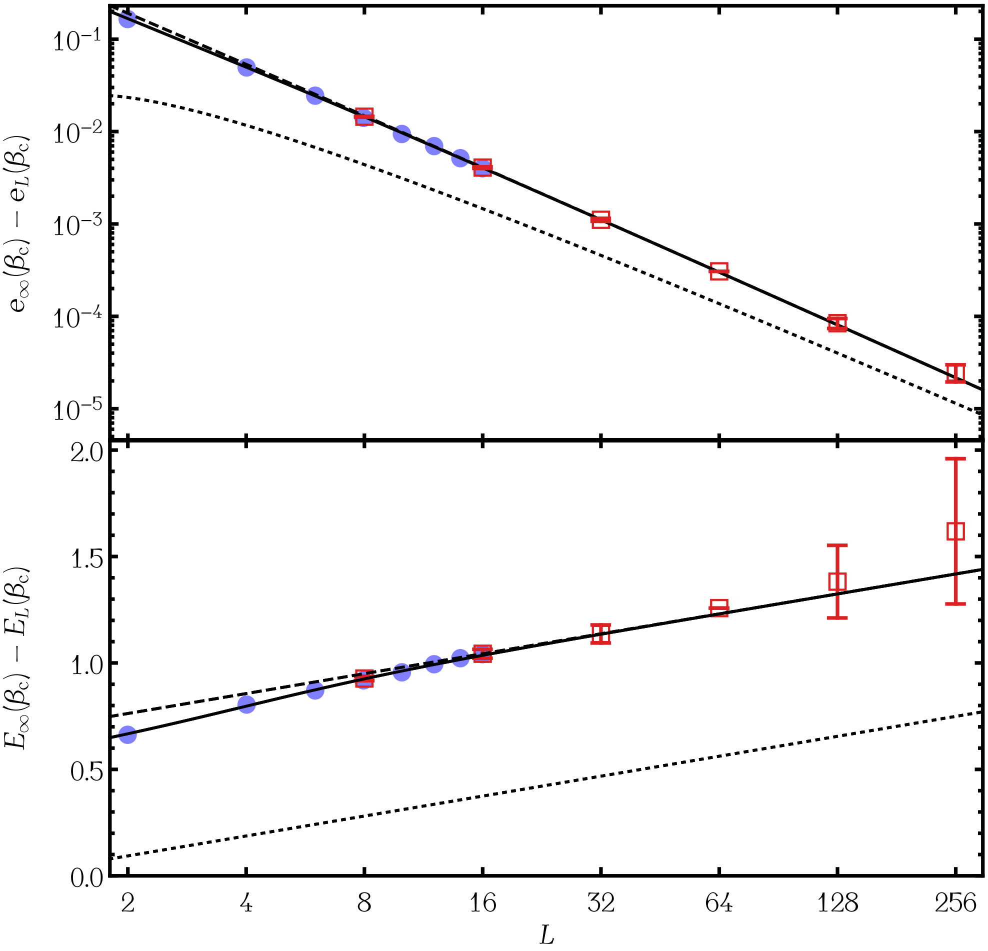

Figure 4.4. The difference between the energy per site (top) and total energy of the system (bottom), with $E_\infty(\beta_c) := L^2\,e_\infty(\beta_c) = 2\,L^2/3$, is shown as a function of system size. The solid blue disks represent the exact known values for small system sizes obtained from Eq. (4.4). The open red squares denote best estimates obtained from our simulations. The error bars are estimates based on the fluctuations in the energy and the number of measurements taken. The expressions from Eq. (4.15) with only the leading correction ($C_1 \equiv C_2 \equiv 0$) and with first subleading correction ($C_1 = 0.669 \pm 0.018$), as well as the expression from Eq. (4.16) ($C_2 = 1.6 \pm 1.2$, $C_3 = 14 \pm 12$, $\alpha = 1.91 \pm 0.36$) are shown as dotted, dashed, and solid curves, respectively.

4.11 The logarithmic derivative of P_0

Similar to our work in Ref. [3] we now study $d\ln P_0/d\beta$, which must have a peak at the critical point for infinitely large systems if P_0 is a true observable of the infinite-order phase transition. As for the energy the multi-histogram method is used to obtain $d\ln P_0/d\beta$ by interpolation between the temperatures at which the systems were simulated. Figure 4.5(a) shows $d\ln P_0/d\beta$ as a function of inverse temperature for various system sizes up to linear size $L = 256$. To obtain a numerical collapse for each system size we determine the peak coordinates $(\beta_{\max}, h_{\max})$ as well as the typical width w, which is defined as the absolute difference between $\beta_{\max}$ and the lower temperature at which $d\ln P_0/d\beta$ attains 95% of the peak height. The numerical collapse is shown in Fig. 4.5(b); unfortunately it is less clean than its counterpart for PBCs in [3].

Previously we found behavioural similarities between $d\ln P_0/d\beta$ and the susceptibility χ of the staggered polarization for PBCs [3]. Since there are no known analytical expressions for the asymptotic behaviour of P_0 for DWBCs we fall back on the leading corrections known for PBCs [103]. In the case of PBCs the leading correction for the peak position of χ is of the form $\ln^{-2} L$, and so for DWBCs one could make the educated guess that the form of the peak of $d\ln P_0/d\beta$ scales like

$$x = A_x + B_x \ln^{-2} L + C_x \ln^{-3/2} L + D_x \ln^{-4} L, \tag{4.17}$$

where x is either the inverse peak height $h_{\max}^{-1}$, the peak width w, or the position $\beta_{\max}$ of the peak. Figure 4.6 shows these quantities as a function of $\ln^{-2} L$ with the best fit of Eq. (4.17) to the three characteristics. The best estimates from an unweighed fit to all data points for the peak height are $A_{h_{\max}^{-1}} = -0.01 \pm 0.03$, $B_{h_{\max}^{-1}} = 5.4 \pm 1.1$, $C_{h_{\max}^{-1}} = -3 \pm 3$, and $D_{h_{\max}^{-1}} = -2 \pm 3$. For the peak width the best estimates are given by $A_w = -0.009 \pm 0.009$, $B_w = 2.4 \pm 0.4$, $C_w = -5 \pm 1$, and $D_w = 3.0 \pm 0.8$. A similar fit for $\beta_{\max}$ does not seem to work. Indeed, the best estimate for $A_{\beta_{\max}} = 0.83 \pm 0.02$ is far from the analytically known value $\beta_c = \ln 2$. Alternatively one could fix $A_{\beta_{\max}} = \beta_c$, in which case the fit does not go through the data in a clean fashion. Although this method does not reliably give an estimate for the critical point it does show the convergence of $d\ln P_0/d\beta$ to a Dirac delta-like distribution as the system size tends to infinity. From Fig. 4.6 we see that in practice direct computation using (4.13) cannot be used outside of the regime in which subleading finite-size corrections are important. Simulations reveal the decrease in $\beta_{\max}$ for increasing system size.

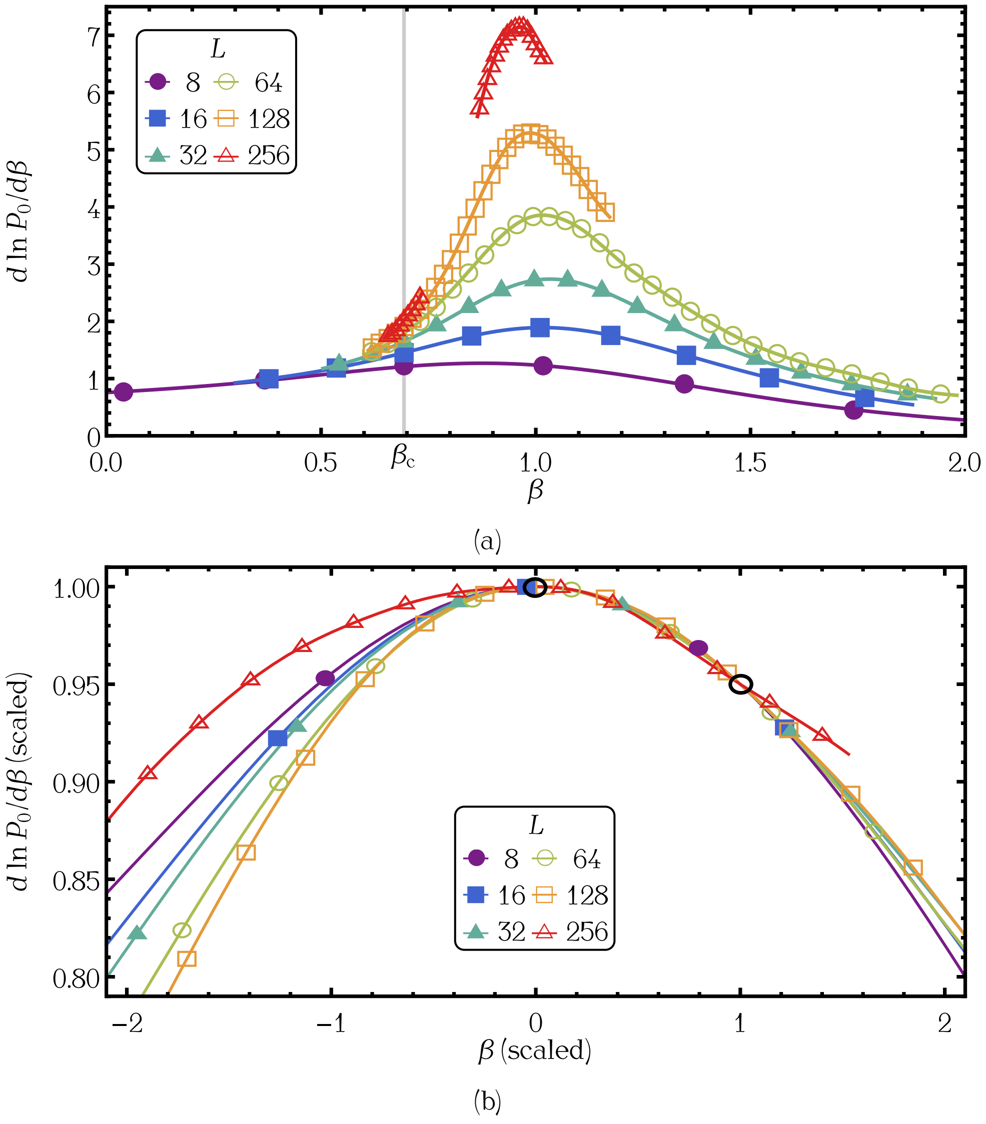

Figure 4.5. The observable $d \ln P_0/d\beta$ is shown in (a) as a function of inverse temperature β for various system sizes up to $L = 256$. In the thermodynamic limit, under the assumption that P_0 is a valid order parameter, this function must have its peak at the critical point. In (b) the peak and the point where the curves attain 95% of their peak height (at higher β) are scaled on top of each other, with the two points indicated by black circles. From this collapse we extract the peak position and typical width for further analysis; cf. Fig. 4.6.

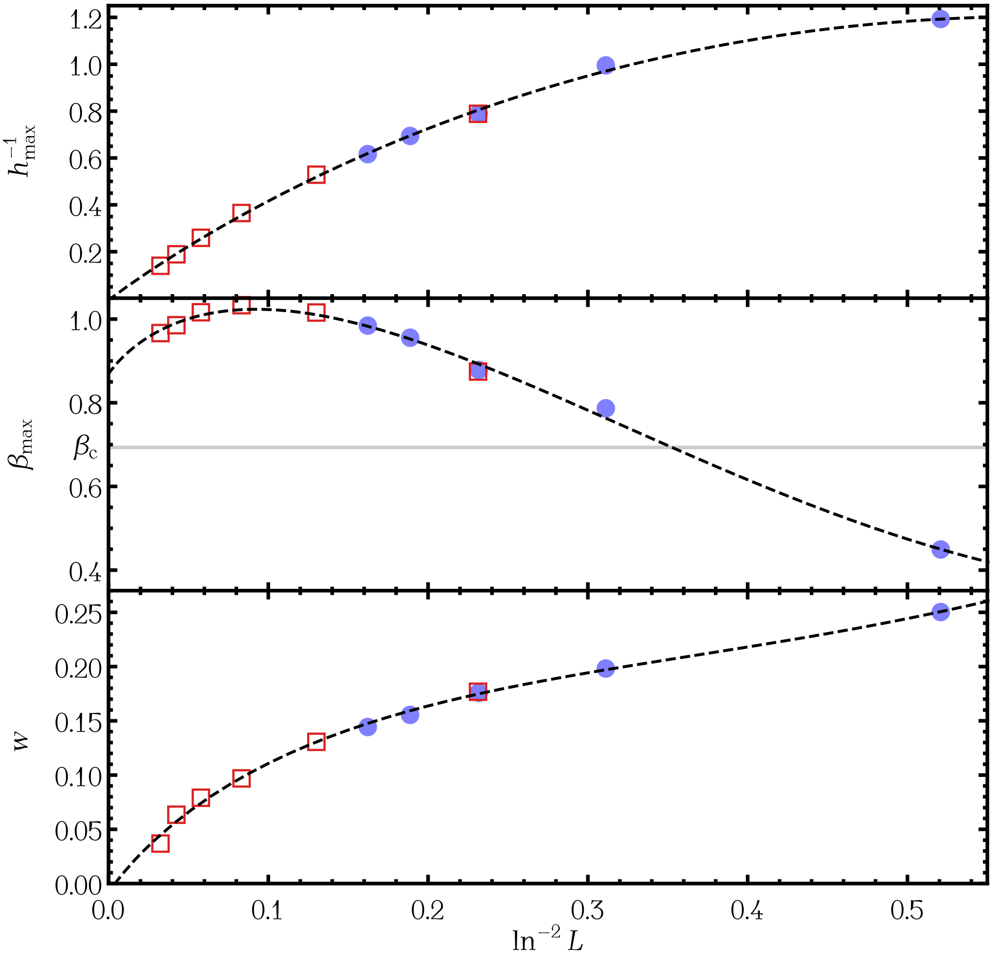

Figure 4.6. Values of the inverse peak height $h_{\max}^{-1}$ (upper panel), peak position $\beta_{\max}$ (central panel), and peak width w (lower panel) are shown for $d \ln P_0 / d\beta$ up to system size $L = 256$ as a scaled function of $\ln^{-2} L$. Exact values for small system sizes obtained from Eq. (4.13) are shown as solid blue disks and best estimates obtained from our simulations as open red squares. The best unweighed fits of the form (4.17) are drawn as black dashed lines. For $\beta_{\max}$ a fit through all data points results in a best estimate for the critical point $A_{\beta_{\max}} = 0.87 \pm 0.03$ far from the analytically known value $\beta_c = \ln 2 \approx 0.69$. For $h_{\max}^{-1}$ ($A_{h_{\max}^{-1}} = -0.01 \pm 0.03$, $B_{h_{\max}^{-1}} = 5.4 \pm 1.1$, $C_{h_{\max}^{-1}} = -3 \pm 3$, $D_{h_{\max}^{-1}} = -2 \pm 3$) and w ($A_w = -0.009 \pm 0.009$, $B_w = 2.4 \pm 0.4$, $C_w = -5 \pm 1$, $D_w = 3.0 \pm 0.8$) the fits work well and are in agreement with $d \ln P_0 / d\beta$ becoming a Dirac delta-like distribution as $L \to \infty$.

4.III Arctic curves

So far we have investigated global quantities. For inhomogeneous (not translationally invariant) systems such as the F model with DWBCs such properties provide rather coarse information, as a lot of the local information is averaged away.

Figure 4.7 shows the thermally averaged c-vertex density $\rho(c)$, together with several contour lines, for a system of linear size $L = 512$ at various temperatures: zero temperature ($\beta \to \infty$, $\Delta \to -\infty$), below the critical point ($\beta = 2\beta_\mathrm{c}$, $\Delta = -7$), at the critical point ($\beta_\mathrm{c} = \ln 2$, $\Delta = -1$), at the free-fermion point ($\beta = \beta_\mathrm{c}/2$, $\Delta = 0$), and at infinite temperature ($\beta = 0$, $\Delta = 1/2$). For nonzero temperature 10 independent simulations, each yielding 10^6 measurements, were performed per temperature to calculate the local vertex density. We use the global symmetries described in App. 4.A to get a smoother $\rho(c)$-profile by averaging at a given Δ. At the centre $\rho(c)$ is always at a maximum. For zero temperature, the critical temperature, and the free-fermion point the maximal values are 1 and about 2/3 and 1/2, respectively. At low temperatures there is a AF region, with constant $\rho(c)$ close to unity signalling its ordered nature. As the temperature rises from zero a temperate region emerges that encloses the central AF region, completely engulfing it at the critical point; cf. Ref. [113]. The arctic curves, exactly known for $\Delta = -\infty$ and $\Delta = 0$ [137, 138] and conjectured for $\Delta < 1$ [139, 140, 141] are also shown in Fig. 4.7. The outer contours are drawn at temperature-dependent values for $\rho(c)$ (see Table 4.1) chosen such that those contours are qualitatively comparable to the known and conjectured forms of the arctic curves. We see that our data match very well with the analytic expressions; for nonzero temperature the deviation from zero of the values given in Table 4.1 is a measure of the influence of finite-size effects.

4.IV Oscillations in vertex densities

Finally we turn to the structure inside the temperate region. In Fig. 4.8 we show the thermally averaged densities ρ along the diagonal from the FE region dominated by b_--vertices ($r = L/\sqrt{2}$, bottom left corner in Fig. 4.7) to the centre ($r = 0$) of a system of size $L = 512$ at the critical point $\Delta = -1$. Along this diagonal one has $\rho(a_+) = \rho(a_-)$. Moreover if one considers r to cover the full diagonal, $-L/\sqrt{2} \leq r \leq L/\sqrt{2}$, then $\rho(a_\pm)$ and $\rho(c_\pm)$ are even as functions of r while $r \mapsto -r$ reverses $\rho(b_+) \leftrightarrow \rho(b_-)$. This once

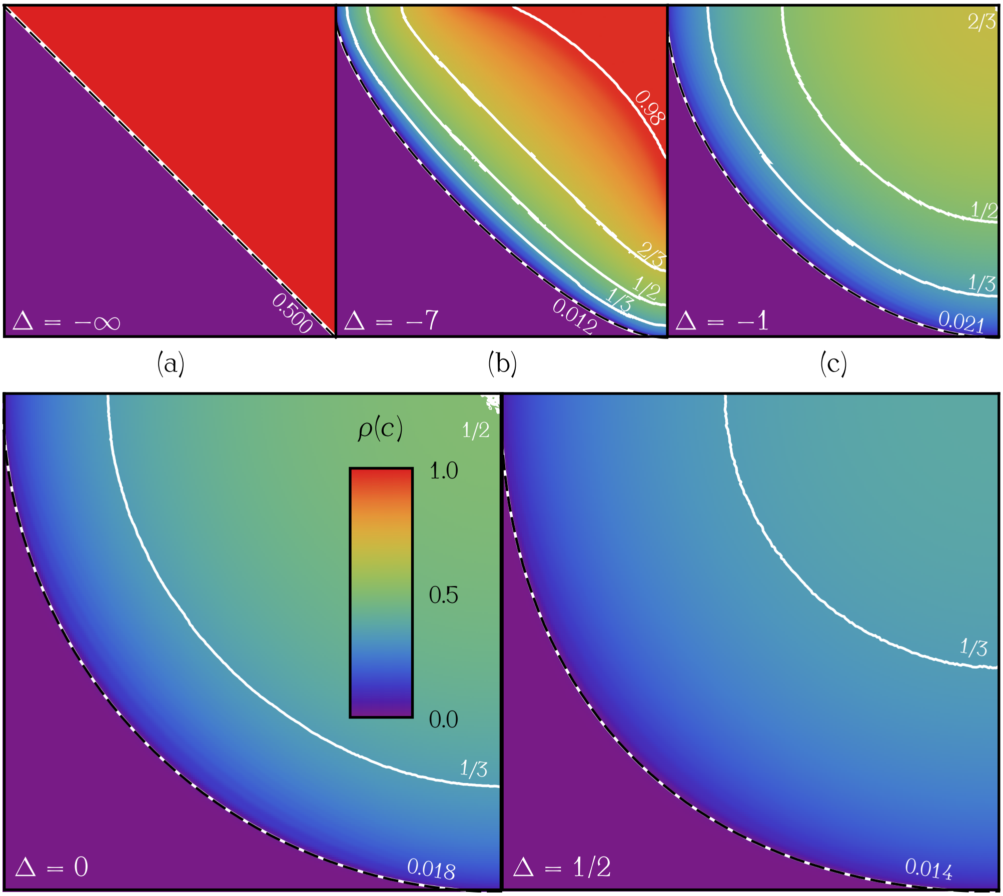

(a) (b) (c)

(d) (e)

Figure 4.7. The thermally averaged density $\rho(c)$ of c-vertices at $L = 512$ show phase separation at different temperatures. The density lies between zero (shown in purple) and one (red). White solid contour lines are drawn at the values $1/3, 1/2, 2/3$, and 0.98, as indicated, of $\rho(c)$. The outer white solid contours are drawn at temperature-dependent values of $\rho(c)$ (see Table 4.1) that give the best qualitative match with the arctic curves [137, 138, 139, 140, 141], which are shown as dashed black curves. At zero temperature (a) the AF region is a diamond. At slightly elevated temperatures (b) the AF and FE regions are separated by a temperate region. As the temperature increases past its critical value (c), at which the AF region disappears, the arctic curve deforms to a circle at the free-fermion point (d). The system at infinite temperature is shown in (e), in which the arctic curve is a sort of inflated circle, with the arcs deformed somewhat towards the corners of the domain.

	(a)	(b)	(c)	(d)	(e)
β	∞	$2\beta_c$	$\beta_c = \ln 2$	$\beta_c/2$	0
Δ	$-\infty$	-7	-1	0	$1/2$
$\rho(c)$	0.500	0.012	0.021	0.018	0.014

Table 4.1. The values for β and Δ at which the simulations for Figs. 4.7(a)–4.7(e) were performed are given together with the values for $\rho(c)$ at which the outer contours are drawn. For finite Δ this gives a measure of the deviation from the asymptotic values $\rho(c) = 0$ due to finite-size effects.

more allows us to exploit the global symmetries as explained in App. 4.A to average for the densities of $\rho(a_\pm)$ and $\rho(b_\pm)$ in Fig. 4.8. Note that some of these transformations exchange $a_\pm \leftrightarrow b_\pm$ as they involve arrow reversal to preserve the boundary conditions.

Using numerics, Syljuåsen and Zvonarev [133] first noticed oscillatory behaviour ('small wiggles') of the arrow polarization density for $\Delta < -1$; see Fig. 6 therein[8]. Recently Lyberg *et al.* [135] recovered these oscillations while studying the local vertex densities exactly; cf. the asymptotic expression of the arrow polarization found for $\Delta = 0$ in Ref. [123], as well as numerically. In Fig. 4.8 we observe oscillations for all of the vertex densities in the temperate region. The wavelengths of these oscillations are comparable functions of r for each of the vertices. For lower temperatures these ripples are more pronounced yet the region in which they appear, *viz.*,the temperate region, becomes smaller. The thermally averaged densities $\rho(c_+)$ and $\rho(c_-)$ are in anti-phase (cf. Fig. 4.8) so these oscillations are masked if just $\rho(c)$ is considered as in Fig. 4.7. The complicated oscillatory behaviour in the temperate region can more clearly be seen from the thermally averaged c-vertex density difference $\delta\rho(c) := \rho(c_-) - \rho(c_+)$. Let us emphasize that we focus on the density difference for the c-vertices because $\rho(c_\pm)$ are in anti-phase, so $\delta\rho(c)/2 = \rho(c)/2 - \rho(c_+)$ allows us to study the oscillations of $\rho(c_+)$ about its 'average' by approximating the latter with the average $\rho(c)/2$ of $\rho(c_\pm)$. We should also point out that $\rho(c)$ itself exhibits oscillations, visible near the arctic curve for finite Δ in Fig. 4.7; we have verified, however, that the $\rho(c)$- and $\delta\rho(c)$-oscillations have a phase difference of $\pi/2$, so the ripples in Fig. 4.7 are related to the 'FE oscillations' that we will introduce momentarily.

---

[8] We thank I. Lyberg for bringing this to our attention.

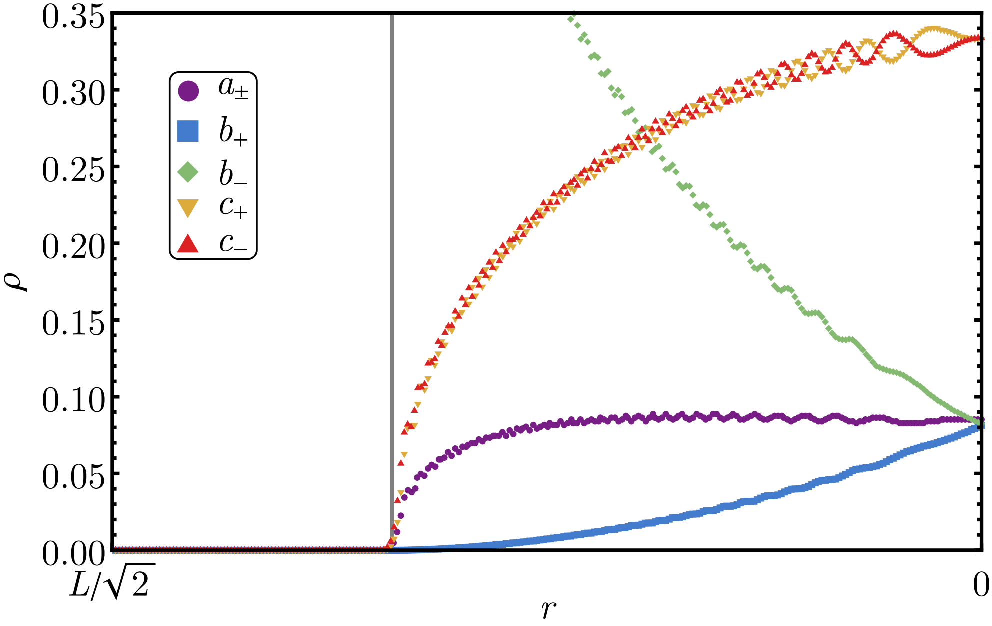

Figure 4.8. The thermally averaged densities ρ for all six vertices in a system of linear size $L = 512$ at the critical point $\Delta = -1$ are shown along the diagonal from the b_--dominated FE region to the centre at $r = 0$. The grey vertical line marks the transition between the FE and temperate region [141]. Each vertex density oscillates in the temperate region. Note that $\rho(c_\pm)$ are in antiphase around their average.

To study the dependence on the system size of the oscillations in the temperate region Fig. 4.9 shows $\delta\rho(c)$ along the diagonal for system sizes $L = 32$ up to $L = 512$. The wavelength of the oscillations is always largest at the edges of the temperate region. We observe a sublinear growth of the wavelength in L. A best unweighed fit to the distance between the centre of the system ($r = 0$) and the position of the maximum of $\delta\rho(c)$ gives $(0.67 \pm 0.06)L^{(0.553\pm0.016)}$. Such a fit cannot be made for the maximal amplitude as our data are not accurate enough to distinguish between logarithmic or power-law behaviour. Still Fig. 4.9 does clearly show that the average wave amplitude monotonically decreases with system size, suggesting that the oscillations are finite-size effects, as was conjectured in Ref. [133]; cf. Sec. 4 of Ref. [135].

Figure 4.10 shows the profile of $\delta\rho(c)$ for systems at $\Delta = -1$ and $\Delta = -7$.

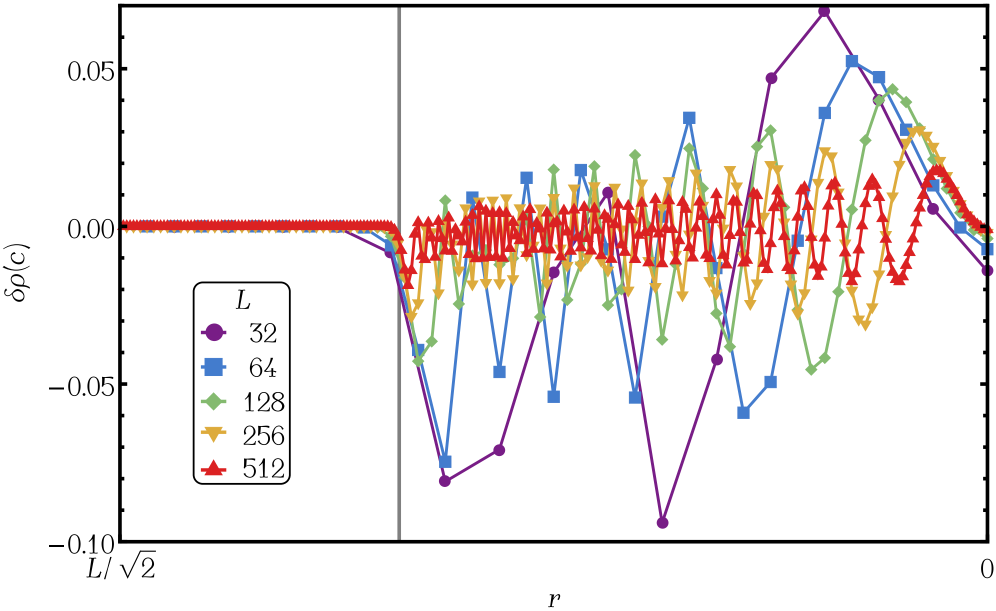

Figure 4.9. The difference $\delta\rho(c)$ is shown as a function of distance r along the diagonal to the centre (at $r = 0$) for systems up to size $L = 512$ at $\Delta = -1$. The coloured lines are a guide to the eye, and the grey vertical line denotes the transition between the FE-frozen and temperate region as in Ref. [141]. The wavelength of the oscillations seems to increase sublinearly while the average wave amplitude decreases monotonically with system size, suggesting that these are finite-size effects.

Inside the temperate region there are at least two types of oscillations: one type, let us call them 'AF oscillations', follows the boundary between the AF-frozen and temperate regions (which at $\Delta = -1$ degenerates to the horizontal and vertical lines separating the quadrants), while the other type, 'FE oscillations', follows the contours of the arctic curve between the temperate and FE-frozen regions. (Both of these types of oscillations may be discerned in Ref. [135, Fig. 6] too, and the FE oscillations arguably already in Figs. 10 and 11 of Ref. [133]. We should point out that in Ref. [133] the term 'AF oscillations' is instead used for the chequerboard patterns of $c_{\pm}$-vertices typical for AF order.)

Interestingly, upon closer inspection of Fig. 4.10 we observe a chequerboard-like pattern inside the AF oscillations (cf. Ref. [135, Fig. 6,

$\Delta = -10$]), signalling site-to-site anti-correlations for $\rho(c_\pm)$ that persist over long distances along the oscillations, and justifying the name 'AF' for these types of oscillations. Note that, albeit in a weaker form, these chequerboards survive thermal averaging: unlike the one in the AF region for even L it is a physical property of the system. We observe that the chequerboards in adjacent oscillations are opposite, so the bands separating the oscillations can be understood as the result of destructive interference between the two chequerboards. Also note that such chequerboard-like anti-correlations are invisible when one focusses on the densities along the diagonal. Next we turn to the FE oscillations. The profile of $\rho(b_-)$ reveals that the interior of the FE oscillations near the frozen region dominated by b_- are also dominated by b_-, and similar statements are true for the other quadrants. Figure 4.10 further shows that the regions between the FE oscillations are dominated by c_--vertices ($\delta\rho(c) > 0$) to account for the constraint $\#c_- > \#c_+$ imposed by the DWBCs. Notice that as the FE oscillations approach the median, at the top of Fig. 4.10, they reduce to a chequerboard pattern on the median to merge with the interior of the largest AF oscillation.

To justify our observations let us explain in more detail how Fig. 4.10 was obtained. We use the same data as for Fig. 4.7, based on 10 independent simulations each with 10^6 measurements of local vertex density. We use the model's global symmetries to produce further configurations from those obtained from our simulations and sample over the full phase space as described in App. 4.A. Averaging over these configurations we obtain the profile for $\delta\rho(c)$ shown in Fig. 4.10, which correctly vanishes both in the FE and AF regions. For even as well as odd L, however, the site-to-site anti-correlations between the AF oscillations in the *temperate* region survive this averaging: unlike for the chequerboard in the AF region for even L, this seems to be a *statistical* property of the system. See also (the end of) App. 4.A.

Besides the AF and FE oscillations following the curves separating the temperate and corresponding frozen regions there are also additional 'higher-order' oscillations in $\delta\rho(c)$ that form intricate patterns in the temperate region that are barely visible in Fig. 4.10. To visualize these oscillations more clearly we truncate $\delta\rho(c)$ in the upper panel of Fig. 4.11 at 10% of the minimal and maximal values from the upper panel of Fig. 4.10. Even though the relative errors sometimes exceed the average value for very small $\delta\rho(c)$ the patterns exhibit a lot of structure, and cannot be attributed to random noise. These higher-order oscillations exhibit several saddle-point-like patterns around the centre of the temperate region. The structure is similar for lower Δ; we

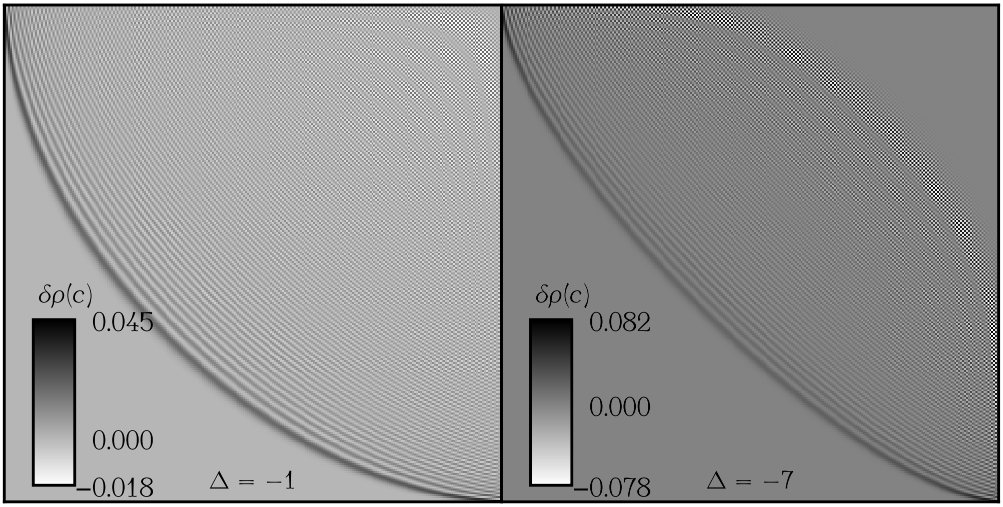

Figure 4.10. [High quality online.] The thermally averaged density difference $\delta\rho(c)$ is shown for a system of size $L = 512$ at $\Delta = -1$ (upper panel) and $\Delta = -7$ (lower panel). Each pixel corresponds to a vertex. The FE-frozen region in the bottom left contains only b_--vertices. Below the critical point the AF-frozen region appears (lower panel) in which $\delta\rho(c) = 0$ due to the two-fold degeneracy for even L. Inside the intermediate temperate region at least two types of oscillations are visible. There appear to be chequerboard-like patterns in the 'AF oscillations' even after thermal averaging, with opposite chequerboards in neighbouring oscillations. The 'FE oscillations' are dominated by the vertices constituting the FE-frozen region (here b_-), with $\delta\rho(c) > 0$ between them.

have chosen $\Delta = -1$ to get the largest temperate region. Some higher-order oscillations can be found in Fig. 7 of Ref. [135] for $\Delta = -10$.

The oscillations persist above the critical point. At $\Delta = -1/2$ one can see FE oscillations in Ref. [135, Fig. 6]. Going deeper into the D phase the profiles of $\delta\rho(c)$ on the free-fermion line ($\Delta = 0$) and at the ice point ($\Delta = 1/2$) are shown in the lower panels of Fig. 4.11. At $\Delta = 0$ the FE oscillations are still clearly visible. Interestingly, even though the AF region has disappeared it leaves behind a 'ghost' in the form of AF oscillations. Close inspection suggests there are higher-order oscillations too, with at least one saddle-point-like feature. At $\Delta = 1/2$ most structure of the temperate region is beyond the resolution of our data, yet one can still see weak FE oscillations as well as the tails of AF oscillations in the top-left and bottom-right corners of that panel.

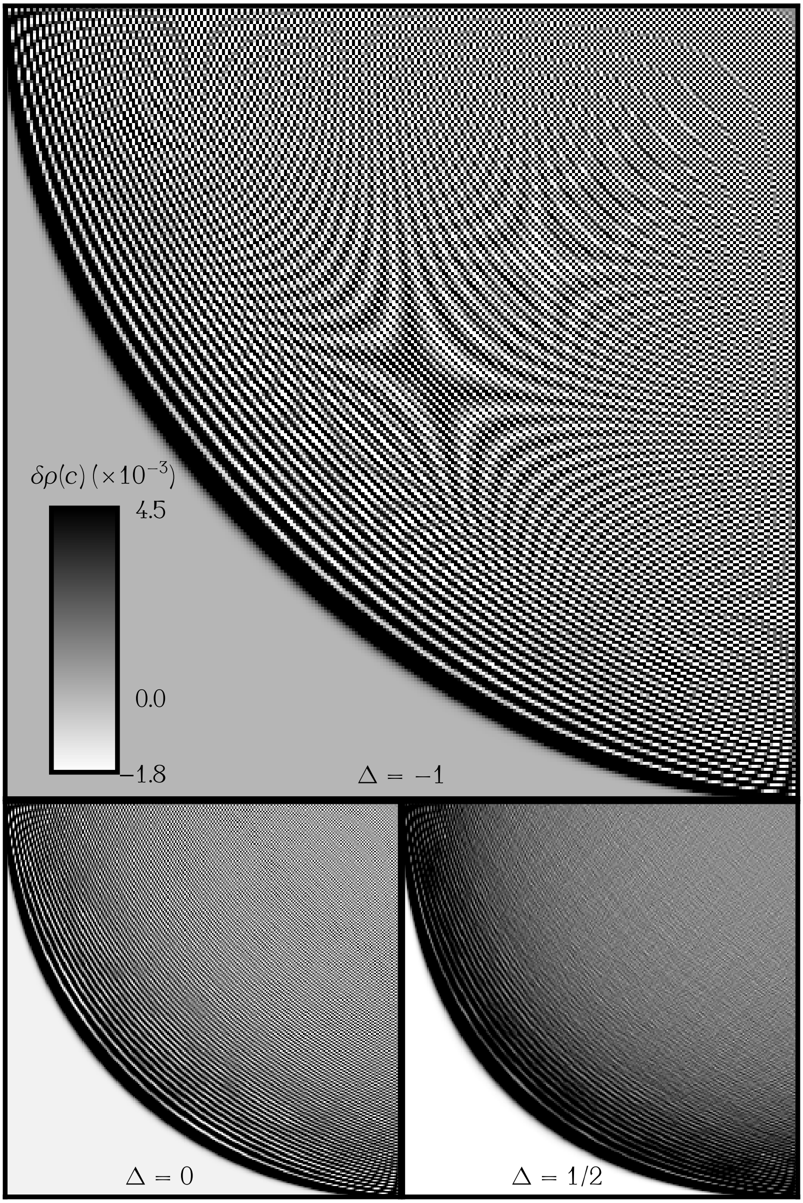

Figure 4.11. [High quality online.] The thermally averaged $c_\pm$-density difference $\delta\rho(c)$ for size $L = 512$ at $\Delta = -1$ (upper panel), truncated at 10% of the values from the upper panel in Fig. 4.10. Every pixel represents one vertex. This reveals weak 'higher-order' oscillations in the temperate region with various saddle-point-like features; we can distinguish at least four of these along the diagonal, and more along the top and right. The lower panels show $\delta\rho(c)$ at $\Delta = 0$ (left) and $\Delta = 1/2$ (right), each again truncated at 10% of its minimal and maximal value.

5 Summary and outlook

In this work we have used Monte Carlo simulations to study the F model with DWBCs. Although a closed form for the partition function is analytically known for all system sizes, in practice it is particularly useful for the exact computation of certain observables for fairly small systems and to obtain the asymptotic form and its finite-size corrections. Simulations allow for the investigation of systems of moderate size to complement such analytic results as well as to study properties that are not (yet) understood from an analytic point of view.

We have given best estimates for the parameters in the first three subleading finite-size corrections to the energy derived from the asymptotic partition function in Eq. (4.5) at the critical point by fits to the average energies obtained from simulations. This tests the reliability of our simulations; they are precise enough to distinguish the different subleading corrections (Fig. 4.4). The best estimates for the parameters suggest that the first subleading correction is non-negligible in comparison to the leading correction even for macroscopically sized systems, with $L \sim 10^{21}$. We find $\alpha = 1.91 \pm 0.39$ for a previously unknown parameter in the asymptotic expression (4.5) of the domain-wall partition function in the disordered regime found by Bleher and Fokin [129].

Following joint work with Duine and Barkema [3] we have further investigated the order parameter based on the staggered polarization P_0, of which we gave a description in the framework of the quantum-inverse scattering method (QISM). From a theoretical point of view it would be interesting to explore whether it is possible to adapt Baxter's work [108] to obtain an exact expression for P_0 in the case of domain walls, at least in the thermodynamic limit, but we have not done so in the present work. If P_0 is a true order parameter for the model's IOPT, i.e., it is constant on one side of the critical temperature and smoothly starts to change at the phase transition, then the observable $d \ln P_0/d\beta$ must by definition have a divergence at the critical point for infinitely large systems. Using finite-size scaling, and extrapolating to the asymptotic case we have found that $d \ln P_0/d\beta$ does indeed converge to a delta-distribution (see Fig. 4.6), although it fails to give an accurate estimate for the (analytically known) temperature at which the phase transition occurs. Of course the DWBCs together with the ice rule make the system that we have investigated rather special; the observable proposed in Ref. [3] may still be useful for the investigation of other models exhibiting an IOPT. One could also try using the susceptibility of P_0 instead; most of its peaks lie outside our simulation range, though the peaks that are visible appear to have a comparable quality for finite-size scaling.

In addition to these global (spatially averaged) properties we have studied local properties of the system. The profiles of the c-vertex density $\rho(c)$ obtained for systems of size $L = 512$ at various temperatures with $\Delta \leq 1/2$ are shown in Fig. 4.7. In the antiferroelectric (AF) phase our simulations corroborate the coexistence of three spatially separated phases as found in Refs. [113, 133], with a flat central region exhibiting frozen AF order surrounded by a disordered (D) 'temperate' region and ferroelectrically (FE) ordered corners. Our data agree very well with the arctic curves conjectured by Colomo and Pronko [140] and Colomo, Pronko and Zinn-Justin [141]. It would be desirable to have similar analytic expressions for the 'antartic curve' separating the temperate and AF-frozen regions for $\Delta < -1$.

Regarding the structure inside the temperate region our simulations confirm the oscillations first found by Syljuåsen and Zvonarev [133] and recently recovered by Lyberg *et al.* [135]. Our findings agree with those works, reproducing the patterns visible there, and uncover interesting additional features. Each vertex density oscillates with the same dependence of the wavelength on the position along the diagonal (Fig. 4.8). Our data confirm the conjecture of [133], in accordance with Ref. [135], that these oscillations are finite-size effects: their wavelengths appear to grow sublinearly — roughly as $(0.67 \pm 0.06)L^{(0.553\pm0.016)}$ — and their average amplitudes decrease with system size (Fig. 4.9). Our most detailed result regarding the structure of the temperate region are Figs. 4.10 and 4.11. Here we have chosen to focus on the density difference for the c-vertices since $\rho(c_\pm)$ are in anti-phase (cf. Fig. 4.8), so $\delta\rho(c) := \rho(c_-) - \rho(c_+)$ allows us to study the deviation of one type of vertex around its 'average' without having to know an expression for the latter. We find several types of oscillations. The 'AF' oscillations close to the AF-frozen region appear to be made up of chequerboards of $c_\pm$-vertices that (unlike the AF region in case of even L) survive thermal averaging for even as well as odd L, and are opposite between neighbouring oscillations. The 'FE' oscillations near the FE-frozen region are dominated by the vertices constituting that frozen region; between these oscillations there is a surplus of the type of c-vertices favoured by the DWBCs. In addition there appear to be weak 'higher-order' oscillations in $c_\pm$-densities, forming various saddle-point-like patterns. The oscillations seem to grow weaker as Δ increases. Nevertheless the oscillations persist well into the D phase, with FE and AF oscillations remaining partially visible at $\Delta = 1/2$ (Fig. 4.11). A more quantitative understanding of these vertex-density oscillations and arrow correlations in the temperate region is desirable, both via simulations and through the analytic methods of Refs. [137, 138], [142], or [123]. In fact, similar finite-size oscillatory behaviour is known to occur for the eigenvalue distributions in random-matrix models[9], see e.g. [154]; this might shed light on the oscillations at least for $\Delta = 0$, cf. [137, 138].

In the near future we plan to report on phase coexistence, arctic-curve phenomena and the structure of the D region for various other choices of boundary conditions; cf. Ref. [148]. Another interesting direction is the study the case of quantum-integrable 'solid-on-solid' (SOS) models, with weights associated to the dynamical Yang–Baxter equation. The trigonometric SOS model is a one-parameter extension of the six-vertex model, and it would be interesting to understand the dependence of those phenomena on the additional 'dynamical' or 'height' parameter. It would also be very exciting if the theoretical and numerical investigations of the F model with domain walls would be complemented by experimental work as in, e.g., Ref. [143].

A Relating configurations with opposite chequerboards in the AF region

In this appendix we show that the F model has symmetries that can be used to sample the whole of phase space starting from any initial configuration obeying the ice rule and DWBCs. We should emphasize that the symmetries we have in mind are symmetries of the model, not of the individual configurations.

We start locally, with the symmetries of the F model at the level of individual vertices shown in Fig. 3.1. Such local symmetries must certainly preserve the lattice near the vertex, i.e. the vertex with its four surrounding edges, so we are led to the dihedral group D_4 of symmetries of the square. Concretely it contains rotations over multiples of $\pi/2$ as well as reflections in the horizontal, vertical and (anti)diagonal line through the vertex. These operations clearly preserve the ice rule. In fact, when the edges carry arrows there is one more thing we can do that is compatible with the ice rule: reversing all arrows, yielding an action of $\mathbb{Z}_2$ that commutes with the D_4.

One can check the preceding operations change the vertex weights as follows:

---

[9] We thank K. Johansson for pointing this out to us.

$$\begin{aligned}
\text{reflect } \updownarrow \ &: \quad a_\pm \leftrightarrow b_\pm \,, \\
\text{reflect } \leftrightarrow \ &: \quad a_\pm \leftrightarrow b_\mp \,, \\
\text{reflect } \neswarrow \ &: \quad a_+ \leftrightarrow a_- \,, \quad c_+ \leftrightarrow c_- \,, \\
\text{reflect } \nwsearrow \ &: \quad b_+ \leftrightarrow b_- \,, \quad c_+ \leftrightarrow c_- \,, \\
\text{rotate } \circlearrowleft \ &: \quad a_\pm \mapsto b_\mp \,, \quad b_\pm \mapsto a_\pm \,, \quad c_+ \leftrightarrow c_- \,, \\
\text{reverse arrows} \ &: \quad a_+ \leftrightarrow a_- \,, \quad b_+ \leftrightarrow b_- \,, \quad c_+ \leftrightarrow c_- \,,
\end{aligned}$$

where for each reflection we omit the two weights it preserves. Notice that, when using arrows along the edges to represent the microscopic degrees of freedom, the F model may be characterized as the special case of the six-vertex model for which the vertex weights are invariant under rotations over $\pi/2$, and that they are then further invariant under all of $D_4 \times \mathbb{Z}_2$.

At the global level $D_4 \times \mathbb{Z}_2$ acts on the configurations, where D_4 acts by symmetries of the $L \times L$ lattice if we would forget about the arrows. Not all of these global maps are allowed, though. Regarding the operations corresponding to D_4 the DWBCs are only preserved by a subgroup isomorphic to $\mathbb{Z}_2 \times \mathbb{Z}_2$ corresponding to rotation over π and reflection in the horizontal and vertical symmetry axes of the lattice. However, that the remaining operations in D_4 also preserve the DWBCs if we combine them with arrow reversal[10].

The next question is how these operations act at the level of configurations. Recall that there are two AF ground states, with opposite chequerboard patterns for the alternating c_+- and c_--vertices constituting the AF region; let us call them '0' and '1'. Below the critical temperature ($\Delta < -1$) any configuration is closer (more similar) to one of these two ground states. Accordingly, the phase space decomposes into two parts, say $\mathcal{C}_i$, with $i \in \mathcal{C}_i$ for $i = 0, 1$. For sufficiently low temperatures (or Δ) and large enough L it costs a macroscopically large amount of energy to go from the energetically favourable part of $\mathcal{C}_0$, i.e. configurations close enough to 0, to the corresponding part of $\mathcal{C}_1$: the system is practically trapped in one of these parts. Since we start our Monte-Carlo algorithm from one of the two AF ground states we thus expect to stay in the corresponding part of the phase space as the system thermalizes for $\Delta < -1$ and large enough L.

---

[10] Thus the full global symmetry group of the F model with DWBCs is a subgroup of $D_4 \times \mathbb{Z}_2$ isomorphic to D_4. Recall that D_4 has a presentation in terms of two generators, r and s, subject to the relations $r^4 = s^2 = (s\,r)^2 = e$. Concretely, r acts by a rotation over $\pi/2$ while s acts by a reflection. Write g^* for the combination of $g \in D_4$ with arrow reversal. Then the subgroup of global symmetries is generated by r^* and s, where the latter acts by reflection in the horizontal or vertical axes; clearly $(r^*)^4 = s^2 = (s\,r^*)^2 = e$. See also (4.18).

Now we return to the model's symmetries. Consider the two AF ground states, 0 and 1. When L is even the four axes of reflection symmetry meet in the middle of the central face of the lattice, and it follows that the model's symmetries fall into two classes:

$$\begin{array}{rl} \text{fixing } i: & \text{identity}, \quad \curvearrowleft, \quad \swarrow\!\!\!\!\nearrow^{*}, \quad \nwarrow\!\!\!\!\searrow^{*}, \\ 0 \leftrightarrow 1: & \circlearrowleft^{*}, \quad \circlearrowright^{*}, \quad \leftrightarrow, \quad \updownarrow, \end{array} \tag{4.18}$$

where '*' means combination with arrow reversal. More generally, (4.18) indicates how the model's global symmetries relate the $\mathcal{G}_i$.

Since for the F model these operations do not change the vertex weights, they preserve the energy of the configurations. Given any configuration we can act by the model's symmetries to generate further configurations of the same energy; we get up to eight configurations in this way, though it may be only four or two if the original configuration happened to possess some amount of symmetry. (One should really check for such symmetries of the original configuration to avoid overcounting, but at high enough L we can skip this step as such symmetric configurations make up a negligible portion of the phase space.) Half of the configurations we get in this way lie in $\mathcal{G}_0$ and the other half in $\mathcal{G}_1$. The upshot is that after having run the Monte Carlo simulation we can use the model's symmetries to sample the full phase space, even from simulations that correctly sample around one of the two ground states.

Outlook

The main focus of this Thesis is the behaviour of two-dimensional materials, namely (anti)-ferromagnetic materials in the first two chapters, which show topological phases, and energetic square ice in the third and fourth chapter. The magnetic materials are of interest in part due to foreseen practical applications in which skyrmions can act as data carriers for which we have shown that skyrmions can exist in the ground state. Energetic square ice is of theoretical interest due to its anomalous behaviour at the infinite-order phase transition and as a purely mathematical analytically solvable model. We used this model to test the order parameter we constructed that, by definition, can be used to detect these infinite-order phase transitions. We also show agreement between conjectured and known properties for energetic square ice with special boundaries and show the existence of oscillations that go beyond current theories.

Further research, however, is necessary in both of these topics. For ferromagnetic systems we developed tools to calculate quantum fluctuations on given configurations. It would be interesting to use these to investigate the changes these fluctuations bring to the classical phase diagram for both the ferromagnetic as well as the anti-ferromagnetic case. As skyrmionic textures are of interest in search for new data transfer methods more research is needed to investigate the behaviour of stable ground state configurations when manipulated by spin and heat currents.

The chapter on energetic ice also brings forth some yet unanswered questions. More numerical investigation into the F-model with even more exotic boundary conditions, which can lead to drastic changes for the phase diagram, can be compared to and used in combination with analytical results. Since the order parameter we constructed should, in principle, work for all infinite-order phase transitions it would be interesting to test our proposed observable for other models that exhibit these types of phase transitions.

References

[1] R. Keesman, A. O. Leonov, P. van Dieten, S. Buhrandt, G. T. Barkema, L. Fritz, and R. A. Duine, *Degeneracies and fluctuations of Néel skyrmions in confined geometries*, Phys. Rev. B **92**, 134405 (2015), arXiv:1506.00271 [cond-mat.mes-hall].

[2] R. Keesman, M. Raaijmakers, A. E. Baerends, G. T. Barkema, and R. A. Duine, *Skyrmions in square-lattice antiferromagnets*, Phys. Rev. B **94**, 054402 (2016), arXiv:1603.03688 [cond-mat.mes-hall].

[3] R. Keesman, J. Lamers, R. A. Duine, and G. T. Barkema, *Finite-size scaling at infinite-order phase transitions*, J. Stat. Mech., 093201 (2016), arXiv:1605.08876 [cond-mat.stat-mech].

[4] R. Keesman and J. Lamers, *Numerical study of the F model with domain-wall boundaries*, Phys. Rev. E **95**, 052117 (2017), arXiv:1702.05474 [cond-mat.stat-mech].

[5] R. Keesman, G. T. Barkema, and D. Panja, *Dynamical eigenmodes of star and tadpole polymers*, J. Stat. Mech., P02021 (2013), arXiv:1210.0774 [cond-mat.soft].

[6] R. Keesman, G. T. Barkema, and D. Panja, *Dynamical eigenmodes of a polymerized membrane*, J. Stat. Mech., P04009 (2013), arXiv:1212.1024 [cond-mat.soft].

[7] Nobelprize.org, *The 2016 Nobel Prize in Physics - Press Release*, (2016).

[8] A. D. McNaught and A. Wilkinson, *Compendium of Chemical Terminology* (Wiley, 1997).

[9] P. Zinn-Justin, *Quantum Field Theory and Critical Phenomena* (Oxford University Press, Oxford, 1989).

[10] V. L. Berezinskiĭ, *Destruction of Long-range Order in One-dimensional and Two-dimensional Systems having a Continuous Symmetry Group I. Classical Systems,* Soviet Journal of Experimental and Theoretical Physics **32**, 493 (1971).

[11] V. L. Berezinskiĭ, *Destruction of Long-range Order in One-dimensional and Two-dimensional Systems Possessing a Continuous Symmetry Group. II. Quantum Systems,* Soviet Journal of Experimental and Theoretical Physics **34**, 610 (1972).

[12] J. M. Kosterlitz and D. J. Thouless, *Ordering, metastability and phase transitions in two-dimensional systems,* Journal of Physics C: Solid State Physics **6**, 1181 (1973).

[13] M. E. J. Newman and G. T. Barkema, *Monte Carlo Methods in Statistical Physics* (Clarendon Press, Oxford, 1999).

[14] E. Marinari and G. Parisi, *Simulated Tempering: A New Monte Carlo Scheme,* Europhys. Lett. **19**, 6 (1992), arXiv:hep-lat/9205018.

[15] J. W. Gibbs, *Elementary Principles in Statistical Mechanics* (Charles Scribner's Sons, New York, 1902).

[16] A Papoulis, *Probability, Random Variables and Stochastic Processes, 2nd ed.* (McGraw-Hill, New York, 1984).

[17] R. Y. Rubinstein and D. P. Kroese, *Simulation and the Monte Carlo Method (Vol. 707)* (John Wiley & Sons, Hoboken, New Jersey, 2011).

[18] M. Michel, S. C. Kapfer, and W. Krauth, *Generalized event-chain Monte Carlo: Constructing rejection-free global-balance algorithms from infinitesimal steps,* The Journal of Chemical Physics **140**, 054116 (2014), 10.1063/1.4863991, arXiv:1309.7748 [cond-mat.stat-mech].

[19] N. Metropolis, A. W. Rosenbluth, M. N. Rosenbluth, A. H. Teller, and E. Teller, *Equation of State Calculations by Fast Computing Machines,* The Journal of Chemical Physics **21**, 1087 (1953).

[20] H. G. Katzgraber and S. Trebst and D. A. Huse and M. Troyer, *Feedback-optimized parallel tempering Monte Carlo,* J. Stat. Mech., P03018 (2006), arXiv:cond-mat/0602085.

[21] A. E. Ferdinand and M. E. Fisher, *Bounded and Inhomogeneous Ising Models. I. Specific-Heat Anomaly of a Finite Lattice,* Phys. Rev. **185**, 832 (1969).

[22] J. P. Valleau and D. N. Card, *Monte Carlo Estimation of the Free Energy by Multistage Sampling,* The Journal of Chemical Physics **57**, 5457 (1972).

[23] A. M. Ferrenberg and R. H. Swendsen, *Optimized Monte Carlo data analysis,* Phys. Rev. Lett. **63**, 1195 (1989).

[24] T. W. B. Kibble, *Topology of cosmic domains and strings,* Journal of Physics A: Mathematical and General **9**, 1387 (1976).

[25] W. H. Zurek, *Cosmological experiments in superfluid helium?* Nature **317**, 505 (1985).

[26] K. Binder, *Finite size scaling analysis of ising model block distribution functions,* Zeitschrift für Physik B Condensed Matter **43**, 119 (1981).

[27] Nobelprize.org, *Pierre Curie - Biographical,* (2016).

[28] I. Dzyaloshinskii, *A thermodynamic theory of "weak" ferromagnetism of antiferromagnetics,* Journal of Physics and Chemistry of Solids **4**, 241 (1958).

[29] T. Moriya, *Anisotropic Superexchange Interaction and Weak Ferromagnetism,* Phys. Rev. **120**, 91 (1960).

[30] J. D. Bernal and R. H. Fowler, *A Theory of Water and Ionic Solution, with Particular Reference to Hydrogen and Hydroxyl Ions,* The Journal of Chemical Physics **1**, 515 (1933).

[31] L. Pauling, *The structure and entropy of ice and of other crystals with some randomness of atomic arrangement,* Journal of the American Chemical Society **57**, 2680 (1935).

[32] G. Algara-Siller, O. Lehtinen, F. C. Wang, R. R. Nair, U. Kaiser, H. A. Wu, A. K. Geim, and I. V. Grigorieva, *Square ice in graphene nanocapillaries,* Nature **519**, 443 (2015), arXiv:1412.7498 [cond-mat.mes-hall].

[33] E. H. Lieb, *Residual Entropy of Square Ice,* Phys. Rev. **162**, 162 (1967).

[34] T.H.R. Skyrme, *A unified field theory of mesons and baryons,* Nuclear Physics **31**, 556 (1962).

[35] S. L. Sondhi, A. Karlhede, S. A. Kivelson, and E. H. Rezayi, *Skyrmions and the crossover from the integer to fractional quantum Hall effect at small Zeeman energies,* Phys. Rev. B **47**, 16419 (1993).

[36] U. A. Khawaja and H. Stoof, *Skyrmions in a ferromagnetic Bose–Einstein condensate,* Nature **411**, 918 (2001).

[37] L. S. Leslie, A. Hansen, K. C. Wright, B. M. Deutsch, and N. P. Bigelow, *Creation and Detection of Skyrmions in a Bose-Einstein Condensate,* Phys. Rev. Lett. **103**, 250401 (2009), ARXIV:0910.4918 [COND-MAT.QUANT-GAS].

[38] A. N. Bogdanov, U. K. Rößler, and A. A. Shestakov, *Skyrmions in nematic liquid crystals,* Phys. Rev. E **67**, 016602 (2003).

[39] P. J. Ackerman, R. P. Trivedi, B. Senyuk, J. van de Lagemaat, and I. I. Smalyukh, *Two-dimensional skyrmions and other solitonic structures in confinement-frustrated chiral nematics,* Phys. Rev. E **90**, 012505 (2014), ARXIV:1612.09015 [COND-MAT.SOFT].

[40] A. O. Leonov, I. E. Dragunov, U. K. Rößler, and A. N. Bogdanov, *Theory of skyrmion states in liquid crystals,* Phys. Rev. E **90**, 042502 (2014), ARXIV:1407.7409 [COND-MAT.MES-HALL].

[41] A. Bogdanov and A. Hubert, *Thermodynamically stable magnetic vortex states in magnetic crystals,* Journal of Magnetism and Magnetic Materials **138**, 255 (1994).

[42] S. Mühlbauer, B. Binz, F. Jonietz, C. Pfleiderer, A. Rosch, A. Neubauer, R. Georgii, and P. Böni, *Skyrmion Lattice in a Chiral Magnet,* Science **323**, 915 (2009), ARXIV:0902.1968 [COND-MAT.STR-EL].

[43] C. Pappas, E. Lelièvre-Berna, P. Falus, P. M. Bentley, E. Moskvin, S. Grigoriev, P. Fouquet, and B. Farago, *Chiral Paramagnetic Skyrmion-like Phase in MnSi,* Phys. Rev. Lett. **102**, 197202 (2009), ARXIV:0902.3603 [COND-MAT.OTHER].

[44] X. Z. Yu, Y. Onose, N. Kanazawa, J. H. Park, J. H. Han, Y. Matsui, N. Nagaosa, and Y. Tokura, *Real-space observation of a two-dimensional skyrmion crystal,* Nature **465**, 901 (2010).

[45] F. Jonietz, S. Mühlbauer, C. Pfleiderer, A. Neubauer, W. Münzer, A. Bauer, T. Adams, R. Georgii, P. Böni, R. A. Duine, K. Everschor, M. Garst, and A. Rosch, *Spin Transfer Torques in MnSi at Ultralow Current Densities,* Science **330**, 1648 (2010), ARXIV:1012.3496 [COND-MAT.STR-EL].

[46] A. Fert, V. Cros, and J. Sampaio, *Skyrmions on the track,* Nature Nanotechnology **8**, 152 (2013).

[47] N. Romming, C. Hanneken, M. Menzel, J. E. Bickel, B. Wolter, K. von Bergmann, A. Kubetzka, and R. Wiesendanger, *Writing and Deleting Single Magnetic Skyrmions,* Science **341**, 636 (2013).

[48] S. Emori, U. Bauer, S.-M. Ahn, E. Martinez, and G. S. D. Beach, *Current-driven dynamics of chiral ferromagnetic domain walls,* Nature Materials **12**, 611 (2013), ARXIV:1302.2257 [COND-MAT.MTRL-SCI].

[49] K.-S. Ryu, L. Thomas, S.-H. Yang, and S. Parkin, *Chiral spin torque at magnetic domain walls,* Nanotechnology **8**, 527 (2013).

[50] K.-S. Ryu, S.-H. Yang, L. Thomas, and S. Parkin, *Chiral spin torque arising from proximity-induced magnetization,* Nature Communications **5**, 3910 (2014).

[51] J. H. Franken, M. Herps, H. J. M. Swagten, and B. Koopmans, *Tunable chiral spin texture in magnetic domain-walls,* Scientific Reports **4**, 5248 (2014), ARXIV:1404.2945 [COND-MAT.MES-HALL].

[52] S.-G. Je, D.-H. Kim, S.-C. Yoo, B.-C. Min, K.-J. Lee, and S.-B. Choe, *Asymmetric magnetic domain-wall motion by the Dzyaloshinskii-Moriya interaction,* Phys. Rev. B **88**, 214401 (2013), ARXIV:1307.0984 [COND-MAT.MTRL-SCI].

[53] A. Hrabec, N. A. Porter, A. Wells, M. J. Benitez, G. Burnell, S. McVitie, D. McGrouther, T. A. Moore, and C. H. Marrows, *Measuring and tailoring the Dzyaloshinskii-Moriya interaction in perpendicularly magnetized thin films,* Phys. Rev. B **90**, 020402 (2014), ARXIV:1402.5410 [COND-MAT.MTRL-SCI].

[54] G. Chen, T. Ma, A. T. N'Diaye, H. Kwon, C. Won, Y. Wu, and A. K. Schmid, *Tailoring the chirality of magnetic domain walls by interface engineering,* Nature Communications **4**, 2671 (2013).

[55] S. Heinze, K. von Bergmann, M. Menzel, J. Brede, A. Kubetzka, R. Wiesendanger, G. Bihlmayer, and S. Blügel, *Spontaneous atomic-scale magnetic skyrmion lattice in two dimensions,* Nature Physics **7**, 713 (2011).

[56] I. Kézsmárki, S. Bordács, P. Milde, E. Neuber, L. M. Eng, J. S. White, H. M. Ronnow, C. D. Dewhurst, M. Mochizuki, K. Yanai, H. Nakamura, D. Ehlers, V. Tsurkan, and A. Loidl, *Néèl-type skyrmion lattice with confined orientation in the polar magnetic semiconductor* GaV_4S_8, Nat Mater **14**, 1116 (2015), ARXIV:1502.08049 [COND-MAT.MTRL-SCI].

[57] S. Banerjee, J. Rowland, O. Erten, and M. Randeria, *Enhanced Stability of Skyrmions in Two-Dimensional Chiral Magnets with Rashba Spin-Orbit Coupling,* Phys. Rev. X **4**, 031045 (2014).

[58] S. Buhrandt and L. Fritz, *Skyrmion lattice phase in three-dimensional chiral magnets from Monte Carlo simulations,* Phys. Rev. B **88**, 195137 (2013), ARXIV:1304.6580 [COND-MAT.STR-EL].

[59] S. D. Yi, S. Onoda, N. Nagaosa, and J. H. Han, *Skyrmions and anomalous Hall effect in a Dzyaloshinskii-Moriya spiral magnet,* Phys. Rev. B **80**, 054416 (2009), ARXIV:0903.3272 [COND-MAT.STR-EL].

[60] M. N. Wilson, A. B. Butenko, A. N. Bogdanov, and T. L. Monchesky, *Chiral skyrmions in cubic helimagnet films: The role of uniaxial anisotropy,* Phys. Rev. B **89**, 094411 (2014), ARXIV:1311.1191 [COND-MAT.MES-HALL].

[61] S. X. Huang and C. L. Chien, *Extended Skyrmion Phase in Epitaxial* FeGe(111) *Thin Films,* Phys. Rev. Lett. **108**, 267201 (2012).

[62] M. N. Wilson, E. A. Karhu, A. S. Quigley, U. K. Rößler, A. B. Butenko, A. N. Bogdanov, M. D. Robertson, and T. L. Monchesky, *Extended elliptic skyrmion gratings in epitaxial MnSi thin films,* Phys. Rev. B **86**, 144420 (2012).

[63] M. N. Wilson, E. A. Karhu, D. P. Lake, A. S. Quigley, S. Meynell, A. N. Bogdanov, H. Fritzsche, U. K. Rößler, and T. L. Monchesky, *Discrete helicoidal states in chiral magnetic thin films,* Phys. Rev. B **88**, 214420 (2013), ARXIV:1305.5196 [COND-MAT.MES-HALL].

[64] H. Du, D. Liang, C. Jin, L. Kong, M. J. Stolt, W. Ning, J. Yang, Y. Xing, J. Wang, R. Che, J. Zang, S. Jin, Y. Zhang, and M. Tian, *Electrical probing of field-driven cascading quantized transitions of skyrmion cluster states in MnSi nanowires,* Nat Commun **6**, 7637 (2015), ARXIV:1504.04918 [COND-MAT.MES-HALL].

[65] H. Du, R. Che, L. Kong, X. Zhao, C. Jin, C. Wang, J. Yang, W. Ning, R. Li, C. Jin, X. Chen, J. Zang, Y. Zhang, and M. Tian, *Edge-mediated skyrmion chain and its collective dynamics in a confined geometry,* Nat Commun **6**, 8504 (2015), ARXIV:1505.04932 [COND-MAT.MES-HALL].

[66] N. Romming, A. Kubetzka, C. Hanneken, K. von Bergmann, and R. Wiesendanger, *Field-Dependent Size and Shape of Single Magnetic Skyrmions,* Phys. Rev. Lett. **114**, 177203 (2015), ARXIV:1504.01573 [COND-MAT.MES-HALL].

[67] M. Beg, R. Carey, W. Wang, D. Cortés-Ortuño, M. Vousden, M.-A. Bisotti, M. Albert, D. Chernyshenko, O. Hovorka, R. L. Stamps, and H. Fangohr, *Ground state search, hysteretic behaviour, and reversal mechanism of skyrmionic textures in confined helimagnetic nanostructures,* Scientific Reports **5**, 17137 (2015), ARXIV:1312.7665 [COND-MAT.MTRL-SCI].

[68] R. E. Troncoso and Á. S. Núñez, *Thermally assisted current-driven skyrmion motion,* Phys. Rev. B **89**, 224403 (2014), ARXIV:1402.1501 [COND-MAT.MES-HALL].

[69] S. Rohart and A. Thiaville, *Skyrmion confinement in ultrathin film nanostructures in the presence of Dzyaloshinskii-Moriya interaction,* Phys. Rev. B **88**, 184422 (2013), ARXIV:1310.0666 [COND-MAT.MES-HALL].

[70] A. O. Leonov, (2011).

[71] S. A. Meynell, M. N. Wilson, H. Fritzsche, A. N. Bogdanov, and T. L. Monchesky, *Surface twist instabilities and skyrmion*

states in chiral ferromagnets, Phys. Rev. B **90**, 014406 (2014), arXiv:1405.5275 [cond-mat.mes-hall].

[72] A. Roldán-Molina, M. J. Santander, Á. S. Núñez, and J. Fernández-Rossier, *Quantum theory of spin waves in finite chiral spin chains,* Phys. Rev. B **89**, 054403 (2014), arXiv:1311.2695 [cond-mat.mes-hall].

[73] A. Roldán-Molina, M. J. Santander, Á. S. Núñez, and J. Fernández-Rossier, *Quantum fluctuations stabilize skyrmion textures,* Phys. Rev. B **92**, 245436 (2015), arXiv:1502.01950 [cond-mat.mes-hall].

[74] N. Kanazawa, M. Kubota, A. Tsukazaki, Y. Kozuka, K. S. Takahashi, M. Kawasaki, M. Ichikawa, F. Kagawa, and Y. Tokura, *Discretized topological Hall effect emerging from skyrmions in constricted geometry,* Phys. Rev. B **91**, 041122 (2015), arXiv:1501.03290 [cond-mat.str-el].

[75] M. Lee, W. Kang, Y. Onose, Y. Tokura, and N. P. Ong, *Unusual Hall Effect Anomaly in MnSi under Pressure,* Phys. Rev. Lett. **102**, 186601 (2009), arXiv:0811.3146 [cond-mat.str-el].

[76] A. Neubauer, C. Pfleiderer, B. Binz, A. Rosch, R. Ritz, P. G. Niklowitz, and P. Böni, *Topological Hall Effect in the A Phase of MnSi,* Phys. Rev. Lett. **102**, 186602 (2009), arXiv:0902.1933 [cond-mat.str-el].

[77] M. E. Knoester, J. Sinova, and R. A. Duine, *Phenomenology of current-skyrmion interactions in thin films with perpendicular magnetic anisotropy,* Phys. Rev. B **89**, 064425 (2014), arXiv:1310.2850 [cond-mat.mes-hall].

[78] C. Moreau-Luchaire, C. Moutafis, N. Reyren, J. Sampaio, F. Vaz, C. A., N. Van Horne, K. Bouzehouane, K. Garcia, C. Deranlot, P. Warnicke, P. Wohlhüter, J.-M. George, M. Weigand, J. Raabe, V. Cros, and A. Fert, *Additive interfacial chiral interaction in multilayers for stabilization of small individual skyrmions at room temperature,* Nat Nano **11**, 444 (2016), arXiv:1607.02958 [cond-mat.mtrl-sci].

[79] J. Iwasaki, M. Mochizuki, and N. Nagaosa, *Current-induced skyrmion dynamics in constricted geometries,* Nat Nano **8**, 742 (2013), arXiv:1310.1655 [cond-mat.mes-hall].

[80] J. Iwasaki, M. Mochizuki, and N. Nagaosa, *Universal current-velocity relation of skyrmion motion in chiral magnets,* Nat Commun **4**, 1463 (2013), arXiv:1207.3224 [cond-mat.str-el].

[81] I. Raičević, Dragana Popović, C. Panagopoulos, L. Benfatto, M. B. Silva Neto, E. S. Choi, and T. Sasagawa, *Skyrmions in a Doped Antiferromagnet,* Phys. Rev. Lett. **106**, 227206 (2011), arXiv:1006.1891 [cond-mat.str-el].

[82] T. Ollikainen, E. Ruokokoski, and M. Möttönen, *Creation and dynamics of two-dimensional skyrmions in antiferromagnetic spin-1 Bose-Einstein condensates,* Phys. Rev. A **89**, 033629 (2014), arXiv:1310.0269 [cond-mat.quant-gas].

[83] T. Okubo, S. Chung, and H. Kawamura, *Multiple-q States and the Skyrmion Lattice of the Triangular-Lattice Heisenberg Antiferromagnet under Magnetic Fields,* Phys. Rev. Lett. **108**, 017206 (2012), arXiv:1109.6161 [cond-mat.stat-mech].

[84] H. D. Rosales, D. C. Cabra, and P. Pujol, *Three-sublattice skyrmion crystal in the antiferromagnetic triangular lattice,* Phys. Rev. B **92**, 214439 (2015), arXiv:1507.05109 [cond-mat.str-el].

[85] Z. Liu and H. Ian, *Numerical studies on antiferromagnetic skyrmions in nanodisks by means of a new quantum simulation approach,* Chemical Physics Letters **649**, 135 (2016), arXiv:1601.05170 [cond-mat.mes-hall].

[86] A. N. Bogdanov, U. K. Rößler, M. Wolf, and K.-H. Müller, *Magnetic structures and reorientation transitions in noncentrosymmetric uniaxial antiferromagnets,* Phys. Rev. B **66**, 214410 (2002), arXiv:cond-mat/0206291.

[87] A. Bogdanov and A. Shestakov, *Vortex states in antiferromagnetic crystals,* Physics of the Solid State **40**, 1350 (1998).

[88] J. Barker and O. A. Tretiakov, *Static and Dynamical Properties of Antiferromagnetic Skyrmions in the Presence of Applied Current and Temperature,* Phys. Rev. Lett. **116**, 147203 (2016), arXiv:1505.06156 [cond-mat.mes-hall].

[89] X. Zhang, Y. Zhou, and M. Ezawa, *Antiferromagnetic Skyrmion: Stability, Creation and Manipulation,* Scientific Reports **6**, 24795 (2016), arXiv:1504.01198 [cond-mat.mes-hall].

[90] H. Velkov, O. Gomonay, M. Beens, G. Schwiete, A. Brataas, J. Sinova, and R. A. Duine, *Phenomenology of current-induced skyrmion motion in antiferromagnets,* New J. Phys. **18**, 075016 (2016), arXiv:1604.05712 [cond-mat.mes-hall].

[91] E. M. Lifshitz and Pitaevskii L. P., *Statistical Physics, Part 2, Course of Theoretical Physics Vol. 9* (Pergamon, Oxford, 1980).

[92] P. Minnhagen, *The two-dimensional coulomb gas, vortex unbinding, and superfluid-superconducting films,* Rev. Mod. Phys **59**, 1001 (1987).

[93] R. J. Baxter, *Exactly Solved Models in Statistical Mechanics* (Dover Publications, New York, 2007).

[94] M. N. Barber, *Phase transitions and critical phenomena,* (Academic Press, 1983) Chap. Finite-size scaling, p. 146.

[95] Y.-D. Hsieh, Y.-J. Kao, and A. W. Sandvik, *Finite-size scaling method for the Berezinskiĭ–Kosterlitz–Thouless transition,* J. Stat. Mech., P09001 (2013), arXiv:1302.2900 [cond-mat.stat-mech].

[96] C. J. Hamer and M. N. Barber, *Finite-size scaling in Hamiltonian field theory,* J. Phys. A: Math. Gen. **13**, L169 (1980).

[97] C. J. Hamer and M. N. Barber, *Finite-lattice methods in quantum Hamiltonian field theory: II. O(2) and O(3) Heisenberg models,* J. Phys. A: Math. Gen. **14**, 259 (1981).

[98] R. Kenna, *The XY model and the Berezinskiĭ–Kosterlitz–Thouless phase transition,* Ann. MCFA **IV**, phy4 (2005), arXiv:cond-mat/0512356.

[99] R. H. Swendsen, *Monte Carlo studies of the interface roughening transition,* Phys. Rev. B **15**, 5421 (1977).

[100] H. Hu, Y. Deng, and H. W. J. Blöte, *Berezinskiĭ-Kosterlitz-Thouless-like percolation transitions in the two-dimensional XY model,* Phys. Rev. E **83**, 011124 (2011), arXiv:1010.3075 [cond-mat.stat-mech].

[101] H. W. J. Blöte and M. P. Nightingale, *Antiferromagnetic triangular Ising model: Critical behavior of the ground state,* Phys. Rev. B **47**, 15046 (1993).

[102] G. Mazzeo, G. Jug, A. C. Levi, and E. Tosatti, *Sublattice order parameter in the BCSOS model: a finite-size Monte Carlo study,* J. Phys. A: Math. Gen. **25**, L967 (1992).

[103] M. Weigel and W. Janke, *The square-lattice F model revisited: a loop-cluster update scaling study,* J.Phys. A **38**, 7067 (2005), ARXIV:COND-MAT/0501222.

[104] E. H. Lieb, *Exact solution of the F-model of an antiferroelectric,* Phys. Rev. Lett. **18**, 1046 (1967).

[105] H. van Beijeren, *Exactly solvable model for the roughening transition of a crystal surface,* Phys. Rev. Lett. **38**, 993 (1977).

[106] Bernard Nienhuis, *Critical behavior of two-dimensional spin models and charge asymmetry in the Coulomb gas,* J. Stat. Phys. **34**, 731 (1984).

[107] R. Savit, *Duality in field theory and statistical systems,* Rev. Mod. Phys **52**, 453 (1980).

[108] R. J. Baxter, *Spontaneous staggered polarization of the F-model,* J. Stat. Phys. **9**, 145 (1973).

[109] R. J. Baxter, *Spontaneous staggered polarization of the F-model,* J. Phys. C: Solid State Phys. **6**, L94 (1973).

[110] F. Rys, *Über ein zweidimensionales klassisches Konfigurationsmodell,* Helv. Phys. Acta **36**, 537 (1963).

[111] V. Korepin and P. Zinn-Justin, *Thermodynamic limit of the six-vertex model with domain wall boundary conditions,* J. Phys. A: Math. Gen. **33**, 7053 (2000), ARXIV:COND-MAT/0004250.

[112] P. Zinn-Justin, *The Influence of Boundary Conditions in the Six-Vertex Model,* (2002), ARXIV:COND-MAT/0205192.

[113] D. Allison and N. Reshetikhin, *Numerical study of the 6-vertex model with domain wall boundary conditions,* Ann. Inst. Fourier (Grenoble) **55**, 1847 (2005), arXiv:cond-mat/0502314.

[114] T. S. Tavares, G. A. P. Ribeiro, and V. E. Korepin, *The entropy of the six-vertex model with variety of different boundary conditions,* J. Stat. Mech., P06016 (2015), arXiv:1501.02818 [cond-mat.stat-mech].

[115] T. S. Tavares, G. A. P. Ribeiro, and V. E. Korepin, *Influence of boundary conditions on bulk properties of six-vertex model,* J. Phys. A: Math. Theor. **48**, 454004 (2015), arXiv:1509.06324 [cond-mat.stat-mech].

[116] H. J. Brascamp, H. Kunz, and F. Y. Wu, *Some rigorous results for the vertex model in statistical mechanics,* J. Math. Phys. **14**, 1927 (1973).

[117] J. Lamers, *A pedagogical introduction to quantum integrability, with a view towards theoretical high-energy physics,* PoS **Modave2014**, 001 (2014), arXiv:1501.06805 [math-ph].

[118] S. K. Jain, V. Juričić, and G. T. Barkema, *Boundaries determine the formation energies of lattice defects in two-dimensional buckled materials,* Phys. Rev. B **94**, 020102 (2016), arXiv:1607.03638 [cond-mat.mtrl-sci].

[119] V. E. Korepin, *Calculation of norms of bethe wave functions,* Commun. Math. Phys. **86**, 391 (1982).

[120] W. H. Mills, D. P. Robbins, and H. Rumsey, *Alternating sign matrices and descending plane partitions,* J. Combin. Theory Ser. A **34**, 340 (1983).

[121] G. Kuperberg, *Another proof of the alternating sign matrix conjecture,* Inter. Math. Res. Notes **1996**, 139 (1996), arXiv:math/9712207 [math.CO].

[122] D. Bressoud, *Proofs and Confirmations: The Story of the Alternating Sign Matrix Conjecture* (Cambridge University Press, Cambridge, 1999).

[123] N. Allegra, J. Dubail, J.-M. Stéphan, and J. Viti, *Inhomogeneous field theory inside the arctic circle,* J. Stat. Mech.: Theor. Exp., 053108 (2016), arXiv:1512.02872 [cond-mat.stat-mech].

[124] I. Kostov, *Three-point function of semiclassical states at weak coupling,* J. Phys. A: Math. Theor. **45**, 494018 (2012), arXiv:1205.4412 [hep-th].

[125] Y. Jiang, S. Komatsu, I. Kostov, and D. Serban, *Clustering and the three-point function,* J.Phys. A: Math. Theor. **49**, 454003 (2016), arXiv:1604.03575 [hep-th].

[126] A. G. Izergin, *Partition function of the six-vertex model in finite volume,* Sov. Phys. Dokl. **32**, 878 (1987).

[127] A. G. Izergin, D. A. Coker, and V. E. Korepin, *Determinant formula for the six-vertex model,* J. Phys. A: Math. Gen. **25**, 4315 (1992).

[128] P. Zinn-Justin, *Six-vertex model with domain wall boundary conditions and one-matrix model,* Phys. Rev. E **62**, 3411 (2000), arXiv:math-ph/0005008.

[129] P. Bleher and V. Fokin, *Exact solution of the six-vertex model with domain wall boundary conditions. disordered phase,* Commun. Math. Phys. **268**, 223 (2006), arXiv:math-ph/0510033.

[130] P. Bleher and K. Liechty, *Exact solution of the six-vertex model with domain wall boundary conditions. antiferroelectric phase,* Commun. Math. Phys. **286**, 777 (2009), arXiv:0904.3088 [math-ph].

[131] P. Bleher and T. Bothner, *Exact solution of the six-vertex model with domain wall boundary conditions. critical line between disordered and antiferroelectric phases,* Random Matrices: Theory Appl. **01**, 1250012 (2012), arXiv:1208.6276 [math-ph].

[132] P. Bleher and K. Liechty, *Random Matrices and the Six-Vertex Model* (AMS, Providence, RI, 2013).

[133] O. F. Syljuåsen and M. B. Zvonarev, *Directed-loop monte carlo simulations of vertex models,* Phys. Rev. E **70**, 016118 (2004), arXiv:cond-mat/0401491.

[134] L. F. Cugliandolo, G. Gonnella, and A. Pelizzola, *Six-vertex model with domain wall boundary conditions in the Bethe-Peierls approximation,* J. Stat. Mech.: Theor. Exp., 06008 (2015), arXiv:1501.00883 [cond-mat.stat-mech].

[135] I. Lyberg, V. Korepin, and J. Viti, *The density profile of the six vertex model with domain wall boundary conditions,* (2016), arXiv:1612.06758 [cond-mat.stat-mech].

[136] W. Jockusch, J. Propp, and P. Shor, *Random domino tilings and the arctic circle theorem,* (1998), arXiv:math/9801068.

[137] K. Johansson, *The arctic circle boundary and the airy process,* Ann. Prob. **33**, 1 (2005), arXiv:math/0306216.

[138] P. L. Ferrari and H. Spohn, *Domino tilings and the six-vertex model at its free fermion point,* J. Phys. A: Math. Gen. **39**, 10297 (2006), arXiv:cond-mat/0605406.

[139] F. Colomo and A. G. Pronko, *The limit shape of large alternating sign matrices,* SIAM J. Discrete Math. **24**, 1558 (2010), arXiv:0803.2697 [math-ph].

[140] F. Colomo and A. G. Pronko, *The arctic curve of the domain-wall six-vertex model,* J. Stat. Phys. **138**, 662 (2010), arXiv:0907.1264 [math-ph].

[141] F. Colomo, A. G. Pronko, and P. Zinn-Justin, *The arctic curve of the domain-wall six-vertex model in its anti-ferroelectric regime,* J. Stat. Mech.: Theor. Exp., L03002 (2010), arXiv:1001.2189 [math-ph].

[142] F. Colomo and A. G. Pronko, *Thermodynamics of the Six-Vertex Model in an L-Shaped Domain,* Commun. Math. Phys. **339**, 699 (2015), arXiv:1501.03135 [math-ph].

[143] C. Nisoli, R. Moessner, and P. Schiffer, *Colloquium: Artificial spin ice: Designing and imaging magnetic frustration,* Rev. Mod. Phys. **85**, 1473 (2013), arXiv:1306.0825 [cond-mat.mes-hall].

[144] E. H. Lieb and F. Y. Wu, *Phase Transitions and Critical Phenomena,* (Academic Press, London, 1972) Chap. Two-dimensional Ferroelectric Models.

[145] E. H. Lieb, *Exact solution of the two-dimensional slater* KDP *model of a ferroelectric,* Phys. Rev. Lett. **19**, 108 (1967).

[146] P. Bleher and K. Liechty, *Exact solution of the six-vertex model with domain wall boundary conditions. critical line between ferroelectric and disordered phases,* J. Stat. Phys. **134**, 463 (2009), arXiv:0802.0690 [math-ph].

[147] K. Eloranta, *Diamond ice,* J. Stat. Phys. **96**, 1091 (1999).

[148] G. Kuperberg, *Symmetry classes of alternating-sign matrices under one roof,* Ann. of Math. **156**, 835 (2002), arXiv:math/0008184.

[149] J. M. Maillet and J. Sanchez de Santos, *Drinfel'd twists and algebraic Bethe ansatz,* in *L. D. Faddeev's Seminar on Mathematical Physics*, Translations Series 2, Vol. 201, edited by M. Semenov-Tian-Shansky (AMS, Providence, RI, 2000) arXiv:q-alg/9612012.

[150] J. G. Propp and D. B. Wilson, *Exact sampling with coupled markov chains and applications to statistical mechanics,* Random Struct. Algor. **9**, 223 (1996).

[151] J. Propp and D. Wilson, *Coupling from the past: a user's guide,* in *Microsurveys in Discrete Probability*, Discrete Math. Theoret. Comput. Sci., Vol. 41, edited by D. Aldous and J. Propp (AMS, Providence, RI, 1998) pp. 181–192.

[152] J.-S. Wang, R. H. Swendsen, and R. Kotecký, *Three-state antiferromagnetic potts models: A monte carlo study,* Phys. Rev. B **42**, 2465 (1990).

[153] G. T. Barkema and M. E. J. Newman, *Monte carlo simulation of ice models,* Phys. Rev. E **57**, 1155 (1998), arXiv:cond-mat/9706190.

[154] A. Edelman and M. La Croix, *The Singular Values of the GUE (Less is More),* Random Matrices: Theory Appl. **04**, 1550021 (2015), arXiv:1410.7065 [math.PR].

Samenvatting

Omdat niet iedereen zich innig vertrouwd voelt met natuurkunde volgt hier een samenvatting in het Nederlands. Deze samenvatting is gericht op familie, vrienden, en (andere) leken die graag willen weten waar mijn focus lag de laatste jaren, zonder dat zijzelf al te diep in de stof hoeven te duiken.

Aan de hand van de titel van dit proefschrift, *Topologische Fasen en Faseovergangen in Magneten en IJs*, hoop ik duidelijk te maken hoe de verschillende hoofstukken aan elkaar gerelateerd zijn. Daarvoor behandelen we eerst in zijn algemeenheid topologische fasen en faseovergangen om vervolgens inhoudelijk te gaan kijken naar zowel magneten als ijs. Voor deze twee systemen, magneten en ijs, richten we ons eerst op de motivatie om hier onderzoek naar te doen waarna een samenvatting volgt van de bijdrage van deze Thesis aan deze onderzoeksgebieden.

Topologische fasen en faseovergangen

In de natuurkunde wordt het deel van de wereld dat beschreven wordt altijd het systeem genoemd. Alles buiten dit systeem wordt buiten beschouwing gelaten. Als in het systeem een substantie is met een bepaalde eigenschap, dan kan hier vaak een fase aan worden toegeschreven. De fase van een stof beschrijft welke eigenschappen de stof heeft. Denk bijvoorbeeld aan een systeem waarin een pan met water in een ruimte met lucht wordt verhit. De pan, het water, en de lucht zijn in verschillende fasen (vast, vloeibaar, en gasvorming). Hoewel de fase enkele eigenschappen vastlegt van de stof is er nog wel enige vrijheid. Zo kan de temperatuur van het vloeibare water onder normale omstandigheden tussen de $0°C$ en $100°C$ liggen. Wanneer genoeg energie wordt toegevoegd aan het water begint het water te koken. Dit is het proces waarbij vloeibaar water onder verwarming wordt omgezet in waterdamp. De fase van het water is veranderd van vloeibaar naar gasvorming en dit proces vindt plaats op de faseovergang.

Naast verscheidene eigenschappen kan een fase ook topologisch niet-triviaal zijn. Een dergelijke fase wordt ook wel een topologische fase genoemd. Aan een topologische fase kan een beschermd geheel getal worden toegekend. Dit getal, zoals het aantal gaten in een object, is beschermd in de zin dat het niet kan worden veranderd zonder een extreme transformatie, zoals het prikken van een gat, toe te brengen aan het systeem. Een niet-extreme transformatie, zoals de buiging of uitrekking van een object, laat dit getal onveranderd. Het verschil tussen deze types van transformaties is dat de niet-extreme transformatie steeds kleiner gemaakt kan worden terwijl dat niet geldt voor extreme transformaties zoals het maken van een gat. Er kan immers geen half gat gemaakt worden. Dit is het type topologische fasen dat vaak genoemd wordt omdat het tot de verbeelding spreekt. De topologische fasen zoals behandeld in deze Thesis daarentegen gaan meer over topologische texturen op een materiaal waarover hieronder meer volgt. Topologische faseovergangen is een ietwat vaag begript dat slaat op faseovergangen tussen fasen waarvan er minstens één topologisch is of waarbij topologische objecten een relevante rol spelen. Recentelijk (okt 2016) hebben David Thouless, Duncan Haldane, en Michael Kosterlitz de Nobelprijs voor Natuurkunde ontvangen *voor theoretische ontdekkingen van topologische faseovergangen en topologische fasen van materie* [7].

Magneten

Magnetische materialen zijn al bekend sinds de oudheid maar pas na de middeleeuwen zijn er theorieën ontwikkeld die hebben geleid tot onze huidige kennis omtrend magnetisch gedrag. Praktisch gezien zijn magneten overal om ons heen; van de koelkast magneet tot mobieltjes. Magneten zijn belangrijk voor elektronica omdat deze interageren met elektrische stromen. Dit stelt ons er toe in staat om magneten te beïnvloeden en af te tasten met behulp van stroom wat uiteindelijk heeft geleid tot apparaten zoals de magnetische harde schijf.

Om magneten te kunnen begrijpen moeten we onderzoeken wat er gebeurt op microscopisch niveau. Met het Stern–Gerlach experiment is aangetoond dat sommige ongeladen deeltjes, zoals zilver atomen, in een niet-uniform magnetisch veld afgebogen kunnen worden (in verschillende richtingen). Hieruit moet geconcludeerd worden dat sommige elementaire deeltjes een eigenschap, *spin*, moeten hebben die bepaald hoe deze deeltjes beïnvloedt worden door magnetische velden. De spin van een elementair deeltje is een vector; het heeft een grootte en een richting en kan dus worden weergegeven met een pijl. Hoewel kwantummechanisch gezien de spin gekwantiseerd is, dat wil zeggen, gelimiteerd in het aantal toegestane richtingen, mogen we (in de klassieke limiet) aannemen dat deze vrij kan draaien in de ruimte.

Ampère's wet, voor het eerst bewezen door Maxwell, laat zien dat bewegende elektrische lading (stroom) een magnetisch veld opwekt. Omgekeerd geldt dat een magnetisch veld geladen deeltjes in beweging kan zetten. Volgens Ampère's wet kunnen we de spin van een elementair deeltje, sterk gerelateerd aan het intrinsiek magnetisch moment, opvatten als een soort instrinsieke elektrische stroom die behouden is in grootte. Anderzijds kan het ook worden opgevat als een magnetische dipool; een oneindig kleine magneet met een noord- en zuidpool. In Figuur 5.1 worden de opgewekte magneetvelden van een stroomkring, een magneet, en een elementair deeltje met spin met elkaar vergeleken. De magneetvelden van een oneindig kleine stroomkring en een oneindig kleine magneet zijn equivalent aan die van de magnetische dipool.

Een deeltje met spin zal enerzijds een magnetisch veld opwekken en anderzijds beïnvloed worden door externe magnetische velden. Door de zogeheten (puur kwantummechanische) Heisenberg interactie is het voor naburige deeltjes in (anti)ferromagneten energetisch voordelig om de spins (anti)parallel te ordenen waardoor in het geval van de ferromagneet een macroscopisch magnetisch veld opgewekt wordt. De configuratie van de spins in een materiaal kan worden beïnvloed door temperatuur, externe magnetische velden, en stromen zonder dat de atomen daarbij van hun vaste plek in het rooster komen.

Deze mogelijke spin texturen wordt vergroot door meer exotische magneten te bekijken zoals in de eerste twee hoofdstukken van dit werk. Hierbij worden naast de Heisenberg interactie, die zorgt voor de (anti)parallelle ordening, ook nog andere type interacties meegenomen. Zo kunnen lagen van verschillende typen materialen een zogenaamde Dzyaloshinskii-Moriya interactie (DMI) bewerkstelligen waarbij naburige spins onder een hoek ten opzichte van elkaar gedraaid willen zijn. Ook kan er anisotropie optreden waarbij spins uit het vlak, of juist in het vlak, de energie verlagen. Typische magneten, zoals ook hier behandeld, proberen de spins ook langs een aangelegd extern magnetisch veld te richten. Al deze interacties bij elkaar zorgen voor een verscheidenheid aan mogelijke grondtoestanden, configuraties met minimale energie, afhankelijk van de parameter waarden.

De spin texturen waar in dit werk de focus op ligt zijn degenen met skyrmionen. Skyrmionen zijn topologische objecten, of lokale spin configuraties, die

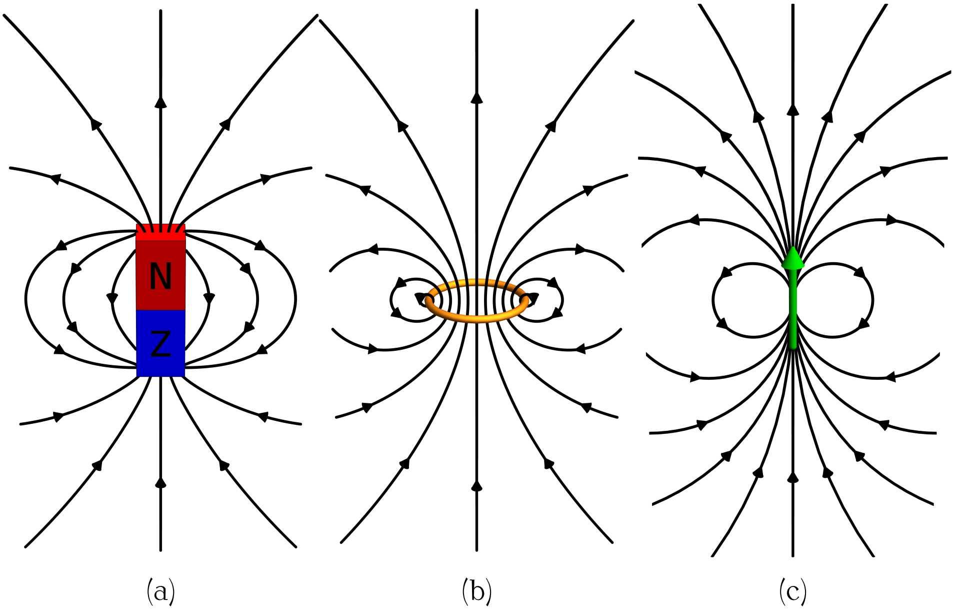

Figuur 5.1. Magneetvelden voor een magneet (a), een stroomkring (b), en een elementair deeltje met spin (c). De magneetveldlijnen zijn weergegeven door de zwarte lijnen waarbij de pijl de richting van het veld weergeeft. Een elementair deeltje met spin (c) gedraagt zich als een magnetische dipool. De velden lijken vooral op grote afstand van de objecten op elkaar omdat oneindig kleine stroomkringen en oneindig kleine magneten equivalent zijn aan magnetische dipolen.

zich in een zee van spins kunnen bevinden (zie Figuur 5.2). Deze zijn topologisch beschermd en zijn dus in grote mate robuust tegen externe fluctuaties door onder andere de temperatuur.

In het eerste hoofdstuk van deze Thesis onderzoeken we de robuustheid van skyrmionen in ferromagnetische systemen van (on)-eindige grootte wanneer deze onderhevig zijn aan opwarming. Hiervoor is gebruikt gemaakt van computer simulaties die de spins in magnetische systemen nabootsen waarna uit de typische configuraties die gerealiseerd worden relevante informatie gehaald kan worden. Ook laten we zien dat skyrmionen kunnen voorkomen in microscopische draden wat voordelig is wanneer deze daadwerkelijk ingezet moeten worden in elektronische apparaten. De simulaties zijn gebaseerd op een klassiek model en daarom bekijken we ook de invloeden van kwantum

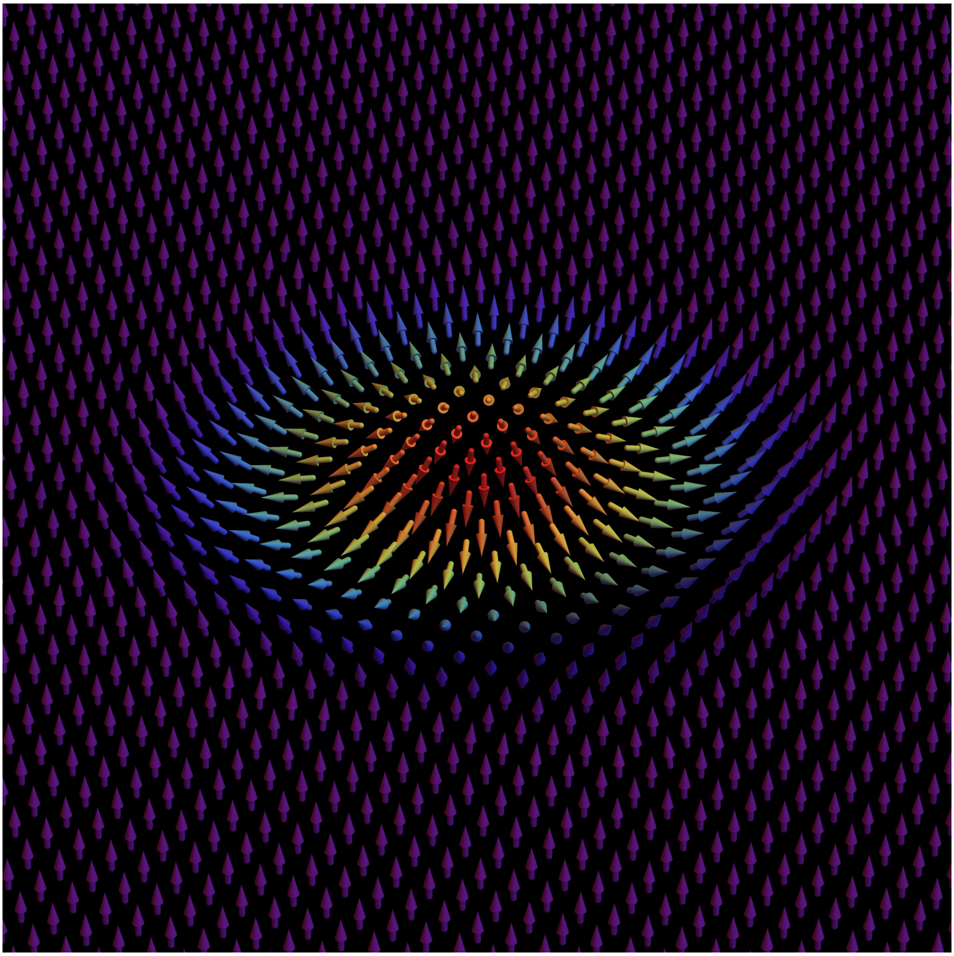

Figuur 5.2. Eén skyrmion in een zee van parallel gerichte spins. Elk pijltje representeert de grootte en richting van de spin van een deeltje. De kleur geeft aan of de spin naar beneden (rood) of omhoog (paars) is gericht. Het skyrmion is een topologisch object dat zich duidelijk onderscheidt van de omliggende homogene spin structuur.

fluctuaties die berekend kunnen worden aan de hand van de klassieke spin configuraties.

In het tweede hoofdstuk onderzoeken we anti-ferromagnetische systemen met computer simulaties en we onderbouwen de resultaten met enkele analytische berekeningen. Voor deze materialen vinden we de globaal anti-ferromagnetische fase, de spiraal fase, en een nieuwe skyrmionische fase die enkele eigenschappen deelt met de skyrmionische fase in de ferromagneet. Ook voor dit materiaal construeren we een fasediagram als functie van enkele materiaaleigenschappen. Daarnaast laten we zien dat een enkel skyrmion ook in een anti-ferromagneet gestabiliseerd kan worden in een microscopisch klein vlak wanneer de temperatuur laag genoeg is.

IJs

Net als magneten speelt ijs ook een belangrijke rol in ons leven ook al is het minder voor de hand liggend dan bij magneten. Water heeft de eigenaardige eigenschap dat ijs, de normale variant die wij kennen, een lagere dichtheid heeft dan vloeibaar water waardoor ijs blijft drijven. Dit is van invloed voor de warmte van de aarde die getemperd blijft door grote ijsvlakten die, doordat deze aan de oppervlakte liggen, grote hoeveelheden zonlicht kunnen weerkaatsen. Naast ‘normaal’ ijs zijn er nog veel meer soorten ijs. Afhankelijk van de druk, de temperatuur, en de manier waarop ijs kristalliseert zijn er ontzettend veel vormen van ijs te produceren die allemaal een andere kristalstructuur kennen. Een enkel watermolecuul bestaat uit een zuurstofatoom waaraan twee waterstofatomen dicht gebonden zijn. De zuurstofatomen in ijs zitten zo dicht bij elkaar dat er tussen hen ook nog bindingen, ook wel waterstofbruggen genoemd, ontstaan tussen waterstofatomen en zuurstofatomen waaraan ze niet dicht gebonden zitten. Deze bindingen stabiliseren de kristalstructuur van ijs.

IJs zoals behandeld in deze Thesis is een speciale tweedimensionale vierkante vorm van ijs. Hoewel dit nogal theoretisch klinkt is deze vorm van ijs onlangs gerealiseerd[32] door water te vangen tussen twee lagen van grafeen. De watermoleculen liggen in een perfect platte laag op de vertices in een vierkant rooster. Elk van de moleculen vormt waterstofbruggen met twee van de vier buren. Wanneer een waterstofbrug gerepresenteerd wordt door een pijl vanaf het zuurstofatoom waaraan het waterstofatoom gebonden zit heeft elk molecuul twee pijlen naar binnen en twee naar buiten. Dit wordt ook wel de *ijsregel* genoemd. Er bestaan zes mogelijke configuraties, zie Figuur 5.3, per molecuul en daarom wordt dit model ook wel het zes-vertex-model genoemd.

In de laatste twee hoofdstukken kijken we naar een energetisch ijs-model, het F model, waarbij sommige van deze toegestane vertexconfiguraties een andere energie toegekend krijgen dan de andere. Dit zorgt voor een speci-

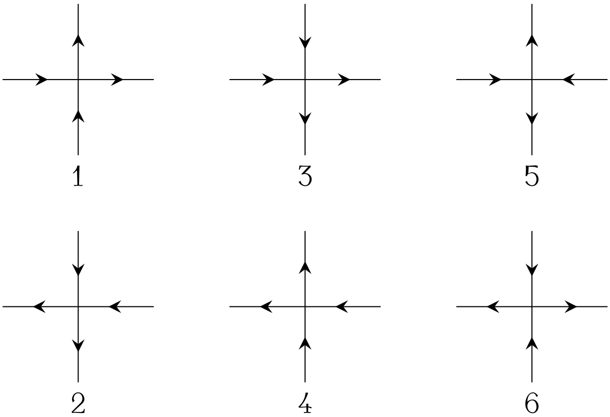

Figuur 5.3. De ijsregel eist dat er bij elke vertex twee pijlen naar binnen en twee pijlen naar buiten gaan. Dit resulteert in zes toegestane vertex configuraties.

ale oneindige-orde faseovergang van een ongeordende naar een geordende fase. De orde van een faseovergang geeft informatie over de manier waarop fasen in elkaar overgaan en het typische gedrag van oneindige-orde faseovergangen is dat deze juist weinig speciaals doen tijdens de faseovergang. In tegenstelling tot de meeste faseovergangen gebeurt er niet iets speciaals op de faseovergang "maar begint er iets te gebeuren". Dit maakt het erg moeilijk om deze faseovergang te detecteren. Wij hebben een nieuwe observabele geconstrueerd die per definitie wel uitzonderlijk gedrag vertoond op de faseovergang en laten zien dat deze kan worden gebruikt om de faseovergang te detecteren. Ook maken we duidelijk dat het een redelijk subtiel systeem is waarbij het, zelfs met deze nieuwe observabele, nog steeds erg moeilijk is om scherpe kwantitatieve uitspraken te kunnen doen doordat eindige-grootte effecten een zeer grote rol spelen.

In hoofdstuk drie kijken we naar het F model met periodieke randen, waarbij de pijltjes aan de randen zo gericht zijn dat de tegenovergestelde randen als het ware aan elkaar gelijmd kunnen worden. In hoofdstuk vier kijken we naar nog steeds naar het F model maar dan met speciale randvoorwaarden. Hierbij zijn de pijltjes aan de linker- en rechterrand naar buiten gericht, en bij de boven- en onderrand naar binnen gericht. In de meeste modellen verdwijnen de effecten van de gekozen randen voor systemen die voldoende groot zijn. Bij het F model blijkt dit niet zo te zijn. Zelfs voor systemen van oneindige grootte laten we zien dat het gehele systeem zich anders gedraagt voor deze speciale randen, domein muren genaamd, ten opzichte van periodieke muren.

Acknowledgements

Although time spent on research in theoretical physics is mostly spent alone, the interaction with other people is a vital part of research and it is here that I explicitly thank all the people that helped give this work its final form.

I would like to start by thanking my day-to-day advisors, Gerard and Rembert, for providing guidance the last four years. I have also had the pleasure of collaborating with Andrey, Patrick, Stefan, Lars, Mark, Sascha, Erik, Pepijn, and Jules and would like to thank the above for helping me publish parts of my work. Besides the people that were directly involved with my research I would also like to thank the supporting staffs at Leiden and Utrecht University for helping with more administrative matters.

I also appreciate all my friends' and family's support and general interest in my work. Special thanks go out to my partner, Joëlle, who has been nothing but loving and supporting from beginning to end.

Curriculum vitae

I was born on the 24th of June 1988 in Hengelo but was raised in Bennekom. I attended The Marnix College (2000-2007) in Ede where I received my VWO diploma. At Utrecht University I successfully completed my bachelor studies in Physics as well as the master in Theoretical Physics (2007-2013). I was able to obtain a PhD position (2013-2017) at Leiden university, at Instituut Lorentz for Theoretical Physics, although I physically worked at Utrecht University during most of this time. I will continue doing research as a PostDoc at the Department of Information and Computing Sciences at Utrecht University.